



Preliminary Trigonometric Parallaxes of 184 Late-T and Y Dwarfs and an Analysis of the Field Substellar Mass Function into the “Planetary” Mass Regime

J. Davy Kirkpatrick¹, Emily C. Martin^{2,3}, Richard L. Smart⁴, Alfred J. Cayago⁵, Charles A. Beichman¹, Federico Marocco^{1,6}, Christopher R. Gelino¹, Jacqueline K. Faherty⁷, Michael C. Cushing⁸, Adam C. Schneider⁹, Gregory N. Mace¹⁰, Christopher G. Tinney^{11,12}, Edward L. Wright², Patrick J. Lowrance¹³, James G. Ingalls¹³, Frederick J. Vrba¹⁴, Jeffrey A. Munn¹⁴, Scott E. Dahm¹⁴, and Ian S. McLean²

¹ IPAC, Mail Code 100-22, Caltech, 1200 E. California Boulevard, Pasadena, CA 91125, USA; davy@ipac.caltech.edu

² Department of Physics and Astronomy, University of California Los Angeles, 430 Portola Plaza, Box 951547, Los Angeles, CA 90095-1547, USA

³ Department of Astronomy & Astrophysics, University of California Santa Cruz, 1156 High Street, Santa Cruz, CA 95064, USA

⁴ Istituto Nazionale di Astrofisica, Osservatorio Astrofisico di Torino, Strada Osservatorio 20, I-10025 Pino Torinese, Italy

⁵ Department of Statistics, University of California Riverside, 900 University Avenue, Riverside, CA 92521, USA

⁶ Jet Propulsion Laboratory, California Institute of Technology, MS 169-237, 4800 Oak Grove Drive, Pasadena, CA 91109, USA

⁷ Department of Astrophysics, American Museum of Natural History, Central Park West at 79th Street, New York, NY 10034, USA

⁸ The University of Toledo, 2801 West Bancroft Street, Mailstop 111, Toledo, OH 43606, USA

⁹ School of Earth and Space Exploration, Arizona State University, Tempe, AZ 85282, USA

¹⁰ McDonald Observatory and the Department of Astronomy, The University of Texas at Austin, Austin, TX 78712, USA

¹¹ School of Physics, University of New South Wales, NSW 2052, Australia

¹² Australian Centre for Astrobiology, University of New South Wales, NSW 2052, Australia

¹³ IPAC, Mail Code 314-6, Caltech, 1200 E. California Boulevard, Pasadena, CA 91125, USA

¹⁴ US Naval Observatory, Flagstaff Station, P.O. Box 1149, Flagstaff, AZ 86002, USA

Received 2018 October 11; revised 2018 November 29; accepted 2018 December 3; published 2019 January 24

Abstract

We present preliminary trigonometric parallaxes of 184 late-T and Y dwarfs using observations from *Spitzer* (143), the U.S. Naval Observatory (18), the New Technology Telescope (14), and the United Kingdom Infrared Telescope (9). To complete the 20 pc census of $\geq T6$ dwarfs, we combine these measurements with previously published trigonometric parallaxes for an additional 44 objects and spectrophotometric distance estimates for another 7. For these 235 objects, we estimate temperatures, sift into five 150 K wide T_{eff} bins covering the range 300–1050 K, determine the completeness limit for each, and compute space densities. To anchor the high-mass end of the brown dwarf mass spectrum, we compile a list of early- to mid-L dwarfs within 20 pc. We run simulations using various functional forms of the mass function passed through two different sets of evolutionary code to compute predicted distributions in T_{eff} . The best fit of these predictions to our L, T, and Y observations is a simple power-law model with $\alpha \approx 0.6$ (where $dN/dM \propto M^{-\alpha}$), meaning that the slope of the field substellar mass function is in rough agreement with that found for brown dwarfs in nearby star-forming regions and young clusters. Furthermore, we find that published versions of the log-normal form do not predict the steady rise seen in the space densities from 1050 to 350 K. We also find that the low-mass cutoff to formation, if one exists, is lower than $\sim 5 M_{\text{Jup}}$, which corroborates findings in young, nearby moving groups and implies that extremely low-mass objects have been forming over the lifetime of the Milky Way.

Key words: brown dwarfs – parallaxes – solar neighborhood – stars: distances – stars: luminosity function, mass function

Supporting material: figure set

1. Introduction

Understanding the creation mechanisms for brown dwarfs has long been a stumbling block of star formation theory. Simplified arguments predicting the minimum Jeans mass fragment forming from a molecular cloud suggest a value of $\sim 7 M_{\text{Jup}}$ (Low & Lynden-Bell 1976), although more complicated considerations such as the role of magnetic fields and rotation are thought to drive this value higher. Lower formation masses are possible via secondary mechanisms. For example, sites replete with high-mass stars can create lower-mass brown dwarfs through the ablation, via O star winds, of protostellar embryos that would otherwise have formed bona fide stars (e.g., Whitworth & Zinnecker 2004). Also, protostars in rich clusters with many high-mass members may, via dynamical interactions, be stripped from their repository of accreting material, thus artificially stunting their growth (e.g., Reipurth & Clarke 2001). Star-forming regions lacking higher

mass stars will form objects via neither of these processes but still create low-mass objects down to at least $\sim 3 M_{\text{Jup}}$, as discoveries of low-mass brown dwarfs in nearby, sparse moving groups suggest (Liu et al. 2013; Gagné et al. 2015a; Faherty et al. 2016; Best et al. 2017). Providing direct measurements on the frequency of low-mass formation and its low-mass limit are thus key parameters needed to inform modified predictions.

Field brown dwarfs—the well-mixed, low-mass byproducts of star formation—can be used to derive the field substellar mass function. This function averages over any site-to-site differences and allows us to study the global efficiency of substellar formation integrated over the history of the Galactic disk. Does this field function suggest that low-mass star formation can be characterized by a simple form (Chabrier 2001) or only by a more complicated one (Kroupa et al. 2013)? What is the low-mass cutoff (Andersen et al. 2008)? Have these

field objects, scattered from their stellar nurseries, been joined by other low-mass objects that escaped their birthplaces within a proto-planetary disk (Sumi et al. 2011; Mróz et al. 2017)? Is the formation efficiency of low-mass objects higher today than it was in the distant past (Bate 2005)?

Our ability to measure the low-mass cutoff is critically dependent on measuring the space density of objects with temperatures below 500 K (Figure 12 of Burgasser 2004), which corresponds to late-T and Y dwarf spectral types believed to span a mass range of $\sim 3\text{--}20 M_{\text{Jup}}$ (Cushing et al. 2011; Luhman 2014a). The functional form of the mass function is also most easily discerned at these same temperatures (Figure 5 of Burgasser 2004). Both of these measurements can be accomplished by establishing a volume-limited sample of nearby brown dwarfs.

The recent spate of cold, field brown dwarf discoveries by the NASA *Wide-field Infrared Survey Explorer* (*WISE*) now makes these measurements possible. The all-sky nature of *WISE* enables the creation of a sample of the closest, brightest brown dwarfs that exist, and these are the easiest brown dwarfs to characterize in detail. In this paper, we aim to use these discoveries to deduce the functional form and low-mass cutoff of the substellar mass function.

In Section 2 we discuss the empirical sample needed to address our goals, and in Section 3 we build a preliminary version of the sample. In subsequent sections we describe astrometric measurements from *Spitzer* (Sections 4 and 5), the U.S. Naval Observatory (Section 6), and other telescopes (Section 7) needed to further characterize the sample. In Section 8 we examine the measured trends in spectral type, color, and absolute magnitude to identify hidden binaries. In Section 9 we build predictions of the space density as a function of T_{eff} using two different suites of evolutionary models and several different forms of the underlying mass function; these are compared to our empirical results to deduce the most likely functional form and to place constraints on the mass of the low-mass cutoff. We discuss these results in context with theoretical predictions in Section 10. In Section 11 we summarize our conclusions and discuss future plans for making the sample even more robust.

2. Establishing the Empirical Data Set

To reach the above goals, we define an empirical sample and a list of follow-up observations necessary to adequately characterize it. We consider the following four points:

- (1) Accurate distances to these objects must be measured so that space densities can be calculated. These objects will have large parallactic signatures, but they are extremely faint in the optical and near-infrared wavelengths where ground-based astrometric monitoring takes place. For the faintest objects ($J > 21$ mag), the Earth's atmosphere and thermal environment preclude parallax measurements entirely. *Gaia* is unable to measure parallaxes for cold brown dwarfs because it observes only shortward of $1.05 \mu\text{m}$, a wavelength regime in which these sources emit very little flux. Observations are more easily done at wavelengths near $5 \mu\text{m}$ where these objects are brightest. The InfraRed Array Camera (IRAC; Fazio et al. 2004) on board the *Spitzer Space Telescope* is therefore a natural choice, and accurate parallaxes can be measured using only a modest amount of *Spitzer* observing time.
- (2) Objects must be characterized to the extent that unresolved binarity can be deduced. Unresolved binaries can lead to overestimates of the space density when spectrophotometric distance estimates are used, or underestimates if objects truly in the volume are not recognized as double. This is an inherent problem with any magnitude-limited sample. Although high-resolution imaging has been acquired for some of the nearest brown dwarfs (Gelino et al. 2011; Liu et al. 2012; Opitz et al. 2016), very tight binaries or those with unfavorable orientations as seen from the Earth will go undetected. Measuring the absolute magnitude directly for each object is an excellent means of detecting unresolved doubles with small magnitude differences.
- (3) The number of sources as a function of T_{eff} (or other observable quantity) must be known with sufficient resolution in mass to determine the low-mass cutoff to a few M_{Jup} . As Table 9 of Kirkpatrick et al. (2012) shows, a volume-limited sample with a distance limit of 20 pc provides between one dozen and four dozen objects in each half-subclass spectral type bin from T6 through early Y, although the magnitude limits of *WISE* restrict the T9 and later bins to somewhat smaller distances. This binning provides sufficient resolution to determine the low-mass cut-off to the precision required. Including brown dwarfs as early as T6 allows us to properly measure the shape of the density distribution below ~ 1100 K so that we can also place constraints on the overall functional form of the mass function, as Figure 14 of Kirkpatrick et al. (2012) illustrates.
- (4) A sufficient sample size must be considered to robustly measure biases due to metallicity effects. At late-T and Y types, a higher percentage of old objects may be expected relative to field stars because the only young objects possible at these types are those that are exceedingly low in mass, although the percentage is critically dependent upon the low-mass cutoff of formation. (See, e.g., Figure 8 of Burgasser 2004). Several late-T subdwarfs, believed to be older objects with lower-than-average metal content, are already recognized in the nearby sample. These can serve as metallicity calibrators with which to calibrate the absolute magnitude versus spectral type relations as a function of metallicity and to provide the first evidence on the efficiency of low-mass formation at lower metallicities. These objects are relatively rare, and to measure the spread in age for each mass bin, sufficient statistics (i.e., a large sample size over a sizable volume) is needed.

In conclusion, a volume-limited sample out to 20 pc that covers spectral types of T6 and later would fulfill our research goals. In the next section, we describe how we tabulated sources belonging to the sample itself.

3. Target Selection for the 20 pc Sample of $\geq T6$ Dwarfs

Using the compilation of known T and Y dwarfs at Dwarf Archives¹⁵ along with a listing of more recent additions that one of us (CRG) has compiled since the last Dwarf Archives update, we cataloged all published objects of type T6 and later (>350 total), regardless of distance. We then used spectral

¹⁵ See <http://www.DwarfArchives.org>.

Table 1
Dwarfs with Type $\geq T6$ and Distance or Distance Estimate ≤ 20 pc

Discovery Designation (1)	Disc. Ref. (2)	WISEA Designation (3)	Infrared Sp. Type (4)	Type Ref. (5)	Parallax (mas) (6)	Parallax Ref. (7)
WISE J000517.48+373720.5	8	J000517.49+373720.4	T9	8	Table 4	1
WISE J001505.87-461517.6	2	J001505.88-461517.8	T8	2	Table 4	1
WISE J003231.09-494651.4	2	J003231.06-494651.9	T8.5	2	Table 4	1
ULAS J003402.77-005206.7	27	J003402.79-005208.2	T8.5	10	68.7 ± 1.4 (abs)	67
2MASS J00345157+0523050	3	J003452.03+052306.9	T6.5	61	Table 4	1
	105.4 ± 7.5 (abs)	66
WISE J003829.05+275852.1	8	J003829.06+275852.0	T9	8	Table 4	1
GI 27B (0039+2115)*	28	<i>source not extracted</i>	T8	61	89.7891 ± 0.0581 (abs)	72
WISE J004024.88+090054.8	8	J004024.88+090054.4	T7	8	Table 6	1
WISE J004945.61+215120.0	8	J004945.65+215119.6	T8.5	8	Table 4	1
2MASS J00501994-3322402	29	J005021.05-332228.8	T7	61	94.6 ± 2.4 (abs)	67
CFBDS J005910.90-011401.3	30	J005911.10-011401.1	T8.5	10	103.2 ± 2.1 (abs)	67
WISEPA J012333.21+414203.9	4	J012333.25+414203.9	T7	4	Table 4	1
CFBDS J013302.27+023128.4	5	J013302.45+023128.8	T8.5	5	Table 4	1
WISE J014656.66+423410.0AB	2	J014656.66+423409.9	Y0	2	Table 4	1
WISEPC J014807.25-720258.7	4	J014807.34-720258.7	T9.5	4	91.1 ± 3.4 (rel)	21
ULAS J015024.37+135924.0	31	J015024.40+135923.6	T7.5	31	Table 6	1
WISEP J022105.94+384202.9	4	J022105.99+384203.0	T6.5	4	Table 4	1
WISEPC J022322.39-293258.1	4	J022322.38-293257.3	T7.5	4	Table 6	1
WISEPA J022623.98-021142.8AB	4	J022623.99-021142.7	T7	4	Table 4	1
WISE J023318.05+303030.5	8	J023318.06+303030.4	T6	8	Table 4	1
WISE J024124.73-365328.0	2	J024124.74-365328.0	T7	2	Table 4	1
2MASS J0243137-245329	32	J024313.47-245332.1	T6	61	93.62 ± 3.63 (abs)	68
WISE J024512.62-345047.8	8	J024512.62-345047.8	T8	8	59	1
WISE J024714.52+372523.5	8	J024714.54+372523.4	T8	8	Table 4	1
WISEPA J025409.45+022359.1	4, 33	J025409.55+022358.5	T8	4	Table 5	1
WISEA J030237.53-581740.3	6	J030237.53-581740.3	Y0:	6	Table 4	1
WISE J030449.03-270508.3	7	J030449.04-270508.1	Y0pec	7	Table 4	1
WISEA J030919.70-501614.2	6	J030919.70-501614.2	[T7] ^b	6	Table 4	1
WISEPA J031325.96+780744.2	4	J031326.00+780744.3	T8.5	4	Table 4	1
WISE J031624.35+430709.1	8	J031624.40+430708.7	T8	8	Table 4	1
WISEA J032309.12-590751.0	1	J032309.12-590751.0	[T6] ^c	1	Table 4	1
WISEPC J032337.53-602554.9	4	J032337.57-602554.5	T8.5	4	Table 4	1
WISE J032504.33-504400.3	9	J032504.52-504403.0	T8	9	Table 4	1
WISE J032517.69-385454.1	8	J032517.68-385453.8	T9	8	Table 4	1
WISE J032547.72+083118.2	8	J032547.73+083118.2	T7	8	Table 4	1
WISE J033515.01+431045.1	8	J033515.07+431044.7	T9	8	Table 4	1
WISE J033605.05-014350.4	8	J033605.04-014351.0	Y0	22	Table 4	1
2MASS J03480772-6022270	34	J034807.33-602235.2	T7	61	Table 6	1
WISE J035000.32-565830.2	2	J035000.31-565830.5	Y1	2	Table 4	1
WISE J035934.06-540154.6	2	J035934.07-540154.8	Y0	2	Table 4	1
WISE J040443.48-642029.9	9	J040443.50-642030.0	T9	9	Table 4	1
WISEPA J041022.71+150248.5	10	J041022.75+150247.9	Y0	10	Table 4	1
WISE J041358.14-475039.3	8	J041358.14-475039.4	T9	8	Table 4	1
2MASS J0415195-093506	32	J041521.26-093500.4	T8	61	175.2 ± 1.7 (abs)	67
WISE J043052.92+463331.6	8	J043052.96+463331.7	T8	8	Table 4	1
WISEPA J045853.89+643452.9AB	11	J045853.91+643452.6	T8.5	10	Table 4	1
WISEPA J050003.05-122343.2	4	J050003.03-122343.1	T8	4	Table 4	1
WISE J051208.66-300404.4	8	J051208.67-300404.2	T8.5	8	Table 4	1
WISEPA J051317.28+060814.7	4	J051317.27+060814.5	T6.5	4	Table 5	1
WISE J052126.29+102528.4	35	J052126.30+102528.3	T7.5	35	171	1
UGPS J052127.27+364048.6	46	J052127.42+364043.6	T8.5	46	Table 6	1
WISEPA J052844.51-330823.9	4	J052844.52-330824.0	T7pec	4	Table 6	1
WISE J053516.80-750024.9	2	J053516.87-750024.6	$\geq Y1$:	2	Table 4	1
WISE J054047.00+483232.4	8	J054047.01+483232.2	T8.5	8	Table 4	1
WISEPA J054231.26-162829.1	4	J054231.27-162829.1	T6.5	4	Table 6	1
GI 229B (0610-2152)	36	<i>source not extracted</i>	T7pec	61	173.6955 ± 0.0457 (abs)	72
WISEPA J061213.93-303612.7AB	4	J061213.88-303612.1	T6	4	Table 6	1
WISEPA J061407.49+391236.4	4	J061407.50+391235.7	T6	4	Table 5	1
WISE J061437.73+095135.0	8	J061437.75+095135.2	T7	8	Table 4	1
WISEA J061557.21+152626.1	22	J061557.21+152626.1	T8.5	22	64	1
WISEPA J062309.94-045624.6	4	J062309.92-045624.5	T8	4	Table 6	1
WISEPA J062542.21+564625.5	4	J062542.23+564625.4	T6	4	Table 5	1
WISEPA J062720.07-111428.8	4	J062720.07-111427.9	T6	4	Table 6	1
WISE J062842.71-805725.0	6	J062842.74-805725.0	[T9] ^d	6	50	1
WISEA J064528.39-030247.9	6	J064528.39-030247.9	T6	6	Table 4	1
WISE J064723.23-623235.5	12	J064723.24-623235.4	Y1	12	Table 4	1
WISEA J071301.86-585445.2	6	J071301.86-585445.2	T9	6	Table 4	1
WISE J071322.55-291751.9	2	J071322.55-291752.0	Y0	2	Table 4	1
UGPS J072227.51-054031.2	37	J072227.27-054029.8	T9	10	242.8 ± 2.4	40

Table 1
(Continued)

Discovery Designation (1)	Disc. Ref. (2)	WISEA Designation (3)	Infrared Sp. Type (4)	Type Ref. (5)	Parallax (mas) (6)	Parallax Ref. (7)
WISE J072312.44+340313.5	8	J072312.47+340313.5	T9:	8	Table 4	1
2MASS J0727182+171001	32	J072719.15+170951.3	T7	61	112.5 ± 0.9 (abs)	67
2MASS J07290002-3954043	24	J072859.49-395345.3	T8pec	24	126.3 ± 8.3 (abs)	66
WISE J073444.02-715744.0	2	J073444.03-715743.8	Y0	2	Table 4	1
WISEPA J074457.15+562821.8	4	J074457.24+562820.9	T8	4	Table 4	1
ULAS J074502.79+233240.3	19	<i>source not extracted</i>	T8.5	19	63	42
WISEPA J075003.84+272544.8	4	J075003.75+272545.0	T8.5	4	Table 6	1
WISEPA J075108.79-763449.6	4	J075108.80-763449.3	T9	4	Table 6	1
WISEPC J075946.98-490454.0	4	J075946.98-490454.0	T8	4	Table 4	1
WD 0806-661B (0807-6618)	65	<i>source not detected</i>	[Y1] ^e	1	52.17 ± 1.67 (abs)	69
WISE J081117.81-805141.3	8	J081117.95-805141.4	T9.5:	8	98.5 ± 7.7 (rel)	21
WISE J081220.04+402106.2	8	J081220.05+402106.2	T8	8	Table 4	1
DENIS J081730.0-615520	38	J081729.76-615503.8	T6	38	203 ± 13	38
WISE J082507.35+280548.5	9	J082507.37+280548.2	Y0.5	9	Table 4	1
WISE J083337.83+005214.2	13	J083337.81+005213.8	(sd)T9	13	Table 4	1
WISEPC J083641.12-185947.2	4	J083641.13-185947.1	T8pec	4	Table 4	1
WISE J085510.83-071442.5	14, 15, 16	J085510.74-071442.5	[\geq Y4] ^f	1	Table 4	1
WISEPA J085716.25+560407.6	4	J085716.21+560407.5	T8	4	Table 4	1
ULAS J085910.69+101017.1	64	J085910.62+101014.8	T7	64	Table 6	1
ULAS J090116.23-030635.0	39	J090116.20-030636.0	T7.5	39	62.6 ± 2.6 (abs)	70
WISEPA J090649.36+473538.6	4	J090649.33+473538.2	T8	4	Table 4	1
WISE J091408.96-345941.5	17	J091408.99-345941.4	T8	6	Table 4	1
WISEPC J092906.77+040957.9	4	J092906.76+040957.6	T6.5	4	Table 6	1
2MASS J0937347+293142	32	J093735.63+293127.2	T6pec	61	162.84 ± 3.88 (abs)	68
2MASS J09393548-2448279	29	J093935.93-244838.9	T8	61	187.3 ± 4.6 (abs)	71
WISEA J094020.09-220820.5	6	J094020.09-220820.5	T8	6	Table 4	1
WISE J094305.98+360723.5	18	J094306.00+360723.3	T9.5	18	Table 4	1
ULAS J095047.28+011734.3 ^g	40, 41	J095047.31+011733.1	T8	19, 8	Table 6	1
...	53.40 ± 3.51	19
WISEPC J095259.29+195507.3	4	J095259.29+195508.1	T6	4	Table 4	1
WISEPC J101808.05-244557.7	4	J101808.03-244558.1	T8	4	Table 4	1
WISEPA J101905.63+652954.0	4	J101905.61+652954.0	T6	4	Table 5	1
WISE J102557.72+030755.7	8	J102557.67+030755.8	T8.5	8	Table 4	1
CFBDS J102841.01+565401.9	5	<i>source not extracted</i>	T8	5	Table 4	1
ULAS J102940.52+093514.6	19	J102940.51+093514.1	T8	20	Table 6	1
WISE J103907.73-160002.9	8	J103907.74-160002.9	T7.5	8	Table 4	1
WISEPC J104245.23-384238.3	4	J104245.24-384238.1	T8.5	4	64.8 ± 3.4 (rel)	21
ULAS J104355.37+104803.4	19	J104355.40+104802.4	T8	19	Table 4	1
2MASS J1047538+212423	43	J104752.35+212417.2	T6.5	61	94.73 ± 3.81 (abs)	68
WISE J105047.90+505606.2	8	J105047.89+505606.9	T8	8	Table 4	1
WISE J105130.01-213859.7	8	J105130.02-213859.9	T8.5	22	Table 4	1
WISE J105257.95-194250.2	20	J105257.95-194250.1	T7.5	20	Table 4	1
WISEA J105553.62-165216.5	6	J105553.62-165216.5	T9.5	22	Table 4	1
WISE J111239.24-385700.7	6	J111239.25-385700.5	T9	6	56	1
2MASS J11145133-2618235	29	J111448.74-261827.9	T7.5	61	179.2 ± 1.4 (abs)	67
WISE J111838.70+312537.9 ^h	2, 44	J111838.69+312537.7	T8.5	44	113.2 ± 4.6 (abs)	75
WISEPC J112254.73+255021.5	4	J112254.70+255021.9	T6	4	Table 5	1
WISE J112438.12-042149.7	8	J112438.10-042149.6	T7	8	Table 4	1
WISE J113949.24-332425.1	20	J113949.23-332425.4	T7	20	Table 4	1
WISEA J114156.67-332635.5	21	J114156.67-332635.5	Y0	6	Table 4	1
WISE J114340.22+443123.8	8	J114340.22+443124.0	T8.5	8	Table 4	1
WISEP J115013.88+630240.7	4	J115013.85+630241.3	T8	4	Table 4	1
ULAS J115239.94+113407.6	19	J115239.94+113406.9	T8.5	19	Table 4	1
WISE J120604.38+840110.6	9	J120604.25+840110.5	Y0	9	Table 4	1
2MASS J1217110-031113	43	J121710.27-031112.1	T7.5	61	90.8 ± 2.2 (rel)	76
WISEPC J121756.91+162640.2AB	4	J121756.92+162640.3	T9	4	Table 4	1
WISEA J122036.38+540717.3	22	J122036.38+540717.3	T9.5	22	Table 4	1
WISE J122152.28-313600.8	8	J122152.28-313600.7	T6.5	8	Table 4	1
2MASS J12255432-2739466AB	43	J122554.66-273954.1	T6	61	75.1 ± 2.5 (rel)	76
WISE J122558.86-101345.2	8	J122558.86-101345.2	T6	8	Table 4	1
2MASS J12314753+0847331	3	J123146.70+084722.1	T5.5 ⁱ	61	Table 4	1
2MASS J12373919+6526148	43	J123737.33+652608.0	T6.5	61	96.07 ± 4.78 (abs)	68
ULAS J123828.51+095351.3	42	J123828.38+095352.0	T8	10	Table 6	1
WISE J124309.61+844547.8	20	J124309.40+844547.7	T9	20	Table 4	1
WISE J125015.56+262846.9	8	J125015.56+262846.8	T6.5	8	53	1
WISE J125448.52-072828.4	20	J125448.50-072828.3	T7	20	Table 4	1
WISE J125715.90+400854.2	8	J125715.91+400854.2	T7	8	Table 4	1
VHS J125804.89-441232.4	23	J125804.91-441232.6	T6	23	Table 4	1
Gl 494C (1300+1221) ^j	45	J130041.63+122114.5	T8	10	86.8570 ± 0.1515 (abs)	72
WISE J130141.62-030212.9	8	J130141.63-030212.9	T8.5	8	Table 4	1

Table 1
(Continued)

Discovery Designation (1)	Disc. Ref. (2)	WISEA Designation (3)	Infrared Sp. Type (4)	Type Ref. (5)	Parallax (mas) (6)	Parallax Ref. (7)
ULAS J130217.21+130851.2	31	J130217.07+130851.1	T8	10	65 ± 5 (abs)	77
WISEPC J131106.24+012252.4	4	J131106.21+012253.9	T9:	4	Table 6	1
ULAS J131508.42+082627.4	64	J131508.40+082627.0	T7.5	64	Table 6	1
WISE J131833.98-175826.5	8	J131833.96-175826.3	T8	22	Table 4	1
WISEPC J132004.16+603426.2	4	J132004.16+603426.1	T6.5	4	Table 5	1
WISEPA J132233.66-234017.1	4	J132233.63-234017.0	T8	4	Table 5	1
WISEA J133300.03-160754.4	1	J133300.03-160754.4	[T7.5] ^k	1	Table 4	1
ULAS J133553.45+113005.2	42	J133553.41+113004.7	T8.5	10	99.9 ± 1.6 (abs)	67
SDSSp J134646.45-003150.4	47	J134646.05-003151.5	T6.5	61	68.3 ± 2.3 (rel)	76
WISEPC J140518.40+553421.4	10	J140518.32+553421.3	Y0.5(pec?)	9, 73	Table 4	1
ULAS J141623.94+134836.3	49	J141623.96+134836.0	(sd)T7.5	62	109.7 ± 1.3 (abs) ^l	67
GI 547B (1423+0116) ^m	50	J142320.84+011637.5	sdT8, T8	50, 8	57.3445 ± 0.0362 (abs)	72
VHS J143311.46-083736.3	23	J143311.41-083736.6	T8	23	Table 4	1
WISEPA J143602.19-181421.8	4	J143602.19-181422.0	T8pec	4	Table 4	1
WISE J144806.48-253420.3	20	J144806.48-253420.5	T8	20	Table 4	1
GI 570D (1457-2121)	51	J145715.83-212208.0	T7.5	61	170.0112 ± 0.0851 (abs)	72
WISEPC J145715.03+581510.2	4	J145715.01+581510.1	T7	4	Table 5	1
WISE J150115.92-400418.4	17	J150115.92-400418.2	T6	6	Table 4	1
2MASS J15031961+2525196	52	J150319.68+252525.7	T5	61	157.2 ± 2.2 (abs)	67
SDSS J150411.63+102718.4	53	J150411.81+102715.4	T7	53	46.1 ± 1.5 (abs)	67
GI 576B (1504+0538) ⁿ	54	J150457.56+053759.8	T6pec	54	52.5873 ± 0.0668 (abs)	72
WISEPC J150649.97+702736.0	4	J150649.92+702736.1	T6	4	Table 5	1
WISE J151721.13+052929.3	8	J151721.12+052929.3	T8	8	Table 4	1
WISEPC J151906.64+700931.5	4	J151906.63+700931.3	T8	4	Table 4	1
WISE J152305.10+312537.6	8	J152305.09+312537.3	T6.5pec	8	Table 4	1
WISEPA J154151.66-225025.2	10	J154151.65-225024.9 ^o	Y1	9	Table 4	1
WISE J154214.00+223005.2	8	J154214.00+223005.2	T9.5	8	Table 4	1
2MASS J1553022+153236AB	32	J155301.93+153238.8	T7	61	75.1 ± 0.9 (abs)	67
WISEPA J161215.94-342027.1	4	J161215.92-342028.5	T6.5	4	Table 4	1
WISEPA J161441.45+173936.7	4	J161441.47+173935.4	T9	4	Table 4	1
2MASS J16150413+1340079	24	J161504.36+134004.0	T6	24	Table 4	1
...	68.6 ± 6.4 (abs)	66
WISEPA J161705.75+180714.3	4	J161705.73+180714.1	T8	4	Table 6	1
WISEPA J162208.94-095934.6	4	J162208.93-095934.6	T6	4	Table 4	1
SDSSp J162414.37+002915.6	55	J162414.07+002915.6	T6	61	90.9 ± 1.2 (rel)	76
WISEPA J162725.64+325525.5	4	J162725.64+325524.5	T6	4	Table 5	1
SDSS J162838.77+230821.1	53	J162838.99+230817.9	T7	53	75.1 ± 0.9 (abs)	67
WISE J163940.86-684744.6	17	J163940.84-684739.4	YOpec	9	Table 4	1
WISEPA J165311.05+444423.9	4	J165311.03+444422.7	T8	4	Table 4	1
WISEPA J171104.60+350036.8AB	4	J171104.59+350036.7	T8	4	Table 4	1
WISEPA J171717.02+612859.3	4	J171717.04+612859.2	T8	4, 8	Table 4	1
WISE J172134.46+111739.4	8	J172134.46+111739.5	T6	8	Table 4	1
WISEA J173551.56-820900.3	6	J173551.56-820900.3	T6	6	Table 4	1
WISEPA J173835.53+273258.9	10	J173835.52+273258.8	Y0	10	Table 4	1
WISEPA J174124.26+255319.5	4, 33, 56	J174124.22+255319.2	T9	4	Table 5	1
SDSS J175805.46+463311.9 ^p	57	J175805.45+463316.9	T6.5	61	71.4754 ± 0.0354 (abs)	72
WISEPA J180435.40+311706.1	4	J180435.37+311706.2	T9.5:	4	Table 4	1
WISEPA J181210.85+272144.3	4	J181210.83+272144.2	T8.5:	10	Table 6	1
WISE J181243.14+200746.4	8	J181243.14+200746.2	T9	8	Table 4	1
WISE J181329.40+283533.3	8	J181329.40+283533.3	T8	8	Table 4	1
WISEPA J182831.08+265037.8	10	J182831.08+265037.6	≥Y2	2	Table 4	1
SCR J1845-6357B	58	<i>source not extracted</i>	T6	63	259.45 ± 1.11 (abs)	78
WISEPA J185215.78+353716.3	4	J185215.82+353716.2	T7	4	Table 5	1
WISEPA J190624.75+450808.2	4	J190624.73+450807.0	T6	4	Table 5	1
WISE J192841.35+235604.9	8	J192841.39+235604.5	T6	8	Table 4	1
WISE J195500.42-254013.9	8	J195500.42-254013.5	T8	8	Table 4	1
WISEPA J195905.66-333833.7	4	J195905.64-333833.8	T8	4	Table 4	1
WISE J200050.19+362950.1	18	J200050.19+362950.1	T8	18	Table 4	1
WISE J200520.38+542433.9	25	J200520.35+542433.6	sdT8	25	Table 4	1
WISE J201546.27+664645.1	8	J201546.45+664645.2	T8	8	Table 4	1
WISEA J201748.74-342102.6	6	J201748.74-342102.6	[T7.5] ^q	6	Table 4	1
WISEPA J201824.96-742325.9	4	J201824.99-742327.9	T7	4	Table 6	1
WISE J201920.76-114807.5	8	J201920.75-114807.5	T8:	8	Table 4	1
WISEPC J205628.90+145953.3	10	J205628.88+145953.6	Y0	10	Table 4	1
WISE J210200.15-442919.5	2	J210200.14-442919.9	T9	2	92.3 ± 1.9 (rel)	21
WISEPA J213456.73-713743.6	4	J213456.79-713744.7	T9pec	4	109.1 ± 3.7 (rel)	21
ULAS J214638.83-001038.7 ^r	59	J214639.07-001039.3	T8.5	10	79.8 ± 4.5 (abs)	79
WISE J214706.78-102924.0	8	J214706.79-102923.7	T7.5	8	Table 4	1
WISEPC J215751.38+265931.4	4	J215751.35+265931.2	T7	4	Table 4	1
WISEA J215949.54-480855.2	6	J215949.54-480855.2	T9	6	Table 4	1

Table 1
(Continued)

Discovery Designation (1)	Disc. Ref. (2)	WISEA Designation (3)	Infrared Sp. Type (4)	Type Ref. (5)	Parallax (mas) (6)	Parallax Ref. (7)
WISEA J220304.18+461923.4	22	J220304.18+461923.4	T8	22	Table 4	1
GI 845C (2204–5646) ^a	60	<i>source not extracted</i>	T6	61	274.8048 ± 0.2494 (abs)	72
WISE J220905.73+271143.9	4	J220905.73+271143.9	Y0:	18	Table 4	1
WISEPC J220922.10–273439.5	4	J220922.09–273439.9	T7	4	Table 4	1
WISEA J221140.53–475826.7	6	J221140.53–475826.7	[T8] ^d	6	Table 4	1
WISE J221216.33–693121.6	9	J221216.27–693121.6	T9	9	Table 4	1
WISEPC J221354.69+091139.4	4	J221354.69+091139.3	T7	4	Table 5	1
WISE J222055.31–362817.4	2	J222055.34–362817.5	Y0	2	Table 4	1
WISEPC J222623.05+044003.9	4	J222623.06+044003.2	T8	4	Table 5	1
2MASS J22282889–4310262	34	J222829.01–431029.8	T6	61	92.1 ± 2.6 (abs)	74
WISEA J223204.53–573010.4	6	J223204.53–573010.4	T9	6	Table 4	1
WISE J223720.39+722833.8	8	J223720.39+722833.9	T6	8	Table 4	1
WISEPC J225540.74–311841.8	4	J225540.75–311842.0	T8	4	Table 4	1
WISE J230133.32+021635.0	8	J230133.32+021635.0	T6.5	8	Table 4	1
WISEA J230228.66–713441.7	6	J230228.66–713441.7	[T4.5] ^h	6	Table 4	1
WISEPA J231336.40–803700.3	4	J231336.47–803700.4	T8	4	Table 4	1
WISEPC J231939.13–184404.3	4	J231939.14–184404.4	T7.5	4	Table 4	1
ULAS J232123.79+135454.9	26	J232123.82+135453.3	T7.5	31	Table 4	1
	84 ± 4 (abs)	77
WISEPC J232519.54–410534.9	4	J232519.55–410535.1	T9pec	4	107.8 ± 3.7 (rel)	21
ULAS J232600.40+020139.2	19	J232600.44+020138.4	T8	19	Table 4	1
WISE J233226.49–432510.6	2	J233226.54–432510.9	T9:	2	Table 4	1
WISEPC J234026.62–074507.2	4	J234026.61–074508.4	T7	4	Table 5	1
ULAS J234228.96+085620.1	26	J234228.97+085619.9	T6.5	8	Table 6	1
WISEPA J234351.20–741847.0	4	J234351.28–741846.9	T6	4	Table 4	1
WISEPC J234446.25+103415.8	4	J234446.24+103415.8	T9	4, 8	Table 4	1
WISEPC J234841.10–102844.4	4	J234841.11–102844.1	T7	4	Table 5	1
WISEA J235402.79+024014.1	9	J235402.79+024014.1	Y1	9	Table 4	1
WISE J235716.49+122741.8	8	J235716.49+122741.5	T6	8	Table 4	1

Notes.^a 0039+2115: Also known as HD 3651B.^b 0309–5016: Type estimated from methane imaging.^c 0323–5907: The ch1–ch2 color of 1.244 ± 0.033 mag (Table 2) suggests a type of T6 based on Figure 11 of Kirkpatrick et al. (2011).^d 0628–8057: Type estimated from methane imaging.^e 0807–6618: Given the fact that the absolute ch2 magnitude of this object (15.43 ± 0.09 mag) and ch1–ch2 color (2.81 ± 0.16 mag) are most like the Y1 dwarfs, this object has been assigned a temporary spectral type of Y1.^f 0855–0714: Given the fact that the absolute *H* and ch2 magnitudes of this object (27.04 ± 0.24 and 17.13 ± 0.02 mag, respectively) are *much* fainter, and the *H*–*W2* and ch1–ch2 colors (10.13 ± 0.24 and 3.55 ± 0.07 mag, respectively) *much* redder, than that of the other Y dwarfs typed as late as $\geq Y2$, this object has been assigned a temporary spectral type of $\geq Y4$.^g 0950+0117: This is a common-proper-motion companion to LHS 6176.^h 1118+3125: Also known as the distant companion to ξ UMa (GI 423).ⁱ 1231+0837: Object earlier in type than T6, but nonetheless included here because we obtained a parallax with *Spitzer*.^j 1300+1221: Also known as Ross 458C.^k 1333–1607: The Table 2 colors of ch1–ch2 = 1.811 ± 0.050 mag and *H*–ch2 = 3.369 ± 0.132 mag suggest, based on Figures 11 and 14 of Kirkpatrick et al. (2011), a type of T7.5.^l 1416+1348: The parallax of the sdL primary is quoted here for the (sd)T companion.^m 1423+0114: Also known as BD+01 2920B.ⁿ 1504+0538: Also known as HIP 73786B.^o 1541–2250: Source not extracted in the AllWISE Source Catalog, so this designation is the one from the WISE All-Sky Source Catalog.^p 1758+4633: Also known as GJ 4040B.^q 2017–3421: Type estimated from methane imaging.^r 2146–0010: Also known as Wolf 940B and GJ 1263B.^s 2204–5646: Also known as ϵ Indi Bb.^t 2211–4758: Type estimated from methane imaging.^u 2302–7134: Type estimated from methane imaging. Object earlier in type than T6, but nonetheless included here because we obtained a parallax with *Spitzer*.

References. (1) This paper, (2) Kirkpatrick et al. (2012), (3) Burgasser et al. (2004), (4) Kirkpatrick et al. (2011), (5) Albert et al. (2011), (6) Tinney et al. (2018), (7) Pinfield et al. (2014b), (8) Mace et al. (2013a), (9) Schneider et al. (2015), (10) Cushing et al. (2011), (11) Mainzer et al. (2011), (12) Kirkpatrick et al. (2013), (13) Pinfield et al. (2014a), (14) Luhman (2014b), (15) Kirkpatrick et al. (2014), (16) Luhman (2014a), (17) Tinney et al. (2012), (18) Cushing et al. (2014), (19) Burningham et al. (2013), (20) Thompson et al. (2013), (21) Tinney et al. (2014), (22) Martin et al. (2018), (23) Lodieu et al. (2012), (24) Looper et al. (2007), (25) Mace et al. (2013b), (26) Scholz (2010b), (27) Warren et al. (2007b), (28) Mugrauer et al. (2006), (29) Tinney et al. (2005), (30) Delorme et al. (2008), (31) Burningham et al. (2010b), (32) Burgasser et al. (2002), (33) Scholz et al. (2011), (34) Burgasser et al. (2003c), (35) Bihain et al. (2013), (36) Nakajima et al. (1995), (37) Lucas et al. (2010), (38) Artigau et al. (2010), (39) Lodieu et al. (2007), (40) Leggett et al. (2012), (41) Luhman et al. (2012), (42) Burningham et al. (2008), (43) Burgasser et al. (1999), (44) Wright et al. (2013), (45) Goldman et al. (2010), (46) Burningham et al. (2011), (47) Tsvetanov et al. (2000), (48) Cardoso et al. (2015), (49) Scholz (2010a), (50) Pinfield et al. (2012), (51) Burgasser et al. (2000), (52) Burgasser et al. (2003a), (53) Chiu et al. (2006), (54) Murray et al. (2011), (55) Strauss et al. (1999), (56) Gelino et al. (2011), (57) Knapp et al. (2004), (58) Biller et al. (2006), (59) Burningham et al. (2009), (60) Scholz et al. (2003), (61) Burgasser et al. (2006b), (62) Burgasser et al. (2010b), (63) Kasper et al. (2007), (64) Pinfield et al. (2008), (65) Luhman et al. (2011), (66) Faherty et al. (2012), (67) Dupuy & Liu (2012), (68) Vrba et al. (2004), (69) Subasavage et al. (2009), (70) Marocco et al. (2010), (71) Burgasser et al. (2008b), (72) Gaia Collaboration et al. (2018), (73) Cushing et al. (2016), (74) Smart et al. (2013), (75) van Altena et al. (1995), (76) Tinney et al. (2003), (77) Manjavacas et al. (2013), (78) Henry et al. (2006), (79) Harrington & Dahn (1980).

types and H - and/or $W2$ -band magnitudes to compute spectrophotometric distance estimates (Kirkpatrick et al. 2012) for those not already having measured parallaxes. Objects were retained in our list if their spectrophotometric distance estimates placed them within 22 pc (to account for distance uncertainties) or if they had published parallaxes good to 10% accuracy that placed them, within the measurement uncertainties, inside the 20 pc volume. This list of 235 objects is presented in Table 1. This table gives the discovery designation and reference in columns 1 and 2, the AllWISE designation in column 3, the measured infrared spectral type and its reference in columns 4 and 5, and the measured parallax and its reference in columns 6 and 7. For previously published parallax values in column 6, measurements of absolute parallax are commented with “(abs)” and those of relative parallax with “(rel).” In some cases, it is not clear whether the published value is an absolute or relative value, so those are left uncommented.

Of these 235 dwarfs in Table 1, 142 are being astrometrically monitored by our *Spitzer* program discussed in Section 4, 41 have high-accuracy parallax measurements from our ground-based programs discussed in Sections 6 and 7, and 49 have high-accuracy¹⁶ parallax measurements from the literature, although four of these are in common with objects in our own parallax programs. Only seven objects lack astrometric monitoring, and these were not added to our *Spitzer* programs because they either do not have any prior *Spitzer* measurements—and thus may not have had a large time baseline to decouple proper motion from parallax had we observed them only in Cycle 13—or were published after the Cycle 13 deadline; all of these, however, are being astrometrically monitored by us in our *Spitzer* Cycle 14 program. For these, the parallax values in column 6 are given in italics and are spectrophotometric estimates only. With one exception, these estimates take the apparent H and/or $W2$ magnitudes in Table 2 together with the spectral types in column 4 to compute distance estimates via the equations (those that include the WISE 1828+2650 data point) from Section 4.3 of Kirkpatrick et al. (2012). The sole exception is the parallax estimate of ULAS 0745+2332 (whose photometry was not extracted by the *WISE* pipeline), which is calculated from the minimum and maximum distance estimates provided by Burningham et al. (2008).

Photometry for these objects is given in Table 2. This table shows an abbreviated name from Table 1 in column 1, the H -band apparent magnitude and its reference in columns 2 and 3, and the *WISE* $W1$ through $W3$ magnitudes in columns 4 through 6. It should be noted that ground-based near-infrared photometry in both the J and H bands has been taken for many of these objects in one of two systems: either the Maunakea Observatories filter set (MKO; Tokunaga et al. 2002) or the filter set established by the Two Micron All Sky Survey (2MASS; Skrutskie et al. 2006). Because the J -band filter profiles between the two systems are very different, and the H -band profiles are nearly the same, we list in Table 2 only the H -band magnitudes since those can be intercompared regardless of the system used. Additional discussion on this point can be found in Section 3.1 of Kirkpatrick et al. (2011). Discussion of the measurements of *Spitzer* magnitudes in columns 7–8 and the Astronomical Observation Requests (AORs) from which they were measured can be found in Section 5.

4. *Spitzer* Observations

A list of 142 objects from Table 1 was astrometrically monitored with *Spitzer*/IRAC. Most of the *Spitzer* data came from programs 70062, 80109, 90007, 11059, and 13012 (Kirkpatrick, PI). The earliest of these programs, 70062 and 80109, were primarily aimed at photometric characterization of *WISE*-selected brown dwarf candidates using the 3.6 μm (hereafter, ch1) and 4.5 μm (hereafter, ch2) bandpasses of IRAC. In these two programs, a cycling dither pattern of medium scale and a five-position dither were used with frame times of 30 s in both channels. However, candidates with the reddest *WISE* $W1$ – $W2$ colors were also observed at subsequent epochs only in ch2 to provide early astrometric monitoring to supplement *Spitzer* astrometric programs planned for later. Additional photometric characterization of brown dwarf candidates selected later in the *WISE* mission was obtained in program 11059. In this program, ch1 and ch2 observations were obtained using a random dither pattern of medium scale and nine dither positions, again with frame times of 30 s. Our main astrometric monitoring campaigns were programs 90007 and 13012, which are described further below.

We chose ch2 for our astrometric follow-up for a variety of reasons, which are listed in Martin et al. (2018) but reiterated here. During *Spitzer* cryogenic operations, ch1 was more sensitive than ch2, but after cryogen depletion the deep image noise was found to be 12% worse in ch1 and 10% better in ch2, making the channels comparable in sensitivity for average field stars (ch1–ch2 \approx 0 mag; Carey et al. 2010). Another change during warm operations was the behavior of latent images from bright objects. Whereas latents in ch2 decay rapidly (typically within ten minutes), ch1 latents decay on timescales of hours. Moreover, the ch2 intra-pixel sensitivity variation (aka, the pixel phase effect) is about half that of ch1. Given these points, the fact that the point response function (PRF) is less undersampled in ch2 than in ch1, and the fact that our cold brown dwarfs are also much brighter in ch2 than in ch1 ($1.0 < \text{ch1} - \text{ch2} < 3.0$ mag), we choose to do our imaging in ch2.

Programs 90007 and 13012 were designed exclusively for astrometric monitoring, with program 90007 providing data to satisfy the minimum astrometric requirement and program 13012 extending the time baseline to improve the astrometric uncertainties. The Lutz–Kelker bias sets the fundamental requirement for the precision we targeted. The Lutz–Kelker effect, a systematic error inherent in the measurements of trigonometric parallax for a volume-limited set of stars, is induced as follows. Near the maximum distance, d_{max} , the volume of stars just inside, ($d_{\text{max}} - \Delta d$), is smaller than that just outside, ($d_{\text{max}} + \Delta d$), meaning that there are more stars able to scatter into the volume than can scatter outside. This means that the true average parallax is smaller than the average parallax that is measured. Figure 1 of Lutz & Kelker (1973) demonstrates that the astrometric error needed to correct this effect must be $\leq 15\%$ or else the effect is uncorrectable. For our distance limit of 20 pc (a parallax of 50 mas), this sets the error floor at 7.5 mas. Ideally, we would like to have errors even smaller; for example, an error of 10% (5 mas) reduces the bias on the absolute magnitude determination from 0.28 mag to 0.11 mag (see Table 1 of Lutz & Kelker 1973).

Our AORs for program 90007 were designed so targets were acquired with a signal-to-noise ratio (S/N) of ≥ 100 per epoch. Theoretically, the best astrometric precision we can expect from

¹⁶ We list the published parallax value with the smallest quoted errors, but only if it meets our goal of $< 10\%$ measurement uncertainty.

Table 2
(Continued)

Object Name (1)	<i>H</i> (mag) (2)	<i>H</i> Ref. (3)	<i>W1</i> (mag) (4)	<i>W2</i> (mag) (5)	<i>W3</i> (mag) (6)	ch1 (mag) (7)	ch2 (mag) (8)	AOR Used (9)
WISE 2209+2711	22.39 ± 0.15	15	>18.831	14.770 ± 0.055	12.455 ± 0.387	17.815 ± 0.087	14.739 ± 0.020	40821248
WISE 2209–2734	17.08 ± 0.05	1	16.314 ± 0.077	13.856 ± 0.041	>11.945	15.478 ± 0.025	13.899 ± 0.018	40819456
WISE 2211–4758	17.79 ± 0.04	43	17.470 ± 0.143	14.607 ± 0.051	12.508 ± 0.476	16.380 ± 0.035	14.618 ± 0.020	44572160
WISE 2212–6931	20.23 ± 0.04	15	17.259 ± 0.122	14.873 ± 0.061	>12.621	17.364 ± 0.063	14.973 ± 0.021	41770752
WISE 2213+0911	16.99 ± 0.11	1	16.579 ± 0.080	14.648 ± 0.060	>12.261	15.790 ± 0.028	14.564 ± 0.020	41523712
WISE 2220–3628	20.86 ± 0.04	15	>18.772	14.714 ± 0.056	>12.292	17.200 ± 0.057	14.736 ± 0.021	44552448
WISE 2226+0440	17.32 ± 0.02	1	16.864 ± 0.112	14.505 ± 0.055	>12.356	16.122 ± 0.031	14.543 ± 0.020	40837376
2MASS 2228–4310	15.36 ± 0.12	46	15.235 ± 0.040	13.326 ± 0.030	11.748 ± 0.273	14.453 ± 0.020	13.353 ± 0.018	45140736
WISE 2232–5730	19.20 ± 0.10	1	17.592 ± 0.178	15.201 ± 0.079	11.900 ± 0.315	17.435 ± 0.066	15.176 ± 0.022	41071616
WISE 2237+7228	15.94 ± 0.21	40	15.563 ± 0.037	13.592 ± 0.029	12.333 ± 0.332	14.607 ± 0.020	13.557 ± 0.018	44736000
WISE 2255–3118	17.70 ± 0.11	8	16.550 ± 0.079	14.161 ± 0.045	>11.932	15.914 ± 0.029	14.210 ± 0.019	40835584
WISE 2301+0216	16.70 ± 0.03	44	16.199 ± 0.066	14.343 ± 0.051	>12.104	15.601 ± 0.026	14.367 ± 0.019	44777728
WISE 2302–7134	17.79 ± 0.12	1	16.846 ± 0.081	14.240 ± 0.040	>12.594	15.991 ± 0.030	14.232 ± 0.019	41723904
WISE 2313–8037	17.28 ± 0.14	35	16.437 ± 0.054	13.676 ± 0.027	12.474 ± 0.363	15.289 ± 0.023	13.683 ± 0.018	41530368
WISE 2319–1844	18.00 ± 0.05	1	16.668 ± 0.087	13.822 ± 0.041	>11.779	15.919 ± 0.029	13.949 ± 0.018	41052928
ULAS 2321+1354	17.09 ± 0.06	44	16.937 ± 0.122	14.108 ± 0.059	>12.337	15.860 ± 0.028	14.191 ± 0.019	44757504
WISE 2325–4105	19.22 ± 0.11	8	17.064 ± 0.114	14.108 ± 0.040	>12.263	16.264 ± 0.033	14.086 ± 0.019	40827904
ULAS 2326+0201	18.46 ± 0.12	44	17.959 ± 0.293	15.531 ± 0.127	>12.354	16.879 ± 0.015	15.442 ± 0.016	45060352
WISE 2332–4325	19.57 ± 0.15	1	17.973 ± 0.240	14.958 ± 0.066	>12.210	17.271 ± 0.059	15.012 ± 0.021	40822272
WISE 2340–0745	16.19 ± 0.06	8	15.934 ± 0.058	13.600 ± 0.036	>11.921	15.194 ± 0.023	13.624 ± 0.018	40830208
ULAS 2342+0856	16.73 ± 0.03	44	15.969 ± 0.059	13.951 ± 0.042	>12.427	15.287 ± 0.024	13.987 ± 0.019	44765696
WISE 2343–7418	16.14 ± 0.04	1	15.669 ± 0.038	13.756 ± 0.031	12.786 ± 0.504	15.036 ± 0.022	13.752 ± 0.018	41727488
WISE 2344+1034	19.07 ± 0.11	8	18.137 ± 0.347	14.941 ± 0.078	>12.345	16.733 ± 0.042	14.907 ± 0.021	41060352
WISE 2348–1028	16.93 ± 0.12	8	16.647 ± 0.093	14.381 ± 0.051	>12.355	15.870 ± 0.028	14.357 ± 0.019	40831232
WISE 2354+0240	22.88 ± 0.30	15	>18.263	15.007 ± 0.085	>12.278	18.105 ± 0.109	15.013 ± 0.022	44790528
WISE 2357+1227	16.49 ± 0.03	44	15.742 ± 0.048	14.018 ± 0.040	12.101 ± 0.369	15.259 ± 0.023	14.103 ± 0.019	45154304

Notes. For resolved photometry of binaries, see Table 5 of Leggett et al. (2015). For VHS *H*-band magnitudes, the hAperMag3 was chosen, per the recommendations given at <http://horus.roe.ac.uk/vsa/dboverview.html>. The AperMag3 values from ULAS and UGPS were also the ones used. References for *H*-band magnitudes: (1) this paper, (2) Leggett et al. (2015), (3) Warren et al. (2007b), (4) Chiu et al. (2006), (5) Liu et al. (2007), (6) Leggett et al. (2010a), (7) Delorme et al. (2008), (8) Kirkpatrick et al. (2011), (9) UKIDSS—Lawrence et al. (2007), (10) Knapp et al. (2004), (11) Liu et al. (2011), (12) Pinfield et al. (2014b), (13) Leggett et al. (2013), (14) Leggett et al. (2017), (15) Schneider et al. (2015), (16) Luhman & Esplin (2016), (17) Leggett et al. (2002), (18) Lucas et al. (2010), (19) Pinfield et al. (2008), (20) Lodieu et al. (2007), (21) Leggett et al. (2009), (22) Burningham et al. (2013), (23) Wright et al. (2013), (24) Goldman et al. (2010), (25) Burningham et al. (2008), (26) Tsvetanov et al. (2000), (27) Burningham et al. (2010b), (28) Pinfield et al. (2012), (29) Geballe et al. (2001), (30) Scholz (2010b), (31) Strauss et al. (1999), (32) McCaughrean et al. (2004), (33) Kasper et al. (2007), (34) Cushing et al. (2014), (35) Kirkpatrick et al. (2012), (36) Burningham et al. (2009), (37) Pinfield et al. (2014a), (38) 2MASS Survey Point Source Reject Table—Skrutskie et al. (2006), (39) Albert et al. (2011), (40) Mace et al. (2013a), (41) Martin et al. (2018), (42) Dupuy et al. (2015), (43) VHS—McMahon et al. (2013), (44) ULAS—Warren et al. (2007a), (45) UGPS—Lucas et al. (2008), (46) 2MASS All-Sky Point Source Catalog—Skrutskie et al. (2006).

^a 0039+2115: *Spitzer* photometry is from Luhman et al. (2007).

^b 0521+3640: AllWISE *W1* photometry highly contaminated by the halo of a much brighter star.

^c 0807–6618: *W2* photometry is from a preliminary CatWISE detection (Meisner et al. 2018). *Spitzer* photometry is from Luhman et al. (2012).

^d 0855–0714: *W1* magnitude is measured by ELW from a moving coadd using eleven epochs of *WISE* and *NEOWISE* data between early 2010 and mid-2018. The epochs themselves are comprised of 177 individual exposures. The software includes one moving source (*WISE* 0855–0714 itself) and a grid of 275 fixed background sources that model the fixed celestial pattern. The two known interfering sources in the 2010 epochs (see Wright et al. 2014) are measured, free of contamination by *WISE* 0855–0714, and are allowed for when using the 2010 data. The fit, which uses a scaled PSF for each source (moving or fixed) and a flat background for each frame, is in principle immune to confusion noise. The resulting *W1* magnitude is much dimmer than the measurement made by Wright et al. (2014), which used only one epoch of *NEOWISE* Reactivation data. This new *W1* measurement is a 2.1σ detection (flux = $1.896 \pm 0.905 \mu\text{Jy}$; the most likely value is $1.809 \mu\text{Jy}$).

^e 1541–2250: *WISE* photometry is from the All-Sky Catalog.

a single measurement (see Equation (1) of Monet et al. 2010) is $\text{FWHM}/(2 \times \text{S/N}) = 1''.7/(2 \times 100) = 8.5 \text{ mas}$, where the FWHM is the ch2 value from Table 2.1 of the IRAC Instrument Handbook.¹⁷ However, our ability to fully correct for astrometric distortion keeps us from reaching this theoretical floor. We conservatively estimated that we could achieve $\sim 15 \text{ mas}$ precision after distortion is taken into account. Because we had already acquired earlier *Spitzer* epochs that would allow us to measure the proper motion and disentangle it from the parallax, we assumed that the error in the parallax would be roughly equal to the per-epoch-precision divided by the square root of the number of epochs measured in program 90007. For a per-epoch precision of 15 mas and a final parallactic error of $<10\%$, at least nine measurement epochs for each source were required. Hence, in program 90007, the per-

epoch goal of $\text{S/N} > 100$ per target was accomplished with a total ch2 integration time of 270 s acquired using a random dither pattern of medium scale, nine dither positions, and individual frame times of 30 s. This same procedure was used for program 13012.

Timing constraints were placed on the observations to optimize the measurement of parallax. The *Spitzer* viewing zone falls between 82.5° and 120° solar elongation, which encompasses the maximum parallax factor in ecliptic longitude (at 90°) critical to our program. For targets having two *Spitzer* visibility windows per year, one AOR was placed within 3.5 days of each maximum parallax factor. The other two or three AORs were evenly spaced through the rest of the visibility period. For targets near, but not in, the Continuous Viewing Zone, five or six observations were obtained at roughly evenly spaced intervals within each window, with an AOR landing within ± 3.5 days of each available maximum parallax factor. For targets located within the Continuous

¹⁷ See <https://irsa.ipac.caltech.edu/data/SPITZER/docs/irac/>.

Table 3
Objects on the IRAC ch2 *Spitzer* Parallax Program

Object Name (1)	First Obs. Date (UT) (2)	Last Obs. Date (UT) (3)	Baseline (yr) (4)	Program # (and # of Epochs) with ch2 Coverage (5)
WISE 0005+3737	2012 Sep 6	2017 Apr 22	4.6	80109(1), 90007(12), 13012(6)
WISE 0015-4615	2010 Dec 17	2017 Sep 10	6.7	70062(2), 90007(12), 13012(5)
WISE 0032-4946	2012 Jul 28	2017 Sep 12	5.1	80109(1), 90007(12), 13012(6)
2MASS 0034+0523	2012 Feb 15	2017 Apr 14	5.2	80109(2), 90007(12), 13012(6)
WISE 0038+2758	2012 Mar 22	2017 Apr 22	5.1	80109(2), 90007(14), 13012(6)
WISE 0049+2151	2012 Mar 22	2017 Apr 24	5.1	80109(2), 90007(12), 13012(6)
WISE 0123+4142	2011 Mar 25	2017 May 13	6.1	70062(1), 13012(6)
CFBDS 0133+0231	2012 Sep 13	2017 Apr 24	4.6	80109(1), 90007(12), 13012(6)
WISE 0146+4234AB	2011 Apr 5	2017 May 15	6.1	70062(1), 80109(2), 90007(12), 13012(6)
WISE 0221+3842	2011 Mar 31	2017 May 17	6.1	70062(1), 13012(6)
WISE 0226-0211AB	2010 Sep 18	2017 May 8	6.6	70062(2), 80109(1), 13012(6)
WISE 0233+3030	2012 Mar 22	2017 May 18	5.2	80109(2), 13012(6)
WISE 0241-3653	2011 Jan 19	2017 Apr 23	6.3	70062(1), 80109(2), 90007(12), 13012(6)
WISE 0247+3725	2011 Apr 12	2017 May 23	6.1	70062(1), 80109(1), 90007(12), 13012(6)
WISE 0302-5817	2015 Feb 10	2017 Oct 2	2.6	11059(1), 13012(8)
WISE 0304-2705	2014 Oct 20	2017 May 9	2.6	10135(1), 13012(6)
WISE 0309-5016	2010 Dec 22	2017 May 5	6.4	70062(1), 80109(2), 13012(6)
WISE 0313+7807	2010 Dec 21	2017 Jun 16	6.5	70062(2), 80109(2), 13012(6)
WISE 0316+4307	2011 Nov 19	2017 Jun 2	5.5	80109(1), 90007(12), 13012(6)
WISE 0323-5907	2010 Dec 18	2017 Apr 23	6.3	70062(2), 13012(6)
WISE 0323-6025	2010 Sep 18	2017 Apr 23	6.6	70062(2), 80109(1), 90007(10), 13012(5)
WISE 0325-5044	2011 Nov 19	2017 May 9	5.5	80109(1), 90007(10), 13012(5)
WISE 0325-3854	2011 Jan 30	2017 May 3	6.3	70062(1), 80109(1), 13012(6)
WISE 0325+0831	2011 Apr 12	2017 May 23	6.1	70062(1), 90007(12), 13012(6)
WISE 0335+4310	2011 Apr 19	2017 Jun 5	6.1	70062(1), 80109(1), 90007(12), 13012(6)
WISE 0336-0143	2011 Apr 12	2017 May 29	6.1	70062(1), 80109(1), 90007(12), 13012(6)
WISE 0350-5658	2010 Sep 18	2017 May 13	6.6	70062(2), 80109(2), 90007(10), 13012(6)
WISE 0359-5401	2010 Sep 18	2017 May 19	6.7	70062(2), 80109(2), 90007(12), 13012(5)
WISE 0404-6420	2011 Nov 20	2017 May 5	5.5	80109(1), 90007(10), 13012(5)
WISE 0410-1502	2010 Oct 21	2017 Jun 5	6.6	70062(2), 80109(2), 90007(12), 13012(6)
WISE 0413-4750	2011 Nov 19	2017 May 28	5.5	80109(1), 13012(6)
WISE 0430+4633	2012 Apr 19	2017 Jun 16	5.2	80109(1), 13012(6)
WISE 0458+6434AB	2010 Oct 29	2017 Jun 22	6.6	70062(2), 80109(1), 13012(6)
WISE 0500-1223	2010 Oct 18	2017 Jun 19	6.7	70062(2), 80109(1), 13012(6)
WISE 0512-3004	2010 Dec 19	2017 Jun 20	6.5	70062(2), 80109(1), 90007(12), 13012(6)
WISE 0535-7500	2010 Oct 17	2017 Sep 12	6.9	70062(2), 80109(2), 90007(10), 13012(6)
WISE 0540+4832	2012 Apr 23	2017 Jun 2	5.1	80109(1), 90007(12), 13012(4)
WISE 0614+0951	2010 Dec 17	2017 Jul 5	6.5	70062(2), 80109(2), 90007(12), 13012(6)
WISE 0645-0302	2012 Jan 7	2017 Jul 20	5.5	80109(1), 13012(6)
WISE 0647-6232	2010 Sep 19	2017 Sep 10	7.0	70062(2), 80109(1), 90007(10), 13012(6)
WISE 0713-5854	2012 Mar 20	2017 Oct 13	5.6	80109(1), 13012(5)
WISE 0713-2917	2012 Jan 2	2017 Aug 1	5.6	80109(1), 90007(12), 13012(6)
WISE 0723+3403	2010 Nov 25	2017 Jul 24	6.7	70062(2), 80109(1), 13012(6)
WISE 0734-7157	2011 Apr 19	2017 Aug 19	6.3	70062(1), 80109(1), 90007(10), 13012(5)
WISE 0744+5628	2011 Jun 2	2017 Jul 18	6.1	70062(1), 80109(2), 90007(12), 13012(6)
WISE 0759-4904	2011 Jan 2	2017 Sep 15	6.7	70062(2), 80109(1), 90007(10), 13012(6)
WISE 0812+4021	2010 Dec 9	2017 Aug 2	6.6	70062(2), 80109(1), 90007(12), 13012(6)
WISE 0825+2805	2012 Jan 7	2017 Aug 4	5.6	80109(2), 90007(12), 13012(6)
WISE 0833+0052	2013 Jan 3	2017 Aug 13	4.6	80077(1), 13012(6)
WISE 0836-1859	2011 Jan 1	2017 Aug 24	6.6	70062(2), 80109(1), 13012(6)
WISE 0855-0714	2013 Jun 21	2017 Aug 24	4.2	90095(3), 10168(4), 13012(6)
WISE 0857+5604	2010 Dec 18	2017 Aug 3	6.6	70062(2), 80109(1), 90007(12), 13012(6)
WISE 0906+4735	2010 Dec 23	2017 Aug 4	6.6	70062(2), 80109(2), 13012(6)
WISE 0914-3459	2012 Jun 19	2017 Sep 10	5.2	80109(1), 13012(6)
WISE 0940-2208	2012 Feb 3	2017 Sep 10	5.6	80109(1), 13012(6)
WISE 0943+3607	2010 Dec 23	2017 Aug 19	6.7	70062(2), 80109(1), 90007(12), 13012(6)
WISE 0952+1955	2011 Jan 1	2017 Aug 26	6.7	70062(2), 80109(2), 13012(6)
WISE 1018-2445	2011 Jan 26	2017 Sep 19	6.6	70062(1), 80109(2), 13012(6)
WISE 1025+0307	2012 Jul 7	2017 Sep 13	5.2	80109(1), 90007(11), 13012(6)
CFBDS 1028+5654	2010 Dec 20	2017 Aug 19	6.7	70021(1), 90007(12), 13012(6)
WISE 1039-1600	2011 Jan 26	2017 Sep 19	6.6	70062(1), 80109(1), 90007(12), 13012(6)
ULAS 1043+1048	2012 Feb 1	2017 Sep 09	5.6	70058(1), 13012(6)

Table 3
(Continued)

Object Name (1)	First Obs. Date (UT) (2)	Last Obs. Date (UT) (3)	Baseline (yr) (4)	Program # (and # of Epochs) with ch2 Coverage (5)
WISE 1050+5056	2012 Jun 12	2017 Aug 26	5.2	80109(1), 13012(6)
WISE 1051–2138	2011 Mar 13	2017 Sep 30	6.6	70062(1), 90007(11), 13012(6)
WISE 1052–1942	2011 Jan 31	2017 Sep 30	6.7	70062(1), 13012(6)
WISE 1055–1652	2012 Jul 16	2017 Sep 30	5.2	80109(1), 90007(9), 13012(6)
WISE 1124–0421	2012 Jul 19	2017 Sep 30	5.2	80109(1), 90007(11), 13012(6)
WISE 1139–3324	2012 Aug 22	2017 Oct 13	5.1	80109(1), 13012(7)
WISE 1141–3326	2012 Aug 22	2017 Oct 13	5.1	80109(1), 13012(7)
WISE 1143+4431	2012 Mar 04	2017 Sep 10	5.5	80109(1), 13012(6)
WISE 1150+6302	2010 Dec 23	2017 Aug 23	6.7	70062(2), 80109(1), 90007(12), 13012(6)
ULAS 1152+1134	2012 Mar 18	2017 Sep 28	5.5	80109(1), 13012(5)
WISE 1206+8401	2010 Dec 9	2017 Aug 3	6.6	70062(2), 80109(1), 90007(12), 13012(6)
WISE 1217+1626AB	2011 Mar 12	2017 Sep 30	6.6	70062(1), 80109(2), 13012(6)
WISE 1220+5407	2015 Feb 10	2017 Sep 10	2.6	11059(1), 13012(6)
WISE 1221–3136	2012 Aug 12	2017 May 19	4.8	80109(1), 90007(12), 13012(5)
WISE 1225–1013	2012 Mar 18	2017 Oct 12	5.6	80109(1), 90007(12), 13012(6)
2MASS 1231+0847	2012 Sep 1	2017 Oct 9	5.1	80109(1), 13012(6)
WISE 1243+8445	2011 Nov 21	2017 Jul 29	5.7	80109(1), 13012(6)
WISE 1254–0728	2012 Mar 30	2017 Oct 20	5.6	80109(1), 13012(8)
WISE 1257+4008	2011 Jan 29	2017 Sep 25	6.7	70062(1), 13012(6)
VHS 1258–4412	2012 Apr 21	2017 Jun 6	5.1	80109(1), 13012(6)
WISE 1301–0302	2012 Aug 22	2017 Oct 20	5.2	80109(1), 13012(8)
WISE 1318–1758	2011 Apr 12	2017 May 27	6.1	70062(1), 80109(2), 90007(12), 13012(5)
WISE 1333–1607	2011 Apr 12	2017 May 31	6.1	70062(1), 13012(5)
WISE 1405+5534	2011 Jan 22	2017 Oct 10	6.7	70062(1), 80109(2), 90007(10), 13012(6)
VHS 1433–0837	2011 Apr 19	2017 Jun 7	6.1	70062(1), 80109(2), 13012(6)
WISE 1436–1814	2011 Apr 19	2017 Jun 10	6.1	70062(1), 80109(2), 90007(12), 13012(6)
WISE 1448–2534	2012 Apr 29	2017 Jun 17	5.1	80109(1), 90007(12), 13012(6)
WISE 1501–4004	2012 Apr 21	2017 Jun 28	5.2	80109(1), 13012(6)
WISE 1517+0529	2012 Apr 4	2017 Jun 19	5.2	80109(1), 13012(6)
WISE 1519+7009	2010 Dec 9	2017 Sep 25	6.8	70062(2), 80109(1), 90007(10), 13012(6)
WISE 1523+3125	2011 Apr 16	2017 Jun 28	6.2	70062(1), 80109(2), 13012(6)
WISE 1541–2250	2011 Apr 13	2017 Jun 26	6.2	70062(1), 80109(2), 90007(12), 13012(6)
WISE 1542+2230	2011 Apr 18	2017 Jun 26	6.2	70062(1), 80109(2), 13012(6)
WISE 1612–3420	2010 Sep 18	2017 Jul 5	6.8	70062(2), 80109(1), 13012(6)
WISE 1614+1739	2010 Sep 20	2017 Jul 7	6.8	70062(2), 80109(2), 13012(6)
2MASS 1615+1340	2012 Apr 28	2017 Jul 7	5.2	80109(2), 90007(12), 13012(6)
WISE 1622–0959	2010 Sep 18	2017 Jul 5	6.8	70062(2), 80109(2), 13012(6)
WISE 1639–6847	2012 May 12	2017 Aug 1	4.2 ^a	80109(1), 90007(12), 11059(1), 13012(6)
WISE 1653+4444	2010 Sep 20	2017 May 31	6.7	70062(2), 80109(2), 90007(10), 13012(4)
WISE 1711+3500AB	2010 Sep 18	2017 Aug 24	6.9	70062(2), 80109(1), 90007(12), 13012(6)
WISE 1717+6128	2010 Sep 19	2017 Jul 15	6.8	70062(2), 80109(1), 13012(6)
WISE 1721+1117	2012 May 12	2017 Jul 24	5.2	80109(1), 13012(6)
WISE 1735–8209	2011 Jun 17	2017 Sep 7	6.2	70062(1), 13012(6)
WISE 1738+2732	2010 Sep 18	2017 Aug 14	6.9	70062(2), 80109(2), 90007(12), 13012(6)
WISE 1804+3117	2010 Sep 26	2017 Sep 4	6.9	70062(2), 80109(2), 13012(6)
WISE 1812+2007	2011 Jun 11	2017 Aug 15	6.2	70062(1), 80109(1), 13012(6)
WISE 1813+2835	2012 May 19	2017 Sep 1	5.3	80109(1), 90007(12), 13012(6)
WISE 1828+2650	2010 Jul 10	2017 Aug 30	7.1	551(1), 70062(1), 80109(2), 90007(12), 13012(6)
WISE 1928+2356	2012 Jun 21	2017 Sep 14	5.2	80109(1), 90007(12), 13012(6)
WISE 1955–2540	2011 Jun 26	2017 Aug 24	6.2	70062(1), 90007(11), 13012(6)
WISE 1959–3338	2011 Jun 7	2017 Aug 24	6.2	70062(2), 80109(2), 90007(12), 13012(6)
WISE 2000+3629	2012 Jul 18	2017 Oct 17	5.2	80109(1), 90007(12), 13012(7)
WISE 2005+5424	2010 Dec 31	2017 Sep 10	6.7	70062(2), 80109(1), 13012(7)
WISE 2015+6646	2010 Dec 31	2017 May 19	6.4	70062(2), 90007(10), 13012(5)
WISE 2017–3421	2011 Jun 9	2017 Sep 1	6.2	70062(1), 13012(6)
WISE 2019–1148	2011 Jun 15	2017 Sep 1	6.2	70062(1), 80109(2), 13012(6)
WISE 2056+1459	2010 Dec 10	2017 Oct 1	6.8	70062(2), 80109(2), 90007(12), 13012(6)
WISE 2147–1029	2010 Dec 22	2017 Sep 25	6.8	70062(2), 13012(6)
WISE 2157+2659	2010 Dec 23	2017 Sep 20	6.7	70062(2), 80109(2), 90007(12), 13012(6)
WISE 2159–4808	2011 Jun 22	2017 Sep 21	6.2	70062(2), 80109(1), 90007(12), 13012(6)
WISE 2203+4619	2014 Sep 22	2017 Oct 1	3.0	10135(1), 13012(7)

Table 3
(Continued)

Object Name (1)	First Obs. Date (UT) (2)	Last Obs. Date (UT) (3)	Baseline (yr) (4)	Program # (and # of Epochs) with ch2 Coverage (5)
WISE 2209+2711	2010 Dec 31	2017 Sep 23	6.7	70062(2), 80109(1), 90007(12), 13012(6)
WISE 2209–2734	2010 Dec 10	2017 Sep 23	6.8	70062(2), 80109(2), 90007(11), 13012(6)
WISE 2211–4758	2011 Nov 30	2017 Sep 19	5.8	80109(1), 13012(6)
WISE 2212–6931	2011 Jun 15	2017 Sep 22	6.3	70062(1), 80109(1), 90007(12), 13012(6)
WISE 2220–3628	2012 Jan 23	2017 Sep 24	5.7	80109(2), 90007(12), 13012(6)
WISE 2232–5730	2010 Nov 15	2017 Sep 24	6.9	70062(2), 13012(6)
WISE 2237+7228	2012 Apr 15	2017 Jun 2	5.1	80109(2), 90007(10), 13012(6)
WISE 2255–3118	2010 Dec 17	2017 Oct 6	6.8	70062(2), 80109(2), 13012(6)
WISE 2301+0216	2012 Jan 13	2017 Oct 16	5.8	80109(2), 90007(12), 13012(6)
WISE 2302–7134	2011 Jun 17	2017 Oct 7	6.3	70062(1), 13012(6)
WISE 2313–8037	2011 Jun 17	2017 Sep 22	6.3	70062(1), 80109(2), 90007(10), 13012(6)
WISE 2319–1844	2010 Dec 31	2017 Oct 12	6.8	70062(2), 80109(1), 90007(12), 13012(6)
ULAS 2321+1354	2009 Aug 19	2017 Oct 13	8.2	60093(1), 70021(1), 80109(2), 90007(12), 13012(7)
ULAS 2326+0201	2012 Jan 31	2017 Oct 9	5.7	80077(1), 13012(6)
WISE 2332–4325	2010 Dec 18	2017 Oct 12	6.8	70062(2), 80109(1), 90007(12), 13012(6)
WISE 2343–7418	2011 Jun 17	2017 Oct 7	6.3	70062(1), 80109(2), 90007(10), 13012(6)
WISE 2344+1034	2011 Jan 18	2017 Oct 4	6.7	70062(1), 80109(2), 13012(6)
WISE 2354+0240	2012 Sep 3	2017 Oct 4	5.1	80109(1), 13012(6)
WISE 2357+1227	2012 Sep 3	2017 Oct 7	5.1	80109(1), 13012(6)

Note.

^a 1639–6847: In the observation from program 80109 and the first observation from program 90007, the object is blended with a background source. This reduces the usable time baseline for astrometric measurements from 5.2 to 4.2 yr because the first clean image was taken on 2013 May 19 (UT).

Viewing Zone, 10–12 observations were used each year, again with an AOR falling within 3.5 days of each available maximum parallax factor. Slight adjustments to these constraints had to be made to fit within the calendar dates of each cycle, and other post facto adjustments were included when the observed data were corrupted by (rarely occurring) coronal mass ejection events from the Sun. These timing constraints were determined using a program written by one of us (ELW) that calculates the time of maximum parallax factor for each target using the predicted *Spitzer* ephemerides available from JPL Horizons.¹⁸

Although program 13012 was granted a full two years of observation and is ongoing, this paper uses only those data taken by 2017 October 20 (UT). This date was chosen so that each target will have been observed through at least two maximum parallax factors in *Spitzer* Cycle 13. Future Cycle 13 observations along with data from our new Cycle 14 program (discussed further in Section 11) to be completed in 2019 November, will be included in a subsequent paper presenting our final parallactic measurements. A listing of the first and last observation date, total time baseline, and number of AORs per program for each target is given in Table 3.

For a few targets, the disentangling of proper motion from parallax benefited from using ch2 observations taken prior to our own:

1. WISE 0304–2705 and WISE 2203+4619: We supplemented our data with an earlier observation from program 10135 (D.J. Pinfield, PI) that used a 16 point spiral dither pattern with medium spacing, two frames at each dither position, and exposure times of 30 s per frame.
2. WISE 0833+0052 and ULAS 2326+0201: We used an earlier observation from program 80077 (S.K. Leggett,

PI) that used a 12 point Reuleaux dither pattern with medium spacing, four frames at each dither position, and exposure times of 30 s per frame.

3. WISE 0855–0714: We used earlier observations from programs 90095 and 10168 (K.L. Luhman, PI). Program 90095 acquired three separate epochs on the target object, using a five-point Gaussian dither with small spacing and exposure times of 30 s per frame. Program 10168 acquired four separate epochs using a nine-point random dither pattern of small spacing and exposure times of 30 s per frame.
4. CFBDS 1028+5654: An earlier observation from program 70021 (K.L. Luhman, PI) was used to extend our time baseline. This program acquired data using a five-point Gaussian dither with small spacing, one frame per dither position, and exposure times of 30 s per frame.
5. ULAS 1043+1048: An observation from program 70058 (S.K. Leggett, PI) was used to extend the time baseline for this object. This program took data using a 16 point spiral dither pattern with medium spacing, six frames at each dither position, and exposure times of 30 s per frame.
6. WISE 1828+2650: Data from program 551 (A.K. Mainzer, PI) were the first taken as part of the *WISE* brown dwarf team’s follow-up of *WISE* color-selected objects. This program, which targeted only WISE 1828+2650 at a single epoch, used a 12 point Reuleaux dither pattern with medium spacing, one frame per dither position, and exposure times of 12 s per frame.
7. ULAS 2321+1354: Program 60093 (S.K. Leggett, PI) provided a supplemental data point for this object. Data were taken using a five-point Gaussian dither pattern with medium spacing, one frame per dither, and exposure times of 30 s per frame.

¹⁸ See <https://ssd.jpl.nasa.gov/?horizons>.

5. *Spitzer* Reductions

5.1. Photometry in *ch1* and *ch2*

With the exception of Gl 27B (Luhman et al. 2007) and WD 0806–661B (Luhman et al. 2012), the *Spitzer* photometry for all sources was measured by CRG and JDK as follows. For each object, we performed aperture photometry on an AOR that included both *ch1* and *ch2* data so that measurements were contemporaneous. These aperture measurements were done either on custom mosaics of the corrected basic calibrated data (CBCD) frames or on the post-basic calibrated data (pBCD) mosaics archived at the *Spitzer* Heritage Archive at IRSA¹⁹ using the MOsaicker and Point Source EXtractor with point-source extraction package (MOPEX/APEX), also available at IRSA. As mentioned in Kirkpatrick et al. (2011), for objects as bright as our targets, we have seen negligible difference in the photometry between the two methods. Our scripts used a 4 pixel aperture (*aperture1* in the MOPEX output files) with a 24 to 40 pixel sky annulus. Resultant raw fluxes were then multiplied by the aperture corrections recommended in Table 4.7 of the IRAC Instrument Handbook, also available at IRSA—1.208 for *ch1* and 1.221 for *ch2*—to obtain the flux in units of μJy , and then converted to magnitudes using the flux zero points in the Handbook’s Table 4.1 (280.9 ± 4.1 Jy in *ch1* and 179.7 ± 2.6 Jy in *ch2*), propagating the uncertainty in zero-point and flux into the final measurement error. This resulting photometry, along with the AOR number from which the photometry was extracted, is given in columns 7–9 of Table 2.

5.2. Astrometry in *ch2*

Our basic astrometric reduction methodology is discussed in detail in Martin et al. (2018). Whereas ECM wrote Python code for the reductions presented in that paper, JDK wrote independent Interactive Data Language (IDL) code and other wrappers for the reductions presented here, and those included one fundamental change to improve astrometric repeatability. We outline the basic steps below.

5.2.1. Identifying *Gaia* Astrometric Anchor Points

For each AOR, we created a mosaic from the individual CBCD frames and extracted astrometry and photometry of detected sources using the MOPEX/APEX software. We examined the resulting mosaics at all epochs to ensure that the target object was near the center of the field, as expected. (This step eliminated three AORs for WISE 2301+0216—46523392, 46523136, and 46522880—from further use, due to a typographical error in the requested pointings for those epochs.) In addition to these per-epoch mosaics, we also created a supermosaic and associated source list by combining all available CBCD files for each object over the full time baseline. We then used the *match2* routine in the Starlink Tables Infrastructure Library Tool Set (STILTS; Taylor 2006) and a three-arcsecond radius to match sources from each per-epoch mosaic source list to the supermosaic source list. Parameters were set so that we retained for each supermosaic source only the closest match in the per-epoch source list (*find = best1*) and listed only those supermosaic sources having a match (*join = 1and2*).

We then used the IDL to perform a preliminary re-registration on each per-epoch mosaic to place it on the same

astrometric grid as the supermosaic. Only those objects with $S/N \gtrsim 30$ on the per-epoch mosaics were used. We found that a simple translation in R.A. and decl. provided excellent results. The per-frame offsets were computed by performing a robust mean of the offsets and including a 3σ clipping of outliers. We uploaded this list of high- S/N re-registration stars into IRSA and matched to the *Gaia* Data Release 1 (DR1) catalog using a one-arcsecond search radius. Most of these stars have *Gaia* matches, since they are bright at both *Gaia* *G* band and IRAC *ch2* band, but we dropped any *Gaia* matches for which the *Gaia* DR1 astrometric uncertainties were $\gtrsim 100$ mas.

Once the *Gaia* astrometric anchor stars had been identified in each field, more precise refinements to the astrometry could be performed, since the *Gaia* DR1 positions for these well detected objects typically have uncertainties of under a milliarcsecond. Originally, we wrote code like that described in Martin et al. (2018), to do these refinements on the source lists derived from the per-epoch mosaics, but we found that this was degrading our final astrometric precision. After some experimentation, we concluded that the mosaicking step in MOPEX was responsible. As described below, the actual astrometric measurements for this paper use source positions as measured on the individual *frames*, not the per-epoch mosaics.

5.2.2. Astrometric Refinements to Frame Source Positions

For each AOR, we ran scripts in MOPEX/APEX to measure the positions and photometry of our target and its associated re-registration stars on each individual frame. These scripts used the CBCD, uncertainty (CBUNC), and mask (BIMSK) files available in the *Spitzer* Heritage Archive. Data were pulled from the *Spitzer* Heritage Archive after all image headers had been updated by the *Spitzer* Science Center to incorporate the new fifth-order correction to the array distortion²⁰ (Lowrance et al. 2014, 2016). PRF fitting was done using a set of warm PRFs built by one of us (JGI), adapted from the cold mission PRFs to mimic the intrapixel gain variations measured with warm IRAC. Because the optical path did not change from the cold to warm *Spitzer* missions, the optical point-spread function (PSF) did not change, only the overall detector sensitivity. In other words, while the dynamic range of the PRF has changed, its spatial structure has not. As usual, the PRFs we used are tabulated images of point sources at various sub-pixel offsets and therefore strongly mitigate the astrometric bias caused by intrapixel distortion (Ingalls et al. 2012, 2014), which is a consequence of the fact that IRAC data are undersampled and the intrinsic sensitivity of an IRAC detector is not uniform across a pixel. While this analysis was underway, warm mission PRFs developed by Hora et al. (2012) were released on the IRSA website,²¹ but, as expected, the astrometric differences between the official PRFs and the ones used here were found to be negligible.

The resulting, native astrometry of the re-registration stars on each frame was then compared to the *Gaia* DR1 positions of these same sources. Specifically, we used the (*x*, *y*) positions computed by APEX and translated these into (R.A., decl.) using the World Coordinate System (WCS) information in the frame FITS header.²² Naively, one would assume that the (*x*, *y*)

¹⁹ See <http://irsa.ipac.caltech.edu>.

²⁰ See also https://irachpp.spitzer.caltech.edu/page/dist_correct.

²¹ See <http://irsa.ipac.caltech.edu/data/SPITZER/docs/irac/calibrationfiles/>.

²² Note that FITS and APEX use the convention that the first pixel is located at (1, 1), whereas IDL convention places this at (0, 0).

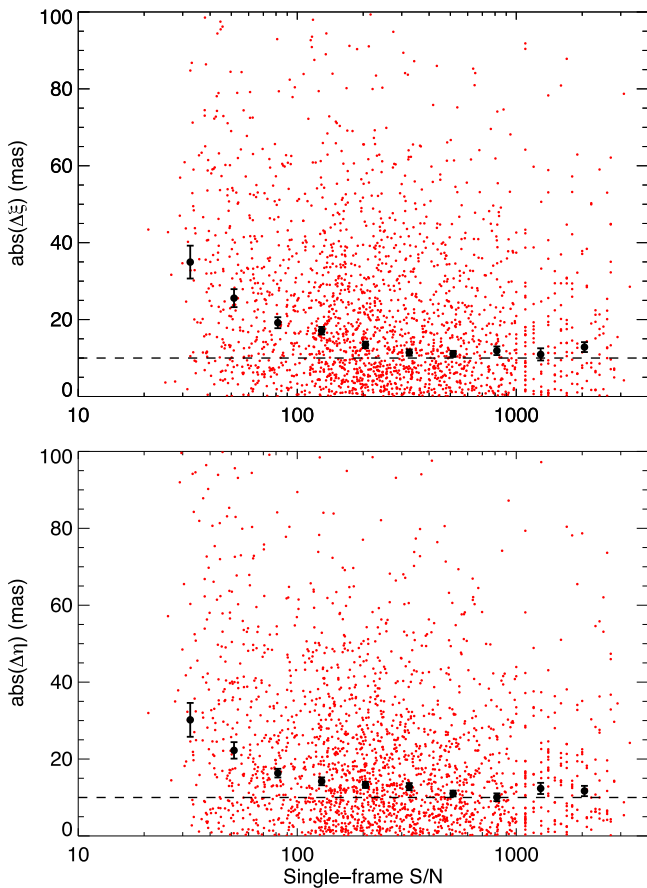


Figure 1. Astrometric repeatability as a function of the single-frame signal-to-noise ratio. Plotted in red are the per-axis differences in position (ξ in the top panel and η in the bottom) between our measurements and those of *Gaia* DR1. These are the mean position in the AOR determined from the (generally) nine independent measurements in each individual frame. Shown in the figure are sources from one representative AOR from each of our 142 targets, excepting 19 with $|\beta| < 15^\circ$ that have been removed since their higher source densities would otherwise dominate the plot. The black points are robust means—determined with a 1σ clipping to remove outliers—that sample 10 S/N bins over the range $25 < S/N < 2500$ using logarithmic spacing. As shown by the dashed black lines, an asymptotic floor of ~ 10 mas is reached at very high S/N values.

positions reported by APEX would be true array coordinates, but through experimentation we determined that these positions are actually rubber-sheeted versions; i.e., ones with the fifth-order distortion correction already included. Hence, we were able to convert to (R.A., decl.) using the WCS specifications only.

With the (x, y) -derived sky positions in hand for both the re-registration stars and the target, we converted all to tangent plane coordinates (ξ, η) , where we used the mean position of our target across all epochs as the tangent point itself; i.e., $(\xi, \eta) = (0, 0)$. We then computed the $(\Delta\xi, \Delta\eta)$ values between the (x, y) -derived sky positions for the re-registration stars and their *Gaia* reported positions, and computed a robust mean of the differences using 3σ outlier clipping and a simple (ξ, η) translation. These mean differences were then used to place the (ξ, η) coordinates of the target object and re-registration stars onto the *Gaia* reference frame.

For most of our targets, we were able to find a sufficient number of *Gaia* DR1 stars above a single-frame S/N value of 100 to perform an adequate re-registration. For some targets in sparser fields, however, as few as three re-registration stars were found

above $S/N = 100$. (For the two targets closest to the Galactic Center, WISE 1928+2356 and WISE 2000+3629, we had the opposite problem of too many potential re-registration stars, so we reset the selection threshold for re-registration stars to $S/N > 500$.) For any target having 10 or more re-registration stars with $S/N \geq 100$, we found that the inclusion of re-registration stars with $30 < S/N < 100$ did not generally decrease the reduced χ^2 values in the final proper motion and parallax fits. For targets having fewer than 10 re-registration stars with $S/N \geq 100$, however, these reduced χ^2 values were generally much better. For these targets, a single-frame S/N floor of ~ 30 was used for selection of the re-registration stars. With this adjustment, no fewer than five re-registration stars were used for each field.

For the target object, the robust mean of these per-frame adjusted positions (again using 3σ clipping) was used as the measured position of the object for this AOR. For the astrometric uncertainty on each AOR position, we use a measurement of the positional repeatability for stars lying at a S/N value similar to the target. Figure 1 illustrates this repeatability. The plot demonstrates that our target T and Y dwarfs, which lie in the single-frame S/N range between 70 and 200, have per-axis astrometric precisions of ~ 15 mas. There are some AORs for which, due to small number statistics, this measured repeatability falls below 10 mas. For these, we set a floor of 10 mas on the per-axis positional uncertainty of the target, since the broader analysis in Figure 1 shows this is the best we actually achieve. For each AOR, the mean (ξ, η) position of the target was then converted back to (R.A., decl.). The FITS header of the middle frame in each AOR was then consulted for the UT date and barycentric (X, Y, Z) position of the *Spitzer Space Telescope* at the time of observation.

5.2.3. Fitting for Proper Motion and Parallax

For each target, our list of measured astrometry and its uncertainties along with the observation times and locations of the observing platform were fed into a least-squares fitting code to determine the proper motion, parallax, and position at a fiducial time. We supply two nonlinear equations (see Smart 1977; Green 1985; Beichman et al. 2014) to the code:

$$\alpha_{\text{residual}} = (\alpha(t) - \alpha') \cos \delta' - \pi_{\text{trig}}(X(t) \sin \alpha' - Y(t) \cos \alpha') / 3600 \quad (1)$$

$$\delta_{\text{residual}} = \delta(t) - \delta' - (\pi_{\text{trig}}(X(t) \cos \alpha' \sin \delta' + Y(t) \sin \alpha' \sin \delta' - Z(t) \cos \delta')) / 3600 \quad (2)$$

where

$$\alpha' = \alpha_0 + (\mu_\alpha(t - t_0)) / \cos \delta' / 3600 \quad (3)$$

$$\delta' = \delta_0 + (\mu_\delta(t - t_0)) / 3600. \quad (4)$$

Here, $\alpha(t)$ and $\delta(t)$ are the R.A. and decl. positions (and their uncertainties) of the target in degrees; $X(t)$, $Y(t)$, and $Z(t)$ are the locations of the spacecraft in astronomical units; t_0 is a fiducial time in years; α_0 and δ_0 are the R.A. and decl. in degrees at time t_0 ; μ_α and μ_δ are the R.A. and decl. components of the proper motion in arcsec yr^{-1} ; and π_{trig} is the trigonometric parallax in arcseconds. We employed the IDL module `mpfitfun` (Markwardt 2009), which uses the Levenberg–Marquardt least-squares algorithm to attempt to drive both α_{residual} and δ_{residual} simultaneously to zero, given the observational data and their uncertainties.

Table 4
Parallax and Motion Fits for Objects on the *Spitzer* Parallax Program

Object Name	J2000 R.A. Ep. 2014.0 (deg)	R.A. Unc. (mas)	J2000 Decl. Ep. 2014.0 (deg)	Decl. Unc. (mas)	π_{abs} (mas)	corr_{π} (mas)	$\mu_{\text{R.A.}}$ (mas yr ⁻¹)	$\mu_{\text{Decl.}}$ (mas yr ⁻¹)	χ^2	Dof	Red. χ^2	# of Ep.	# of Reg. Stars ^a
(1)	(2)	(3)	(4)	(5)	(6)	(7)	(8)	(9)	(10)	(11)	(12)	(13)	(14)
WISE 0005+3737	1.324120	2.6	37.622066	2.5	127.0 ± 2.4	1.3 ± 0.4	998.9 ± 1.4	-267.0 ± 1.4	19.925	33	0.604	19	22H
WISE 0015-4615	3.775288	2.7	-46.255526	2.6	71.8 ± 2.7	1.5 ± 0.5	409.7 ± 1.5	-682.9 ± 1.3	30.137	33	0.913	19	15L
WISE 0032-4946	8.128906	3.3	-49.781951	3.0	63.6 ± 2.9	1.4 ± 0.3	-379.3 ± 1.7	-858.1 ± 1.7	28.256	33	0.856	19	13L
2MASS 0034+0523	8.717410	3.3	5.385402	3.7	120.1 ± 3.0	1.6 ± 0.4	672.6 ± 1.7	184.7 ± 1.9	17.909	35	0.512	20	16L
WISE 0038+2758	9.621136	2.5	27.981175	2.5	89.7 ± 2.5	1.5 ± 0.6	-15.4 ± 1.6	96.3 ± 1.5	37.107	39	0.951	22	12H
WISE 0049+2151	12.439742	2.5	21.855396	2.5	139.9 ± 2.5	1.5 ± 0.5	-483.2 ± 1.4	-46.5 ± 1.4	18.928	35	0.541	20	15L
WISE 0123+4142	20.889465	8.1	41.701367	5.6	44.0 ± 4.1	1.3 ± 0.3	601.7 ± 2.6	91.5 ± 1.9	5.439	9	0.604	7	10H
CFBDS 0133+0231	23.260890	3.7	2.524552	2.7	56.3 ± 3.4	2.2 ± 1.2	598.0 ± 2.0	-113.9 ± 1.5	44.910	33	1.361	19	8L
WISE 0146+4234AB	26.735580	2.4	42.569411	2.3	52.5 ± 2.3	1.3 ± 0.3	-452.0 ± 1.2	-27.9 ± 1.2	58.434	37	1.579	21	21H
WISE 0221+3842	35.275000	5.9	38.701001	5.6	36.0 ± 4.1	1.5 ± 0.5	139.6 ± 1.9	-21.7 ± 1.8	10.011	9	1.112	7	13H
WISE 0226-0211AB	36.599702	6.0	-2.195477	5.1	57.3 ± 4.7	0.6 ± 0.1	-294.9 ± 2.1	-436.9 ± 1.7	307.384	13	23.645	9	11L
WISE 0233+3030	38.325104	6.7	30.508434	6.2	31.3 ± 4.2	1.6 ± 0.4	-134.6 ± 2.3	-29.5 ± 2.2	11.591	11	1.054	8	16H
WISE 0241-3653	40.353413	2.4	-36.891001	2.6	52.4 ± 2.7	1.6 ± 0.2	242.0 ± 1.5	148.4 ± 1.4	26.606	37	0.719	21	8H
WISE 0247+3725	41.810711	2.4	37.422967	2.4	64.8 ± 2.6	1.5 ± 0.6	25.3 ± 1.3	-83.2 ± 1.3	23.715	33	0.719	19	21H
WISE 0302-5817	45.656121	14.5	-58.294668	15.9	56.1 ± 4.4	1.3 ± 0.3	41.2 ± 4.9	-76.4 ± 5.2	21.135	13	1.626	9	15L
WISE 0304-2705	46.204500	19.4	-27.085116	17.1	81.5 ± 7.7	1.6 ± 0.3	128.0 ± 7.0	497.2 ± 6.5	25.307	9	2.812	7	5L
WISE 0309-5016	47.332887	4.9	-50.270419	4.3	66.8 ± 3.9	1.8 ± 0.8	521.5 ± 1.7	203.6 ± 1.5	6.397	13	0.492	9	16L
WISE 0313+7807	48.358936	3.5	78.129054	3.6	134.3 ± 3.6	1.0 ± 0.3	71.1 ± 1.2	54.8 ± 1.2	19.065	15	1.271	10	46L
WISE 0316+4307	49.102234	3.0	43.118785	2.8	73.3 ± 2.8	1.0 ± 0.3	372.4 ± 1.5	-225.9 ± 1.5	28.850	27	1.069	16	33H
WISE 0323-5907	50.788921	4.9	-59.130369	5.9	71.5 ± 4.3	1.5 ± 0.6	519.1 ± 1.6	499.6 ± 2.0	16.304	11	1.482	8	18L
WISE 0323-6025	50.907543	2.7	-60.431966	2.8	71.4 ± 2.9	1.5 ± 1.0	506.7 ± 1.3	-173.5 ± 1.5	25.616	31	0.826	18	19L
WISE 0325-3854	51.324053	5.3	-38.915158	6.2	57.2 ± 5.4	1.6 ± 0.5	283.7 ± 1.9	-107.0 ± 1.8	3.098	11	0.282	8	13L
WISE 0325-5044	51.268421	2.9	-50.733514	3.1	36.7 ± 2.7	1.5 ± 0.4	84.6 ± 1.5	-154.3 ± 1.6	121.079	27	4.484	16	21L
WISE 0325+0831	51.449038	3.1	8.521650	3.4	78.5 ± 3.0	1.4 ± 0.3	116.2 ± 1.8	-38.1 ± 1.7	21.917	33	0.664	19	12L
WISE 0335+4310	53.813849	2.4	43.178366	2.3	72.1 ± 2.4	1.0 ± 0.2	825.7 ± 1.2	-787.0 ± 1.2	112.945	35	3.227	20	52H
WISE 0336-0143	54.020859	2.4	-1.732166	2.4	99.0 ± 2.4	1.7 ± 0.4	-257.8 ± 1.2	-1212.3 ± 1.2	55.719	35	1.592	20	20H
WISE 0350-5658	57.501000	2.7	-56.975637	2.7	174.6 ± 2.6	1.4 ± 0.4	-216.5 ± 1.3	-579.0 ± 1.4	28.501	35	0.814	20	20L
WISE 0359-5401	59.891824	2.5	-54.032512	2.6	75.8 ± 2.5	1.5 ± 0.4	-143.0 ± 1.3	-774.8 ± 1.5	92.938	37	2.512	21	16L
WISE 0404-6420	61.181138	3.0	-64.341730	2.9	45.7 ± 2.7	1.8 ± 0.6	-46.8 ± 1.6	-50.2 ± 1.6	38.537	27	1.427	16	11H
WISE 0410+1502	62.595853	2.3	15.044417	2.2	150.2 ± 2.4	1.5 ± 0.5	954.2 ± 1.1	-2213.3 ± 1.1	39.350	39	1.009	22	20H
WISE 0413-4750	63.492451	7.1	-47.843983	7.8	48.2 ± 4.8	1.5 ± 0.6	110.6 ± 2.3	302.2 ± 2.6	9.477	9	1.053	7	18L
WISE 0430+4633	67.721883	6.9	46.559111	6.7	93.9 ± 4.1	0.4 ± 0.1	879.7 ± 2.3	383.8 ± 2.2	2.835	9	0.315	7	63H
WISE 0458+6434AB	74.725158	3.7	64.581566	3.8	109.2 ± 3.6	1.2 ± 0.2	207.7 ± 1.2	291.2 ± 1.2	2.470	13	0.190	9	16H
WISE 0500-1223	75.012144	3.9	-12.394828	3.7	95.1 ± 3.6	1.3 ± 0.6	-536.5 ± 1.3	493.1 ± 1.2	6.578	13	0.506	9	26L
WISE 0512-3004	78.036948	2.4	-30.067509	2.5	48.9 ± 2.6	1.2 ± 0.4	614.2 ± 1.2	187.6 ± 1.3	72.645	37	1.963	21	23L
WISE 0535-7500	83.819481	2.4	-75.006736	2.4	66.4 ± 2.4	1.4 ± 0.5	-123.7 ± 1.1	19.6 ± 1.1	45.380	33	1.375	19	32H
WISE 0540+4832	85.196268	2.5	48.541582	2.5	70.0 ± 2.6	0.8 ± 0.1	246.0 ± 1.5	-626.9 ± 1.5	41.240	29	1.422	17	58H
WISE 0614+0951	93.657701	2.2	9.859608	2.2	65.6 ± 2.2	0.6 ± 0.1	387.0 ± 1.1	-149.8 ± 1.1	39.525	39	1.013	22	74H
WISE 0645-0302	101.368293	4.5	-3.047051	6.5	50.7 ± 4.2	0.4 ± 0.1	-0.8 ± 1.2	-318.9 ± 2.0	10.993	9	1.221	7	55H
WISE 0647-6232	101.846795	2.3	-62.542827	2.4	100.3 ± 2.4	1.3 ± 0.6	2.2 ± 1.0	387.9 ± 1.1	76.198	33	2.309	19	20H
WISE 0713-2917	108.344415	2.5	-29.298188	2.5	107.5 ± 2.4	1.0 ± 0.2	356.5 ± 1.3	-413.8 ± 1.3	28.123	33	0.852	19	87H
WISE 0713-5854	108.257861	6.7	-58.912164	7.5	78.2 ± 4.6	1.6 ± 0.6	82.2 ± 2.1	358.2 ± 2.3	12.659	7	1.808	6	20H
WISE 0723+3403	110.802009	3.8	34.053368	3.7	56.3 ± 3.5	0.5 ± 0.1	-5.0 ± 1.2	-343.8 ± 1.2	28.654	13	2.204	9	40L
WISE 0734-7157	113.681527	2.5	-71.962324	2.5	75.0 ± 2.4	1.2 ± 0.4	-565.5 ± 1.3	-78.9 ± 1.3	88.425	29	3.049	17	21H
WISE 0744+5628	116.238838	2.3	56.471738	2.4	67.1 ± 2.5	1.8 ± 0.6	153.6 ± 1.2	-764.4 ± 1.2	44.682	37	1.208	21	10H

Table 4
(Continued)

Object Name	J2000 R.A. Ep. 2014.0 (deg)	R.A. Unc. (mas)	J2000 Decl. Ep. 2014.0 (deg)	Decl. Unc. (mas)	π_{abs} (mas)	corr $_{\pi}$ (mas)	$\mu_{\text{R.A.}}$ (mas yr $^{-1}$)	$\mu_{\text{Decl.}}$ (mas yr $^{-1}$)	χ^2	Dof	Red. χ^2	# of Ep.	# of Reg. Stars ^a
(1)	(2)	(3)	(4)	(5)	(6)	(7)	(8)	(9)	(10)	(11)	(12)	(13)	(14)
WISE 0759–4904	119.945205	2.4	–49.081446	2.4	89.1 ± 2.4	0.7 ± 0.1	–367.0 ± 1.1	244.3 ± 1.1	21.246	33	0.644	19	55H
WISE 0812+4021	123.084041	2.6	40.351692	2.3	34.2 ± 2.7	1.5 ± 0.7	258.0 ± 1.3	28.8 ± 1.1	74.070	37	2.002	21	20L
WISE 0825+2805	126.280555	2.5	28.096544	2.4	155.8 ± 2.4	1.4 ± 0.2	–63.1 ± 1.3	–232.8 ± 1.2	34.192	35	0.977	20	14H
WISE 0833+0052	128.408480	8.8	0.869044	7.8	82.6 ± 4.5	1.4 ± 0.5	790.1 ± 2.8	–1590.7 ± 2.5	4.356	9	0.484	7	21H
WISE 0836–1859	129.171466	4.0	–18.996471	3.8	40.8 ± 3.6	1.0 ± 0.2	–47.6 ± 1.3	–150.5 ± 1.2	67.391	13	5.184	9	19H
WISE 0855–0714	133.787057	4.5	–7.244431	4.5	438.9 ± 3.0	1.3 ± 0.3	–8118.9 ± 1.9	679.3 ± 1.9	11.154	21	0.531	13	24H
WISE 0857+5604	134.316277	2.3	56.068512	2.5	87.2 ± 2.4	1.3 ± 0.2	–714.8 ± 1.1	–233.5 ± 1.2	43.297	37	1.170	21	12L
WISE 0906+4735	136.704848	3.5	47.593343	3.6	48.4 ± 3.4	1.5 ± 0.2	–545.9 ± 1.2	–709.6 ± 1.2	19.197	15	1.280	10	15L
WISE 0914–3459	138.537222	7.4	–34.994793	7.0	45.2 ± 4.2	1.1 ± 0.2	–19.7 ± 2.2	175.9 ± 2.2	12.900	9	1.433	7	30H
WISE 0940–2208	145.083635	7.3	–22.138988	7.7	38.1 ± 4.7	1.3 ± 0.3	–144.9 ± 2.3	171.2 ± 2.3	5.652	9	0.628	7	14H
WISE 0943+3607	145.775825	2.6	36.122729	2.7	93.8 ± 2.8	1.8 ± 0.9	675.1 ± 1.3	–498.9 ± 1.4	68.309	37	1.846	21	9L
WISE 0952+1955	148.247005	5.1	19.918980	3.7	41.1 ± 3.9	1.4 ± 0.2	–34.4 ± 1.6	–32.1 ± 1.2	18.487	15	1.232	10	13L
WISE 1018–2445	154.533566	4.0	–24.766900	4.0	83.6 ± 3.6	1.0 ± 0.3	54.3 ± 1.3	–821.4 ± 1.3	9.697	13	0.746	9	23L
WISE 1025+0307	156.489211	2.7	3.132060	2.7	85.4 ± 2.5	1.7 ± 0.5	–1199.3 ± 1.4	–144.4 ± 1.3	27.257	31	0.879	18	10H
CFBDS 1028+5654	157.171475	3.2	56.900364	2.8	45.0 ± 2.9	1.4 ± 0.2	200.8 ± 1.5	–12.1 ± 1.4	33.048	33	1.001	19	19L
WISE 1039–1600	159.782034	2.9	–16.000912	2.5	53.4 ± 2.6	1.4 ± 0.4	–189.1 ± 1.5	–119.7 ± 1.2	27.613	35	0.789	20	13H
ULAS 1043+1048	160.980791	9.7	10.800797	6.9	20.8 ± 7.0	1.6 ± 0.3	95.4 ± 3.0	–105.1 ± 2.1	11.428	9	1.270	7	11L
WISE 1050+5056	162.698915	8.0	50.934880	7.4	49.7 ± 5.0	1.8 ± 0.7	–427.5 ± 2.5	–64.0 ± 2.2	26.459	9	2.940	7	15L
WISE 1051–2138	162.875232	3.3	–21.650044	2.8	67.0 ± 3.0	1.1 ± 0.3	137.1 ± 1.5	–156.4 ± 1.3	27.284	31	0.880	18	19L
WISE 1052–1942	163.241771	7.0	–19.714310	5.9	62.3 ± 4.4	1.3 ± 0.4	326.2 ± 2.1	–315.1 ± 1.7	7.594	9	0.844	7	28L
WISE 1055–1652	163.972545	3.0	–16.870933	3.0	72.2 ± 2.7	1.5 ± 0.8	–991.3 ± 1.4	414.9 ± 1.4	28.055	27	1.039	16	13H
WISE 1124–0421	171.158218	3.4	–4.363736	3.2	61.6 ± 3.1	1.5 ± 0.2	–552.4 ± 1.8	67.6 ± 1.4	16.601	31	0.536	18	7H
WISE 1139–3324	174.955011	7.5	–33.407093	7.2	27.0 ± 3.9	1.1 ± 0.3	–97.5 ± 2.3	–51.3 ± 2.2	20.466	11	1.861	8	37L
WISE 1141–3326	175.485224	7.6	–33.443233	8.1	99.7 ± 4.2	1.8 ± 0.8	–904.4 ± 2.3	–76.5 ± 2.5	11.648	11	1.059	8	15H
WISE 1143+4431	175.917700	17.6	44.523342	16.6	38.1 ± 6.5	1.9 ± 0.8	76.9 ± 5.1	–71.0 ± 5.0	7.188	9	0.799	7	10L
WISE 1150+6302	177.558621	3.1	63.044318	2.6	124.5 ± 3.0	1.7 ± 0.5	410.4 ± 1.8	–539.7 ± 1.2	34.761	37	0.939	21	8L
ULAS 1152+1134	178.165841	12.5	11.568698	6.8	49.7 ± 5.1	2.1 ± 0.2	–492.4 ± 3.6	–24.0 ± 2.1	17.856	7	2.551	6	5H
WISE 1206+8401	181.512532	2.8	84.019282	2.4	81.9 ± 2.5	1.3 ± 0.3	–575.0 ± 1.3	–255.7 ± 1.1	44.711	35	1.277	20	19L
WISE 1217+1626AB	184.487872	5.0	16.443394	4.7	104.4 ± 4.7	1.7 ± 0.3	758.1 ± 1.7	–1252.2 ± 1.5	75.092	13	5.776	9	8L
WISE 1220+5407	185.151875	16.9	54.121108	24.9	42.7 ± 7.1	1.6 ± 0.3	192.2 ± 5.6	–310.7 ± 7.8	17.816	9	1.980	7	13L
WISE 1221–3136	185.468474	3.6	–31.599861	2.9	73.8 ± 3.3	1.9 ± 0.6	611.0 ± 1.9	396.7 ± 2.3	17.685	31	0.570	18	6H
WISE 1225–1013	186.495136	2.9	–10.229558	2.9	43.3 ± 3.0	2.1 ± 1.0	–156.6 ± 1.8	–325.5 ± 1.5	47.409	31	1.529	18	10H
2MASS 1231+0847	187.943521	10.3	8.788496	11.7	75.8 ± 4.8	1.7 ± 0.5	–1173.4 ± 3.1	–1034.1 ± 3.5	3.567	11	0.324	8	9L
WISE 1243+8445	190.783116	9.1	84.762718	8.8	48.6 ± 4.5	1.8 ± 0.4	–530.2 ± 2.8	–524.1 ± 2.7	11.855	9	1.317	7	11H
WISE 1254–0728	193.702040	12.0	–7.474752	7.8	47.2 ± 4.4	1.7 ± 1.0	9.0 ± 3.6	–131.3 ± 2.4	13.651	13	1.050	9	15L
WISE 1257+4008	194.316587	19.7	40.148440	15.3	45.7 ± 8.2	1.8 ± 0.8	320.0 ± 5.7	176.5 ± 4.5	7.465	9	0.829	7	10L
VHS 1258–4412	194.520589	6.7	–44.209184	6.7	63.8 ± 4.0	1.3 ± 0.3	143.6 ± 2.3	–150.7 ± 2.2	12.625	9	1.403	7	22H
WISE 1301–0302	195.423510	9.0	–3.037151	7.3	53.8 ± 5.6	1.5 ± 0.4	241.5 ± 2.9	–295.5 ± 2.2	16.300	13	1.254	9	18L
WISE 1318–1758	199.641069	2.6	–17.974000	2.5	57.8 ± 2.7	1.5 ± 0.4	–515.2 ± 1.6	6.8 ± 1.4	61.843	35	1.767	20	11H
WISE 1333–1607	203.249743	8.0	–16.131943	6.0	48.0 ± 4.7	1.4 ± 1.0	–315.3 ± 2.5	–125.7 ± 1.9	11.932	7	1.705	6	14L
WISE 1405+5534	211.322470	3.2	55.572792	2.7	157.9 ± 3.1	2.0 ± 1.1	–2326.5 ± 1.7	236.1 ± 1.3	19.758	33	0.599	19	10H
VHS 1433–0837	218.297357	7.0	–8.626956	4.8	50.9 ± 4.5	1.7 ± 0.6	–284.4 ± 2.4	–204.6 ± 1.8	13.113	13	1.009	9	10H
WISE 1436–1814	219.009079	2.4	–18.239528	2.4	48.3 ± 2.4	1.2 ± 0.3	–67.3 ± 1.3	–86.3 ± 1.3	40.342	37	1.090	21	14H
WISE 1448–2534	222.027086	2.6	–25.573128	2.6	52.5 ± 2.5	1.1 ± 0.3	142.5 ± 1.4	–741.6 ± 1.4	45.332	33	1.374	19	27H
WISE 1501–4004	225.317046	6.8	–40.072132	6.6	69.5 ± 4.0	1.0 ± 0.1	370.2 ± 2.3	–337.3 ± 2.2	22.436	9	2.493	7	39H

Table 4
(Continued)

Object Name	J2000 R.A. Ep. 2014.0 (deg)	R.A. Unc. (mas)	J2000 Decl. Ep. 2014.0 (deg)	Decl. Unc. (mas)	π_{abs} (mas)	corr $_{\pi}$ (mas)	$\mu_{\text{R.A.}}$ (mas yr $^{-1}$)	$\mu_{\text{Decl.}}$ (mas yr $^{-1}$)	χ^2	Dof	Red. χ^2	# of Ep.	# of Reg. Stars ^a
(1)	(2)	(3)	(4)	(5)	(6)	(7)	(8)	(9)	(10)	(11)	(12)	(13)	(14)
WISE 1517+0529	229.337884	6.8	5.491625	6.5	42.1 ± 4.2	1.1 ± 0.2	-55.5 ± 2.3	194.9 ± 2.2	11.812	9	1.312	7	23L
WISE 1519+7009	229.778548	3.0	70.158202	2.7	77.6 ± 2.8	1.5 ± 0.5	325.0 ± 1.5	-501.4 ± 1.2	28.582	33	0.866	19	10H
WISE 1523+3125	230.771352	4.9	31.426572	4.8	61.4 ± 3.8	1.6 ± 0.7	103.9 ± 1.7	-509.2 ± 1.7	10.595	13	0.815	9	15L
WISE 1541-2250	235.464060	2.4	-22.840555	2.3	167.1 ± 2.3	1.1 ± 0.4	-901.2 ± 1.2	-82.4 ± 1.2	42.714	37	1.154	21	31H
WISE 1542+2230	235.557193	6.5	22.501044	5.3	85.6 ± 4.2	1.2 ± 0.3	-974.3 ± 2.2	-391.9 ± 1.8	28.358	13	2.181	9	11L
WISE 1612-3420	243.066007	3.7	-34.341849	3.6	78.3 ± 3.5	0.7 ± 0.1	-289.4 ± 1.2	-586.6 ± 1.2	12.487	13	0.961	9	62H
WISE 1614+1739	243.673390	3.6	17.659388	3.5	97.6 ± 3.4	1.7 ± 0.5	554.5 ± 1.2	-476.7 ± 1.2	5.324	15	0.355	10	10H
2MASS 1615+1340	243.768480	2.5	13.667415	2.4	58.4 ± 2.5	1.3 ± 0.5	291.1 ± 1.4	-325.5 ± 1.3	30.952	35	0.884	20	18H
WISE 1622-0959	245.537284	3.9	-9.992961	3.4	40.2 ± 3.5	1.0 ± 0.2	44.2 ± 1.4	-7.3 ± 1.2	26.773	15	1.785	10	15H
WISE 1639-6847	249.921745	3.0	-68.797280	3.0	211.9 ± 2.7	1.0 ± 0.2	582.0 ± 1.5	-3099.8 ± 1.5	17.158	31	0.553	18	71H
WISE 1653+4444	253.295797	4.1	44.739248	3.9	78.0 ± 4.2	1.4 ± 0.5	-70.7 ± 2.9	-387.3 ± 2.2	12.774	31	0.412	18	13L
WISE 1711+3500AB	257.768950	2.2	35.010157	2.5	40.3 ± 2.4	1.4 ± 0.5	-156.3 ± 1.1	-71.2 ± 1.2	116.848	37	3.158	21	15H
WISE 1717+6128	259.320846	4.5	61.483138	4.0	48.0 ± 3.8	1.6 ± 0.6	81.7 ± 1.4	-30.5 ± 1.3	15.543	13	1.196	9	9H
WISE 1721+1117	260.393469	6.9	11.294412	9.0	42.0 ± 4.0	1.0 ± 0.2	-89.2 ± 2.2	144.5 ± 2.9	5.929	9	0.659	7	22H
WISE 1735-8209	263.963188	6.0	-82.150405	6.2	75.1 ± 4.6	1.3 ± 0.3	-250.2 ± 1.9	-257.8 ± 1.8	16.760	9	1.862	7	11H
WISE 1738+2732	264.648439	2.4	27.549315	2.3	131.0 ± 2.4	1.2 ± 0.4	337.3 ± 1.1	-338.1 ± 1.1	34.296	39	0.879	22	19H
WISE 1804+3117	271.147014	3.4	31.285122	3.5	62.7 ± 3.4	1.5 ± 0.5	-251.7 ± 1.1	7.0 ± 1.1	20.461	15	1.364	10	22H
WISE 1812+2007	273.179657	3.8	20.128953	4.5	47.8 ± 4.0	0.9 ± 0.1	0.7 ± 0.6	-534.4 ± 1.5	17.409	11	1.583	8	34H
WISE 1813+2835	273.372052	2.6	28.591745	2.6	74.9 ± 2.5	1.0 ± 0.2	-204.7 ± 1.3	-462.4 ± 1.3	22.237	33	0.674	19	31H
WISE 1828+2650	277.130718	2.2	26.844010	2.2	100.7 ± 2.3	1.0 ± 0.2	1017.5 ± 1.0	174.5 ± 1.0	32.475	39	0.833	22	38H
WISE 1928+2356	292.171905	2.5	23.934871	2.6	149.9 ± 2.4	0.4 ± 0.1	-241.5 ± 1.3	243.1 ± 1.3	77.458	33	2.347	19	374H
WISE 1955-2540	298.752056	2.5	-25.670762	2.5	36.6 ± 2.4	1.1 ± 0.3	349.8 ± 1.2	-248.3 ± 1.2	49.674	31	1.602	18	43H
WISE 1959-3338	299.773590	2.2	-33.642914	2.2	85.3 ± 2.2	1.1 ± 0.3	-8.6 ± 1.0	-193.2 ± 1.1	29.136	39	0.747	22	28H
WISE 2000+3629	300.209091	2.6	36.497627	2.7	133.1 ± 2.5	1.2 ± 0.3	9.4 ± 1.3	377.9 ± 1.2	16.485	35	0.471	20	343H
WISE 2005+5424	301.333016	3.7	54.408501	3.7	62.9 ± 3.3	1.1 ± 0.2	-1154.4 ± 1.2	-900.4 ± 1.2	16.282	15	1.085	10	41H
WISE 2015+6646	303.942603	2.7	66.779477	2.8	43.1 ± 2.7	1.3 ± 0.5	290.0 ± 1.3	428.3 ± 1.6	35.701	29	1.231	17	17H
WISE 2017-3421	304.453417	6.2	-34.350581	8.3	46.9 ± 4.1	1.2 ± 0.3	192.1 ± 1.9	291.8 ± 2.6	7.140	9	0.793	7	13H
WISE 2019-1148	304.836805	3.9	-11.802130	3.9	77.5 ± 3.5	1.1 ± 0.3	354.2 ± 1.3	-48.3 ± 1.3	11.785	13	0.907	9	16H
WISE 2056+1459	314.121286	2.2	14.998666	2.2	138.3 ± 2.2	1.1 ± 0.4	823.2 ± 1.0	534.1 ± 1.0	40.728	39	1.044	22	52H
WISE 2147-1029	326.778366	4.8	-10.490200	6.8	42.8 ± 4.0	1.3 ± 0.5	89.0 ± 1.5	-135.0 ± 2.0	25.841	11	2.349	8	22L
WISE 2157+2659	329.464040	2.2	26.991920	2.2	59.7 ± 2.2	1.2 ± 0.4	69.6 ± 1.1	-92.2 ± 1.1	32.509	39	0.834	22	31H
WISE 2159-4808	329.956825	2.7	-48.149927	2.5	75.7 ± 2.7	1.2 ± 0.4	316.6 ± 1.4	-1229.8 ± 1.3	36.665	37	0.991	21	22L
WISE 2203+4619	330.769173	12.8	46.322939	13.1	66.0 ± 4.2	0.4 ± 0.1	1284.9 ± 4.4	-270.3 ± 4.3	16.600	11	1.509	8	79H
WISE 2209-2734	332.341272	3.6	-27.578140	5.2	78.2 ± 3.9	2.1 ± 1.2	-781.0 ± 2.4	-430.9 ± 1.9	18.028	37	0.487	21	5L
WISE 2209+2711	332.275276	2.3	27.194171	2.3	161.6 ± 2.4	1.4 ± 0.5	1204.4 ± 1.1	-1357.5 ± 1.1	38.925	37	1.052	21	17H
WISE 2211-4758	332.918711	9.1	-47.974160	8.7	55.8 ± 4.6	1.6 ± 0.3	-117.6 ± 2.8	-50.4 ± 2.6	5.445	9	0.605	7	10H
WISE 2212-6931	333.070499	2.4	-69.522650	2.5	81.9 ± 2.5	1.1 ± 0.4	784.4 ± 1.2	-54.6 ± 1.2	84.780	35	2.422	20	39L
WISE 2220-3628	335.230876	2.4	-36.471641	2.5	97.0 ± 2.4	2.0 ± 0.6	286.8 ± 1.2	-81.4 ± 1.2	47.403	35	1.354	20	14H
WISE 2232-5730	338.019424	6.6	-57.503027	6.5	49.9 ± 4.4	1.3 ± 0.5	405.5 ± 2.0	-102.6 ± 1.9	12.625	11	1.148	8	15L
WISE 2237+7228	339.334691	2.6	72.476000	2.5	62.3 ± 2.5	1.0 ± 0.2	-80.2 ± 1.3	-97.7 ± 1.3	22.397	31	0.722	18	24H
WISE 2255-3118	343.920079	4.7	-31.311886	6.9	70.7 ± 4.2	1.5 ± 0.4	300.2 ± 1.5	-162.1 ± 2.2	16.157	15	1.077	10	11L
WISE 2301+0216	345.388795	3.4	2.276363	3.1	53.0 ± 2.8	1.4 ± 0.3	-82.6 ± 1.6	-88.9 ± 1.6	41.625	29	1.435	17	14L
WISE 2302-7134	345.619196	7.9	-71.578222	6.2	65.1 ± 4.7	1.3 ± 0.6	-106.3 ± 2.4	30.7 ± 2.0	7.049	9	0.783	7	35L
WISE 2313-8037	348.403564	2.8	-80.617175	2.6	93.5 ± 2.7	1.0 ± 0.2	275.1 ± 1.3	-402.2 ± 1.2	23.801	31	0.768	18	35L
WISE 2319-1844	349.913188	3.1	-18.734474	3.1	79.2 ± 3.1	1.5 ± 0.5	65.5 ± 1.6	138.8 ± 1.6	47.327	37	1.279	21	6L

Table 4
(Continued)

Object Name	J2000 R.A. Ep. 2014.0 (deg)	R.A. Unc. (mas)	J2000 Decl. Ep. 2014.0 (deg)	Decl. Unc. (mas)	π_{abs} (mas)	corr_{π} (mas)	$\mu_{\text{R.A.}}$ (mas yr ⁻¹)	$\mu_{\text{Decl.}}$ (mas yr ⁻¹)	χ^2	Dof	Red. χ^2	# of Ep.	# of Reg. Stars ^a
(1)	(2)	(3)	(4)	(5)	(6)	(7)	(8)	(9)	(10)	(11)	(12)	(13)	(14)
ULAS 2321+1354	350.349333	2.4	13.914238	2.7	83.6 ± 2.4	1.6 ± 0.5	78.7 ± 1.2	-561.6 ± 1.4	25.489	39	0.654	22	12H
ULAS 2326+0201	351.502016	7.1	2.027545	7.8	49.5 ± 4.6	1.5 ± 0.6	299.8 ± 2.2	80.4 ± 2.4	13.197	9	1.466	7	22L
WISE 2332-4325	353.110751	2.4	-43.419959	2.7	65.3 ± 2.6	2.0 ± 0.6	249.7 ± 1.2	-249.9 ± 1.5	46.217	37	1.249	21	10H
WISE 2343-7418	355.965092	2.8	-74.312845	2.4	58.8 ± 2.7	1.7 ± 0.6	380.9 ± 1.4	192.5 ± 1.2	20.757	33	0.629	19	13H
WISE 2344+1034	356.193582	4.1	10.570956	3.9	64.7 ± 3.7	1.6 ± 0.6	942.1 ± 1.4	-23.9 ± 1.3	41.041	13	3.157	9	18L
WISE 2354+0240	358.512041	8.4	2.670263	8.8	124.1 ± 4.9	1.9 ± 0.9	491.1 ± 2.8	-393.1 ± 3.0	14.458	9	1.606	7	16L
WISE 2357+1227	359.318798	7.6	12.460976	9.9	59.5 ± 4.1	1.5 ± 0.4	24.0 ± 2.6	-500.5 ± 3.2	11.415	9	1.268	7	19L

Note.

^a The letter following the number of re-registration stars indicates whether we used the high-S/N (“H”) or low-S/N (“L”) limit for their selection. See Section 5.2.2 for details.

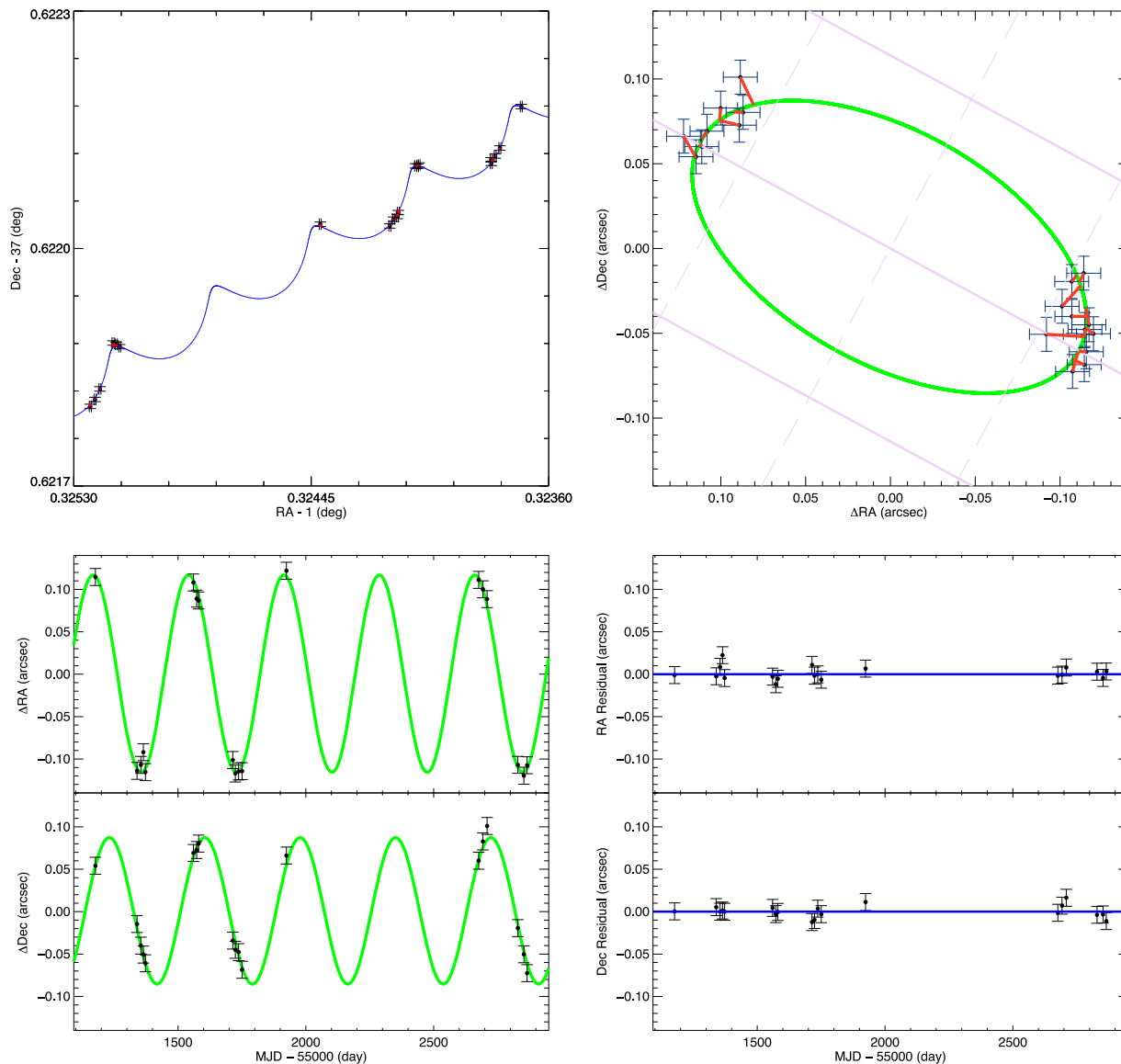
WISE J000517.48+373720.5 ($\beta = 33.56^\circ$)

Figure 2. Plots of our astrometric measurements and their best fits, divided into four panels. (Upper left) The measured astrometry and its uncertainty at each epoch (black points with error bars) plotted in R.A. and decl. with the best-fit model shown as the blue curve. Red lines connect each observation to its corresponding time point along the best-fit curve. (Upper right) A square patch of sky centered at the mean equatorial position of the target. The green curve is the parallax fit, which is just the blue curve in the previous panel with the proper motion vector removed. In the background is the ecliptic coordinate grid, with lines of constant β shown in solid pale purple and lines of constant λ shown in dashed pale purple. Grid lines are shown at $0''.1$ spacing. (Lower left) The change in R.A. and decl. as a function of time with the proper motion component removed. The parallax fit is again shown in green. (Lower right) The overall R.A. and decl. residuals between the observations and the best-fit model as a function of time. The complete figure set contains these same plots for all 142 objects in the *Spitzer* parallax program.

(The complete figure set (142 images) is available.)

The fiducial time was chosen to be at a point in the middle of our observational data set, epoch 2014.0, since setting this to be within the timeframe of the observations minimizes the associated uncertainties. Choosing a much later or earlier time, say 2000.0, would result in larger positional uncertainties since the uncertainty from the proper motion compounds with the difference in the time interval between the observations and the chosen fiducial time.

Table 4 gives the best-fitting solutions for each of our 142 targets. The abbreviated object name is in column 1 followed by the position of the object at epoch 2014.0 along with the positional uncertainties in column 2–5. The value of parallax

obtained by the best-fit solution above is a measurement relative to the background stars and requires an adjustment to the absolute reference frame as described further below. The resulting value of the absolute parallax and the correction needed to convert from relative to absolute units are given in columns 6 and 7. The best-fit proper motion per axis and its uncertainties are listed in columns 8 and 9. The χ^2 value of the best fit, the number of degrees of freedom, and the reduced χ^2 value are listed in columns 10–12. The number of *Spitzer* epochs used in the solution is shown in column 13. Finally, the number of re-registration stars used along with a flag value for the S/N floor used for registration star selection (“H” for the

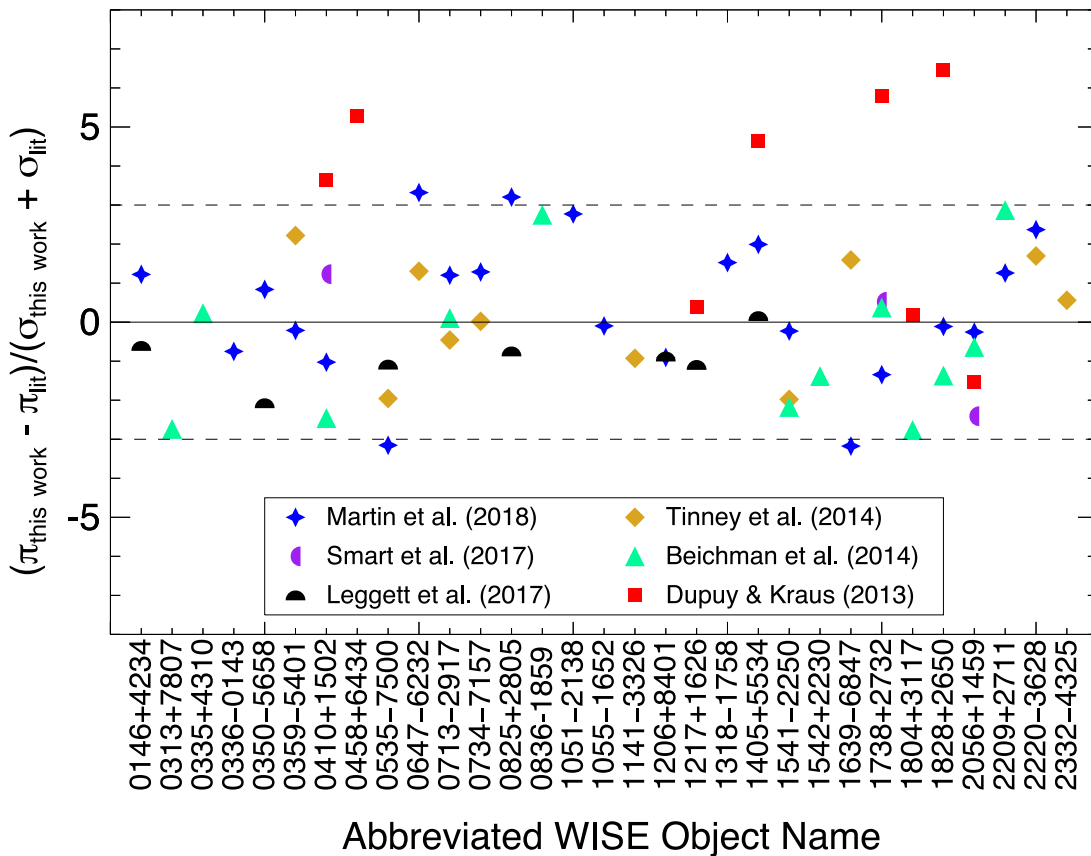


Figure 3. Comparison of the parallax determinations for 31 objects in common between this paper and those of other published works. Our results show excellent agreement with other values, with the exception of measurements from Dupuy & Kraus (2013). See text for discussion.

high S/N cut and “L” for the low S/N cut) is given in column 14.

We are measuring parallaxes relative to re-registration stars in each field, so we need to account for the fact that those re-registration stars themselves each have a small parallax that is partially damping the parallactic signal of our target. In order to correct for this, we need estimates of the mean distance to the re-registration stars. To do this, we tabulated the stars’ J -band magnitudes measured from the 2MASS All-Sky Point Source Catalog, supplemented in some cases by the 2MASS Survey Point Source Reject Table. The distance to each object is then estimated by comparing that magnitude to a model prediction of Galactic structure for that region of sky, as provided by Mendez & van Altena (1996). For fields where 2MASS J magnitudes were available for all re-registration stars, we found that the correction was very small and varied from 0.4 to 2.2 mas. For some fields, not all of our re-registration stars were detected by 2MASS, so these stars were assigned a floor value for $J = 17.0$. To test whether this is a reasonable assumption, we chose WISE 0032–4946 because 5 of its 13 re-registration stars have no 2MASS mags. Setting all five of these to have $J = 17.0$ mag gives a correction of 1.4 ± 0.3 mas. If we instead set all five to an absurdly faint value of $J = 19.0$ mag, we find a correction of 1.1 ± 0.6 mas. Because these two assumptions give corrections that are essentially identical within the error bars and the former is likely more realistic, we assumed a floor of $J = 17.0$ mag (or $J = 16.5$ mag in fields of higher source density) for all 2MASS undetected sources. Plots of our astrometric measurements and their best fits are shown in Figure 2.

We note from Table 4 that most of our objects have values of reduced χ^2 near 1.0, confirming that our methodology for measuring the astrometric uncertainties per epoch is sound. This enables us to identify targets for which either our centroiding is poor because a marginally resolved companion creates a profile not well fit by our PRF, or our single-object solution is a poor assumption due to the presence of an unseen companion. Objects with fits having reduced χ^2 values >2 have been placed on continued monitoring with *Spitzer* through the end of Cycle 14 to see if any cyclical variations in the residuals, indicative of an unseen astrometric companion, can be found. These and other targets of interest are discussed in Section 8.2.

By design, most of the T dwarfs in our parallax program were selected for observation because they were not being targeted by other ground- or space-based programs. On the other hand, *all* known Y dwarfs were targeted regardless of whether they had parallaxes measured elsewhere. As a result, only 31 of the 142 objects for which we have *Spitzer*-measured parallaxes have previously measured values. Figure 3 compares our values to those in the literature for these 31 objects. Three comparison data points fall outside of the boundaries of this plot, but those are attributed to poor measurements in the literature: WISE 0146+4234 and WISE 2220–3628 from Beichman et al. (2014), which are discrepant from our values by $\sim 9\sigma$, and WISE 1541–2250 from Dupuy & Kraus (2013), which is discrepant from our value by $\sim 20\sigma$. These literature values are also discrepant with other published values; see the analyses of WISE 2220–3628 in Martin et al. (2018), WISE

1541–2250 in Martin et al. (2018) and Bedin & Fontanive (2018), and WISE 0146+4234 in Leggett et al. (2017).

We find excellent agreement between our values and ground-based Magellan/FourStar measurements by Tinney et al. (2014), between our values and ground-based United Kingdom Infrared Telescope (UKIRT)/WFCAM measurements by Smart et al. (2017), and between our values and *Spitzer*/IRAC ch2 measurements by Leggett et al. (2017), some data for which had been published earlier in Luhman & Esplin (2016) and which uses a subset of the *Spitzer*/IRAC ch2 imaging taken by us. With the exception of the two objects noted above, we also find excellent agreement with a hybrid approach from Beichman et al. (2014) that uses astrometry compiled from Keck/NIRC2, *Hubble Space Telescope* (HST)/WFC3, *WISE*, and *Spitzer*/IRAC.

We can also compare the parallax measurements for objects in common between this paper and Martin et al. (2018). The latter paper uses a subset of the same *Spitzer*/IRAC ch2 data used in the current paper, but there are a few differences to note: (1) the current paper uses measurements taken from individual frames as opposed to the Martin et al. (2018) method of using measurements from the epochal coadds, (2) the current paper uses a different set of analysis code following the MOPEX frame extraction step, even though the guiding logic is very similar, and (3) the current paper benefits from the longer time baseline afforded by the additional observations in Cycle 13. Of the 22 objects in common between the two papers, 4 have differences exceeding three times the sum of the individual uncertainties. Two of these objects, WISE 0535–7500 and WISE 0647–6323, are located near the Continuous Viewing Zone of *Spitzer* and thus have frames taken at many different roll angles, where the aforementioned issue with the MOPEX mosaicking step (Section 5.2.1) is known to have problems. A comparison of the parallax-only plots for these two objects (Figure 2, upper right panels) show individual measurements with much smaller uncertainties and a more convincing overall fit than do similar plots in Martin et al. (2018, their Figure 5). For the other two objects—WISE 0825+2805 and WISE 1639–6847—the improved astrometry provided by individual frame measurements along with the added time baseline (an additional three years) appears to have vastly improved the fits and as a consequence moved them significantly from the parallax values determined by Martin et al. (2018).

Just as both Smart et al. (2017) and Martin et al. (2018) found, we see a systematic offset between our values and the parallaxes measured by Dupuy & Kraus (2013), who used *Spitzer*/IRAC ch1 imaging. Martin et al. (2018) advanced three hypotheses to attempt to explain the discrepancy: (1) chromatic distortion in the ch1 data, (2) a fundamental error in the Dupuy & Kraus (2013) fitting analysis, or (3) an insufficient time baseline with which to beat down random errors and to disentangle proper motion and parallax. Despite testing each of these hypotheses, Martin et al. (2018) were unable to come to a firm conclusion.

6. USNO Astrometry

A number of early *WISE* discoveries from Table 1 were astrometrically monitored at the U.S. Naval Observatory (USNO) in Flagstaff. These objects were measured on the 1.55 m Strand Astrometric Reflector using the ASTROCAM infrared imager (Fischer et al. 2003), which was commissioned

in 2000 September. Sadly, the original ASTROCAM was destroyed in a cryogenic explosion ultimately caused by a local forest fire in 2006 June. In 2011 May, a repaired version of ASTROCAM was commissioned, using the same basic setup as the old instrument. Observation and reduction procedures for these new targets are nearly identical to those described in Vrba et al. (2004), which presented preliminary parallaxes and proper motions of 40 L and T dwarfs using the first 1.7 years of data from the original instrument. The main difference is that these new reductions use a combined X+Y solution, rather than just using the X solution as was done in Vrba et al. (2004), along with minor quality control software improvements to ensure that all useful frames are included in the solutions. Final parallax and proper motion results for the original 40 objects plus an additional 19 L and T dwarfs using the full, original ASTROCAM database will be given in F. J. Vrba et al. (in preparation).

The eighteen objects in Table 5 were placed on the program over a number of years after recommissioning and the results shown are for data obtained through early fall of 2017. All of these objects and an additional 103 sources continue on the USNO ASTROCAM astrometry program. All results in Table 5 were obtained through a *J*-band filter. The abbreviated object name is given in column 1, the relative parallax and its uncertainty in column 2, the proper motion along with its uncertainty and position angle (east of north) in columns 3 and 4, the total time baseline of the observations in column 5, the number of independent nights of observation in column 6, and the number of registration stars in column 7. While several factors contribute to the quality of in-frame relative astrometry (e.g., the distribution of registration stars), objects having smaller measurement errors are generally those that have been observed over a longer time baseline. As a case in point, WISE 2226+0440 has the poorest measurements because it was added much later into the program. (In fact, it is the only object in Table 5 not already listed in Table 3 of Vrba et al. 2015.) Given the typical magnitudes of the registration stars, the correction from relative to absolute parallax is $\sim 1.6 \pm 0.3$ mas (Vrba et al. 2004). For subsequent analyses we have added this correction, and its uncertainty in quadrature, to the relative parallax to convert to near-absolute units.

7. New Technology Telescope (NTT) and UKIRT Astrometry

Twenty-three additional late-T dwarfs were monitored astrometrically at either the 3.5 m NTT or the 3.8 m UKIRT; one of these objects was observed at both facilities. Table 6 lists the results. An abbreviated name of the object from Table 1 is given in column 1, and the source of the measurement as either NTT or UKIRT is given in column 2. The J2000 equinox R.A. and decl. along with the epoch of the position are given in columns 3–5. The measured values of the absolute parallax and the correction from relative parallax are given in columns 6–7, and the measured proper motions per axis are given in columns 8–9. Columns 10–12 list the total time baseline, the number of registration stars, and the total number of observations.

Fourteen objects were targeted as part of the NTT Parallaxes of Southern Extremely Cool objects (NPARSEC) project. NPARSEC is a European Southern Observatory long-term program (186.C-0756; R. Smart, PI) of 96 nights on the NTT's infrared spectrograph and imaging camera Son Of ISAAC

Table 5
Parallax and Motion Fits for Objects on the USNO Parallax Program

Object Name	π_{rel} (mas)	μ_{rel} (mas yr ⁻¹)	θ (deg)	Baseline (yr)	# of Ep.	# of Reg. Stars
(1)	(2)	(3)	(4)	(5)	(6)	(7)
WISE 0254+0223	144.49 ± 1.45	2572.2 ± 0.1	85.05 ± 0.03	5.30	107	13
WISE 0513+0608	69.17 ± 1.49	433.0 ± 1.0	180.69 ± 0.07	5.41	133	16
WISE 0614+3912	52.09 ± 1.70	529.3 ± 1.2	200.55 ± 0.07	5.30	71	20
WISE 0625+5646	47.94 ± 2.02	52.7 ± 1.4	251.86 ± 0.76	5.24	74	15
WISE 1019+6529	41.25 ± 1.75	150.6 ± 1.1	323.89 ± 0.21	5.92	93	7
WISE 1122+2550	64.74 ± 2.26	1028.6 ± 1.2	252.34 ± 0.04	5.98	88	8
WISE 1320+6034	59.00 ± 2.54	561.3 ± 1.4	264.80 ± 0.08	6.05	50	10
WISE 1322-2340	75.86 ± 4.22	524.1 ± 1.9	318.35 ± 0.11	5.92	56	9
WISE 1457+5815	53.43 ± 2.30	502.0 ± 1.1	262.75 ± 0.07	6.08	107	12
WISE 1506+7027	191.91 ± 0.51	1587.3 ± 0.3	311.19 ± 0.03	6.08	100	9
WISE 1627+3255	52.77 ± 1.85	351.6 ± 0.8	193.55 ± 0.07	6.10	66	11
WISE 1741+2553	212.65 ± 2.77	1556.9 ± 1.3	198.94 ± 0.04	5.10	56	14
WISE 1852+3537	70.41 ± 1.88	381.5 ± 1.1	138.82 ± 0.09	5.29	63	15
WISE 1906+4508	62.45 ± 1.60	351.0 ± 0.1	183.73 ± 0.08	5.35	53	16
WISE 2213+0911	52.88 ± 2.45	128.0 ± 1.2	256.46 ± 0.27	5.37	133	9
WISE 2226+0440	52.75 ± 5.87	543.2 ± 5.7	211.42 ± 0.30	2.23	38	9
WISE 2340-0745	46.19 ± 3.11	293.1 ± 1.4	148.58 ± 0.14	5.32	61	9
WISE 2348-1028	56.77 ± 3.46	642.5 ± 1.5	75.96 ± 0.08	5.24	62	7

(SOFI; Moorwood et al. 1998). The main observational program ran from 2010 October 1 through 2013 September 15, although various ad hoc requests were made to extend the temporal baseline through 2018. Target selection, observing methodology, and reduction procedures are explained in detail in Smart et al. (2013).

Ten objects were targeted as part of a UKIRT program primarily designed to follow-up T dwarfs from the UKIRT Infrared Deep Sky Survey (UKIDSS; Lawrence et al. 2007). This program, described in Marocco et al. (2010), used service observations on the UKIRT Wide Field Camera (WFCAM; Casali et al. 2007), which is a large-field infrared imager. This program started as a director’s discretionary request in 2007 and continued under various proposals and target lists until 2016. As the UKIDSS discovery image was often used in the parallax determination, some targets also have observations starting as early as 2005. Scheduling, observing methodology, and reduction procedures are described in Smart et al. (2010) and Marocco et al. (2010).

The results in Table 6 are regarded as preliminary only. Final reductions on both data sets will be completed in the near future, once observations from the NTT program conclude.

8. Analysis of the Mean Trends

In the following subsections, we amass the color, parallax, and proper motion data from Tables 1, 2, and 4–6 to study trends in spectral type, absolute magnitude, color, and tangential velocity for late-T to early-Y dwarfs. We also discuss objects that may be particularly interesting because of their unusual placement relative to the means trends or their high reduced χ^2 values in the *Spitzer* parallax and proper motion fits.

Table 7 summarizes the adopted spectral types (column 2), the measured parallaxes and proper motions (columns 4 and 6), and the derived absolute magnitudes (columns 8–13) and tangential velocities (column 14) for all of the T6 and later objects for which we have newly measured parallaxes or for

which quality parallaxes have been published by other groups. Full designations for the abbreviated names listed in column 1 can be found in Table 1, and the spectral code in column 3 gives a conversion from the spectral type to a scale running from 6 at T6.0 to 14 at Y4. Objects lacking spectral types are not shown on subsequent plots having spectral type along one axis, with the exception of WD 0806B and WISE 0855–0714, whose types are assumed to be Y1 and \geq Y4 (see footnotes to Table 1).

Column 5 indicates whether the parallax value in column 4 is an absolute or a relative value. The only references with relative parallaxes are the USNO results from Table 5 and those from Tinney et al. (2003, 2014). As stated in Section 6, the correction from relative to absolute parallax is expected to be $\sim 1.6 \pm 0.3$ mas for the USNO results. The near-infrared results from Tinney et al. (2003) were done on a telescope of larger aperture (3.5 m NTT) than that of the USNO program (1.55 m Strand), so smaller corrections can be assumed based on the fact that stars in the reference frames are generally fainter and more distant. The corrections shown in Table 6 from both the 3.5 m NTT and 3.8 m UKIRT indicate that a correction of $\sim 0.9 \pm 0.3$ mas is also appropriate here. The near-infrared results from Tinney et al. (2014) were obtained on the larger aperture Magellan Baade Telescope (6.5 m), so even smaller corrections of $\sim 0.6 \pm 0.3$ mas can be assumed. These mean relative-to-absolute parallax corrections have been applied to all parallaxes for these three sources prior to the calculation of the absolute magnitudes and tangential velocities in Table 7. These corrections have also been applied in the analyses of subsequent sections of this paper.

For the *J*, *H*, *K* photometry, we list only *H*-band because it is the only one of these three bands that is invariant between the two main near-infrared classification systems, 2MASS and MKO-NIR (see Section 4.3 of Kirkpatrick et al. 2012). Photometry shortward of *J*-band is scarce due to a combination of non-universal filters (such as *z* and *Y*) and the fact that these brown dwarfs are much fainter, and thus harder to detect, at even shorter wavelengths (e.g., at *R* or *I*). Longward of *K*-band,

Table 6
Parallax and Motion Fits for Objects on the NTT and UKIRT Parallax Programs

Object Name (1)	Program (2)	J2000 R.A. (deg) (3)	J2000 Decl. (deg) (4)	Epoch (5)	π_{abs} (mas) (6)	Abs. Corr. (mas) (7)	$\mu_{\text{R.A.}}$ (mas yr ⁻¹) (8)	$\mu_{\text{Decl.}}$ (mas yr ⁻¹) (9)	Baseline (yr) (10)	# of Ref. Stars (11)	# of Obs. (12)
WISE 0040+0900	UKIRT	10.103778	9.0151823	2010.50	69.8 ± 1.5	1.0	-52.3 ± 0.9	-53.0 ± 2.0	6.0	117	11
ULAS 0150+1359	UKIRT	27.601590	13.990027	2011.01	39.8 ± 3.2	1.1	25.0 ± 1.9	24.8 ± 1.4	7.4	177	31
WISE 0223-2932	NPARSEC	35.844782	-29.550163	2016.79	80.7 ± 2.6	0.6	780.2 ± 1.1	-535.1 ± 1.5	5.8	50	13
2MASS 0348-6022	NPARSEC	57.030457	-60.376464	2010.75	120.1 ± 1.8	0.6	-279.7 ± 0.6	-768.5 ± 0.7	6.4	87	16
UGPS 0521+3640	UKIRT	80.364579	36.678113	2012.65	122.2 ± 1.6	0.3	569.0 ± 0.9	-1511.0 ± 1.0	8.3	311	27
WISE 0528-3308	NPARSEC	82.185418	-33.140095	2011.93	49.4 ± 3.9	0.7	1.0 ± 1.2	-19.5 ± 1.6	6.2	71	16
WISE 0542-1628	NPARSEC	85.629964	-16.474330	2015.89	61.5 ± 2.7	0.7	-217.7 ± 0.9	294.6 ± 0.9	6.2	131	23
WISE 0612-3036AB	NPARSEC	93.057745	-30.603509	2011.12	41.1 ± 1.6	0.6	-120.3 ± 0.7	-258.5 ± 1.7	6.2	274	18
WISE 0623-0456	NPARSEC	95.790440	-4.9403225	2012.98	87.4 ± 2.9	0.6	-905.2 ± 1.1	159.9 ± 0.8	6.2	483	19
WISE 0627-1114	NPARSEC	96.837083	-11.242068	2015.92	74.8 ± 3.6	0.4	-13.2 ± 1.2	-337.8 ± 1.1	6.2	361	23
WISE 0750+2725	UKIRT	117.51434	27.428690	2014.88	68.4 ± 3.4	0.8	-755.7 ± 2.0	-205.6 ± 1.8	4.5	322	18
WISE 0751-7634	NPARSEC	117.78645	-76.580638	2013.23	97.9 ± 6.7	0.6	-104.8 ± 2.8	-189.7 ± 4.5	5.3	187	18
ULAS 0859+1010	UKIRT	134.79402	10.170582	2012.27	50.3 ± 1.7	1.2	-359.6 ± 1.1	-615.3 ± 1.1	6.3	93	44
WISE 0929+0409	UKIRT	142.27811	4.1660936	2009.92	41.0 ± 2.2	0.9	513.8 ± 1.0	-468.4 ± 3.4	6.3	219	12
ULAS 0950+0117	NPARSEC	147.69721	1.2925019	2013.15	57.9 ± 2.3	0.7	241.6 ± 0.7	-360.7 ± 1.1	6.2	40	24
ULAS 0950+0117	UKIRT	147.69729	1.292456	2011.87	55.4 ± 3.2	0.9	234.3 ± 1.9	-358.5 ± 2.1	5.9	203	41
ULAS 1029+0935	UKIRT	157.41857	9.5873423	2012.98	66.8 ± 4.2	1.0	-414.5 ± 1.9	-138.2 ± 2.6	6.3	115	14
ULAS 1238+0935	UKIRT	189.61832	9.8977247	2011.04	44.1 ± 6.1	0.8	-445.8 ± 2.7	48.4 ± 2.9	9.0	223	30
WISE 1311+0122	NPARSEC	197.77626	1.3810927	2013.23	68.8 ± 2.7	0.3	277.9 ± 0.9	-813.9 ± 0.9	5.1	99	18
ULAS 1315+0826	UKIRT	198.78501	8.4407566	2011.01	50.5 ± 5.7	0.9	-61.4 ± 2.1	-101.8 ± 2.5	9.7	240	27
WISE 1617+1807	NPARSEC	244.27404	18.120548	2012.66	84.6 ± 4.2	0.6	92.6 ± 2.1	-40.0 ± 2.1	5.7	48	17
WISE 1812+2721	NPARSEC	273.04510	27.362316	2012.66	98.5 ± 4.4	0.5	140.3 ± 4.1	-322.2 ± 7.8	2.1	256	13
WISE 2018-7423	NPARSEC	304.60471	-74.391622	2012.64	83.2 ± 1.9	0.5	307.7 ± 1.0	-1008.4 ± 1.6	5.9	99	19
ULAS 2342+0856	NPARSEC	355.62098	8.9388664	2012.66	39.9 ± 2.8	0.5	260.1 ± 1.7	-54.8 ± 1.3	3.0	46	19

Table 7
Summary of Spectral Types, Parallaxes, Proper Motions, Absolute Magnitudes, and Tangential Velocities

Object Name (1)	Spec. Type (2)	Spec. Code (3)	π_{abs} (mas) (4)	μ_{total} (mas yr ⁻¹) (5)	π, μ_{total} Reference (6)	M_H (mag) (7)	M_{W1} (mag) (8)	M_{W2} (mag) (9)	M_{W3} (mag) (10)	M_{ch1} (mag) (11)	M_{ch2} (mag) (12)	v_{tan} (km s ⁻¹) (13)
WISE 0005+3737	T9	9	127.0 ± 2.4	1034.0 ± 2.0	Table 4	18.50 ± 0.05	17.28 ± 0.10	13.81 ± 0.05	12.30 ± 0.24	15.95 ± 0.05	13.80 ± 0.04	38.6 ± 0.7
WISE 0015–4615	T8	8	71.8 ± 2.7	796.4 ± 2.0	Table 4	17.19 ± 0.11	16.24 ± 0.13	13.50 ± 0.09	...	15.38 ± 0.09	13.51 ± 0.08	52.6 ± 2.0
WISE 0032–4946	T8.5	8.5	63.6 ± 2.9	938.2 ± 2.4	Table 4	17.89 ± 0.17	16.69 ± 0.19	14.09 ± 0.12	11.22 ± 0.36	15.95 ± 0.11	13.95 ± 0.10	69.9 ± 3.2
ULAS 0034–0052	T8.5	8.5	68.7 ± 1.4	359.2 ± 0.8	1	17.67 ± 0.06	16.19 ± 0.14	13.73 ± 0.08	...	15.42 ± 0.06	13.68 ± 0.05	24.8 ± 0.5
2MASS 0034+0523	T6.5	6.5	120.1 ± 3.0	697.5 ± 2.5	Table 4	15.95 ± 0.06	15.49 ± 0.07	12.95 ± 0.06	12.18 ± 0.32	14.49 ± 0.06	12.98 ± 0.06	27.5 ± 0.7
WISE 0038+2758	T9	9	89.7 ± 2.5	97.5 ± 2.2	Table 4	18.68 ± 0.07	17.21 ± 0.16	14.13 ± 0.07	12.14 ± 0.34	16.22 ± 0.07	14.17 ± 0.06	5.2 ± 0.2
GI 27B	T8	8	89.8 ± 0.1	591.9 ± 0.1	2	16.49 ± 0.03	15.15 ± 0.04	13.39 ± 0.02	31.2 ± 0.1
WISE 0040+0900	T7	7	69.8 ± 1.5	74.5 ± 2.2	Table 6	15.78 ± 0.05	15.20 ± 0.08	13.05 ± 0.07	...	14.29 ± 0.05	12.98 ± 0.05	5.1 ± 0.2
WISE 0049+2151	T8.5	8.5	139.9 ± 2.5	485.4 ± 2.0	Table 4	17.45 ± 0.04	16.65 ± 0.07	13.76 ± 0.05	12.31 ± 0.19	15.74 ± 0.04	13.77 ± 0.04	16.4 ± 0.3
2MASS 0050–3322	T7	7	94.6 ± 2.4	1485.1 ± 2.1	1	15.92 ± 0.11	15.48 ± 0.07	13.46 ± 0.06	11.71 ± 0.25	14.75 ± 0.06	13.47 ± 0.06	74.4 ± 1.9
CFBDS 0059–0114	T8.5	8.5	103.2 ± 2.1	885.8 ± 1.1	1	18.34 ± 0.07	16.97 ± 0.13	13.80 ± 0.06	...	15.84 ± 0.05	13.78 ± 0.05	40.7 ± 0.8
WISE 0123+4142	T7	7	44.0 ± 4.1	608.6 ± 3.2	Table 4	15.42 ± 0.24	15.06 ± 0.22	13.16 ± 0.21	...	14.34 ± 0.20	13.06 ± 0.20	65.6 ± 6.1
CFBDS 0133+0231	T8.5	8.5	56.3 ± 3.4	608.8 ± 2.5	Table 4	17.37 ± 0.16	16.00 ± 0.19	13.73 ± 0.15	...	15.54 ± 0.14	13.81 ± 0.13	51.3 ± 3.1
WISE 0146+4234	Y0	10	52.5 ± 2.3	452.9 ± 1.7	Table 4	21.29 ± 0.17	...	13.68 ± 0.12	...	16.10 ± 0.12	13.67 ± 0.10	40.9 ± 1.8
WISE 0148–7202	T9.5	9.5	91.7 ± 3.4	1269.3 ± 4.1	3	19.02 ± 0.09	18.06 ± 0.22	14.39 ± 0.09	...	16.63 ± 0.09	14.45 ± 0.08	66.0 ± 2.5
ULAS 0150+1359	T7.5	7.5	39.8 ± 3.2	35.2 ± 9.2	Table 6	16.11 ± 0.18	15.50 ± 0.24	13.23 ± 0.20	...	14.45 ± 0.18	13.11 ± 0.18	4.2 ± 1.1
WISE 0221+3842	T6.5	6.5	36.0 ± 4.1	141.3 ± 2.6	Table 4	15.23 ± 0.29	14.51 ± 0.26	12.59 ± 0.25	...	13.71 ± 0.25	12.64 ± 0.25	18.6 ± 2.1
WISE 0223–2932	T7.5	7.5	80.7 ± 2.6	946.1 ± 1.9	Table 6	16.83 ± 0.13	16.40 ± 0.11	13.56 ± 0.08	12.18 ± 0.40	15.34 ± 0.08	13.55 ± 0.07	55.6 ± 1.8
WISE 0226–0211	T7	7	57.3 ± 4.7	527.1 ± 2.7	Table 4	17.67 ± 0.20	16.20 ± 0.22	13.31 ± 0.18	...	15.40 ± 0.18	13.42 ± 0.18	43.6 ± 3.6
WISE 0233+3030	T6	6	31.3 ± 4.2	137.8 ± 3.2	Table 4	14.27 ± 0.29	13.88 ± 0.30	11.82 ± 0.29	...	13.11 ± 0.29	11.83 ± 0.29	20.9 ± 2.8
WISE 0241–3653	T7	7	52.4 ± 2.7	283.8 ± 2.1	Table 4	15.64 ± 0.13	15.46 ± 0.14	12.95 ± 0.12	11.11 ± 0.35	14.34 ± 0.12	12.94 ± 0.11	25.7 ± 1.3
2MASS 0243–2453	T6	6	93.6 ± 3.6	354.8 ± 4.1	4	15.25 ± 0.09	14.51 ± 0.09	12.78 ± 0.09	11.34 ± 0.16	13.81 ± 0.09	12.83 ± 0.09	18.0 ± 0.7
WISE 0247+3725	T8	8	64.8 ± 2.6	87.0 ± 1.8	Table 4	17.30 ± 0.21	17.54 ± 0.44	13.68 ± 0.11	...	15.76 ± 0.10	13.61 ± 0.09	6.4 ± 0.3
WISE 0254+0223	T8	8	146.1 ± 1.5	2572.2 ± 0.1	Table 5	17.11 ± 0.03	16.63 ± 0.05	13.58 ± 0.03	12.18 ± 0.14	15.51 ± 0.03	13.53 ± 0.03	84.4 ± 0.9
WISE 0302–5817	Y0:	10	56.1 ± 4.4	86.8 ± 7.1	Table 4	14.55 ± 0.19	...	16.93 ± 0.19	14.59 ± 0.17	7.3 ± 0.8
WISE 0304–2705	Y0pec	10	81.5 ± 7.7	513.5 ± 9.6	Table 4	20.58 ± 0.26	...	15.15 ± 0.22	...	17.26 ± 0.21	15.05 ± 0.21	29.9 ± 2.8
WISE 0309–5016	[T7]	...	66.8 ± 3.9	559.8 ± 2.3	Table 4	16.55 ± 0.13	15.59 ± 0.14	12.75 ± 0.13	11.88 ± 0.47	14.65 ± 0.13	12.76 ± 0.13	39.7 ± 2.3
WISE 0313+7807	T8.5	8.5	134.3 ± 3.6	89.7 ± 1.7	Table 4	18.27 ± 0.08	16.59 ± 0.07	13.90 ± 0.06	12.69 ± 0.27	15.95 ± 0.06	13.91 ± 0.06	3.2 ± 0.1
WISE 0316+4307	T8	8	73.3 ± 2.8	435.6 ± 2.1	Table 4	19.03 ± 0.12	17.12 ± 0.24	13.97 ± 0.10	...	15.97 ± 0.09	13.91 ± 0.09	28.2 ± 1.1
WISE 0323–5907	[T6]	...	71.5 ± 4.3	720.5 ± 2.6	Table 4	...	16.08 ± 0.15	13.80 ± 0.14	12.16 ± 0.45	15.04 ± 0.13	13.80 ± 0.13	47.8 ± 2.9
WISE 0323–6025	T8.5	8.5	71.4 ± 2.9	535.6 ± 2.0	Table 4	17.67 ± 0.09	16.88 ± 0.15	13.76 ± 0.10	...	15.84 ± 0.10	13.77 ± 0.09	35.6 ± 1.5
WISE 0325–5044	T8	8	36.7 ± 2.7	176.1 ± 2.2	Table 4	17.24 ± 0.16	16.25 ± 0.30	14.03 ± 0.22	...	15.57 ± 0.18	13.52 ± 0.16	22.7 ± 1.7
WISE 0325–3854	T9	9	57.2 ± 5.4	303.2 ± 2.6	Table 4	18.37 ± 0.29	16.58 ± 0.25	13.77 ± 0.21	11.72 ± 0.48	15.91 ± 0.21	13.77 ± 0.21	25.1 ± 2.4
WISE 0325+0831	T7	7	78.5 ± 3.0	122.3 ± 2.5	Table 4	15.62 ± 0.12	14.82 ± 0.09	13.01 ± 0.09	11.36 ± 0.35	14.17 ± 0.09	13.06 ± 0.08	7.4 ± 0.3
WISE 0335+4310	T9	9	72.1 ± 2.4	1140.7 ± 1.7	Table 4	19.23 ± 0.08	...	13.80 ± 0.09	...	15.90 ± 0.08	13.67 ± 0.07	75.0 ± 2.5
WISE 0336–0143	Y0	10	99.0 ± 2.4	1239.4 ± 1.7	Table 4	...	18.43 ± 0.47	14.54 ± 0.08	...	17.23 ± 0.08	14.60 ± 0.06	59.3 ± 1.4
2MASS 0348–6022	T7	7	120.1 ± 1.8	817.8 ± 0.9	Table 6	15.96 ± 0.14	15.42 ± 0.04	12.95 ± 0.04	11.62 ± 0.09	14.56 ± 0.04	12.94 ± 0.04	32.3 ± 0.5
WISE 0350–5658	Y1	11	174.6 ± 2.6	618.2 ± 1.9	Table 4	23.47 ± 0.14	...	15.96 ± 0.05	13.54 ± 0.28	19.15 ± 0.10	15.90 ± 0.04	16.8 ± 0.3
WISE 0359–5401	Y0	10	75.8 ± 2.5	787.9 ± 2.0	Table 4	21.43 ± 0.13	...	14.78 ± 0.09	...	16.95 ± 0.10	14.72 ± 0.08	49.3 ± 1.6
WISE 0404–6420	T9	9	45.7 ± 2.7	68.6 ± 2.3	Table 4	18.27 ± 0.13	16.74 ± 0.22	14.03 ± 0.14	...	15.93 ± 0.15	13.72 ± 0.13	7.1 ± 0.5
WISE 0410+1502	Y0	10	150.2 ± 2.4	2410.2 ± 1.6	Table 4	20.78 ± 0.05	...	15.00 ± 0.06	13.20 ± 0.50	17.52 ± 0.05	15.05 ± 0.04	76.1 ± 1.2
WISE 0413–4750	T9	9	48.2 ± 4.8	321.8 ± 3.5	Table 4	18.62 ± 0.22	17.50 ± 0.41	14.00 ± 0.23	...	16.22 ± 0.23	13.90 ± 0.22	31.6 ± 3.2
2MASS 0415–0935	T8	8	175.2 ± 1.7	2278.2 ± 1.2	1	16.92 ± 0.04	16.36 ± 0.04	13.51 ± 0.03	12.31 ± 0.13	15.47 ± 0.03	13.59 ± 0.03	61.6 ± 0.6
WISE 0430+4633	T8	8	93.9 ± 4.1	959.8 ± 3.2	Table 4	19.10 ± 0.15	...	14.27 ± 0.11	...	15.99 ± 0.10	14.08 ± 0.10	48.4 ± 2.1

Table 7
(Continued)

Object Name (1)	Spec. Type (2)	Spec. Code (3)	τ_{abs} (mas) (4)	μ_{total} (mas yr $^{-1}$) (5)	π , μ_{total} Reference (6)	M_H (mag) (7)	M_{W1} (mag) (8)	M_{W2} (mag) (9)	M_{W3} (mag) (10)	M_{ch1} (mag) (11)	M_{ch2} (mag) (12)	v_{tan} (km s $^{-1}$) (13)
WISE 0458+6434	T8.5	8.5	109.2 ± 3.6	357.7 ± 1.7	Table 4	17.60 ± 0.09	16.63 ± 0.10	13.21 ± 0.08	12.28 ± 0.29	15.27 ± 0.07	13.18 ± 0.07	15.5 ± 0.5
WISE 0500–1223	T8	8	95.1 ± 3.6	728.7 ± 1.8	Table 4	18.02 ± 0.15	17.34 ± 0.17	13.87 ± 0.09	...	15.84 ± 0.09	13.89 ± 0.08	36.3 ± 1.4
WISE 0512–3004	T8.5	8.5	48.9 ± 2.6	642.2 ± 1.8	Table 4	18.11 ± 0.43	17.08 ± 0.39	13.78 ± 0.14	...	16.09 ± 0.14	14.03 ± 0.12	62.3 ± 3.3
WISE 0513+0608	T6.5	6.5	70.8 ± 1.5	433.0 ± 1.0	Table 5	15.38 ± 0.09	15.09 ± 0.07	13.15 ± 0.06	...	14.35 ± 0.05	13.20 ± 0.05	29.7 ± 0.6
UGPS 0521+3640	T8.5	8.5	122.2 ± 1.6	1614.6 ± 1.3	Table 6	17.72 ± 0.05	14.83 ± 0.04	13.44 ± 0.04	11.59 ± 0.15	15.37 ± 0.04	14.01 ± 0.03	62.6 ± 0.8
WISE 0528–3308	T7pec	7	49.4 ± 3.9	19.5 ± 2.0	Table 6	15.44 ± 0.22	15.70 ± 0.20	12.99 ± 0.18	11.03 ± 0.45	14.78 ± 0.17	13.06 ± 0.17	1.9 ± 0.2
WISE 0535–7500	≥Y1:	11	66.4 ± 2.4	125.2 ± 1.6	Table 4	22.45 ± 0.35	17.05 ± 0.16	14.01 ± 0.09	...	16.86 ± 0.11	14.12 ± 0.08	8.9 ± 0.3
WISE 0540+4832	T8.5	8.5	70.0 ± 2.6	673.4 ± 2.1	Table 4	17.85 ± 0.09	...	14.21 ± 0.11	...	16.20 ± 0.09	13.99 ± 0.08	45.6 ± 1.7
WISE 0542–1628	T6.5	6.5	61.5 ± 2.7	366.3 ± 1.3	Table 6	15.51 ± 0.14	15.17 ± 0.11	12.90 ± 0.10	...	14.21 ± 0.10	12.91 ± 0.10	28.2 ± 1.2
GI 229B	T7pec	7	173.7 ± 0.1	731.7 ± 0.1	2	15.56 ± 0.05	20.0 ± 0.1
WISE 0612–3036AB	T6	6	41.1 ± 1.6	285.1 ± 1.8	Table 6	15.13 ± 0.14	14.47 ± 0.10	12.11 ± 0.09	...	13.66 ± 0.09	12.10 ± 0.09	32.9 ± 1.3
WISE 0614+3912	T6	6	53.7 ± 1.7	529.3 ± 1.2	Table 5	15.01 ± 0.26	14.89 ± 0.10	12.28 ± 0.08	...	13.84 ± 0.07	12.25 ± 0.07	48.2 ± 1.6
WISE 0614+0951	T7	7	65.6 ± 2.2	415.0 ± 1.6	Table 4	15.91 ± 0.08	15.71 ± 0.13	13.32 ± 0.09	...	14.57 ± 0.08	13.18 ± 0.08	30.0 ± 1.0
WISE 0623–0456	T8	8	87.4 ± 2.9	919.2 ± 1.4	Table 6	17.02 ± 0.13	16.55 ± 0.12	13.52 ± 0.08	12.11 ± 0.45	15.20 ± 0.08	13.44 ± 0.07	49.9 ± 1.7
WISE 0625+5646	T6	6	49.5 ± 2.0	52.7 ± 1.4	Table 5	15.37 ± 0.13	14.99 ± 0.12	12.90 ± 0.10	10.98 ± 0.49	13.94 ± 0.09	12.89 ± 0.09	5.2 ± 0.3
WISE 0627–1114	T6	6	74.8 ± 3.6	338.1 ± 1.6	Table 6	14.81 ± 0.13	14.35 ± 0.11	12.62 ± 0.11	10.90 ± 0.24	13.64 ± 0.11	12.69 ± 0.11	21.4 ± 1.0
WISE 0645–0302	T6	6	50.7 ± 4.2	318.9 ± 2.6	Table 4	15.86 ± 0.18	16.52 ± 0.37	13.39 ± 0.20	...	14.72 ± 0.18	13.21 ± 0.18	29.7 ± 2.6
WISE 0647–6232	Y1	11	100.3 ± 2.4	387.9 ± 1.5	Table 4	23.32 ± 0.18	...	15.23 ± 0.07	...	17.90 ± 0.11	15.08 ± 0.06	18.3 ± 0.4
WISE 0713–5854	T9	9	78.2 ± 4.6	367.5 ± 3.1	Table 4	18.95 ± 0.20	...	14.73 ± 0.14	...	16.76 ± 0.14	14.61 ± 0.13	22.3 ± 1.3
WISE 0713–2917	Y0	10	107.5 ± 2.4	546.2 ± 1.8	Table 4	20.35 ± 0.09	...	14.62 ± 0.07	12.45 ± 0.36	16.83 ± 0.06	14.38 ± 0.05	24.1 ± 0.5
UGPS 0722–0540	T9	9	242.8 ± 2.4	970.2 ± 2.1	6	18.83 ± 0.03	17.18 ± 0.05	14.13 ± 0.03	12.13 ± 0.07	16.22 ± 0.03	14.15 ± 0.03	18.9 ± 0.2
WISE 0723+3403	T9:	9	56.3 ± 3.5	343.8 ± 1.7	Table 4	17.38 ± 0.15	16.46 ± 0.26	13.44 ± 0.15	...	15.52 ± 0.14	13.44 ± 0.14	28.9 ± 1.8
2MASS 0727+1710	T7	7	112.5 ± 0.9	1296.2 ± 0.9	1	15.93 ± 0.03	15.44 ± 0.04	13.22 ± 0.03	12.18 ± 0.31	14.72 ± 0.03	13.27 ± 0.02	54.6 ± 0.4
2MASS 0729–3954	T8pec	8	126.3 ± 8.3	1738.3 ± 7.6	7	16.49 ± 0.23	15.80 ± 0.15	13.48 ± 0.14	11.87 ± 0.19	15.06 ± 0.14	13.50 ± 0.14	65.2 ± 4.3
WISE 0734–7157	Y0	10	75.0 ± 2.4	571.0 ± 1.8	Table 4	20.45 ± 0.10	18.12 ± 0.29	14.56 ± 0.09	...	17.02 ± 0.10	14.59 ± 0.07	36.1 ± 1.2
WISE 0744+5628	T8	8	67.1 ± 2.5	779.7 ± 1.7	Table 4	16.72 ± 0.14	16.31 ± 0.14	13.66 ± 0.09	11.78 ± 0.50	15.40 ± 0.09	13.69 ± 0.08	55.1 ± 2.1
WISE 0750+2725	T8.5	8.5	68.4 ± 3.4	783.2 ± 2.7	Table 6	18.18 ± 0.12	17.61 ± 0.44	13.73 ± 0.12	...	15.85 ± 0.12	13.66 ± 0.11	54.3 ± 2.7
WISE 0751–7634	T9	9	97.9 ± 6.7	216.7 ± 5.3	Table 6	19.63 ± 0.20	16.90 ± 0.16	14.48 ± 0.15	11.86 ± 0.21	16.37 ± 0.15	14.57 ± 0.15	10.5 ± 0.8
WISE 0759–4904	T8	8	89.1 ± 2.4	440.9 ± 1.6	Table 4	17.16 ± 0.07	16.75 ± 0.11	13.56 ± 0.07	...	15.37 ± 0.06	13.51 ± 0.06	23.5 ± 0.6
WD 0806B	[Y1]	11	52.2 ± 1.7	446.8 ± 1.8	8	23.88 ± 0.16	...	15.41 ± 0.11	...	18.24 ± 0.17	15.43 ± 0.09	40.6 ± 1.3
WISE 0811–8051	T9.5:	9.5	99.1 ± 7.7	293.4 ± 6.9	3	19.96 ± 0.22	16.74 ± 0.19	14.31 ± 0.17	12.61 ± 0.36	16.78 ± 0.18	14.37 ± 0.17	14.1 ± 1.2
WISE 0812+4021	T8	8	34.2 ± 2.7	259.6 ± 1.7	Table 4	15.97 ± 0.26	15.47 ± 0.28	12.94 ± 0.20	...	14.60 ± 0.18	12.97 ± 0.17	36.0 ± 2.9
DENIS 0817–6155	T6	6	203. ± 13.	1145.4 ± 67.8	9	15.07 ± 0.14	14.51 ± 0.14	12.80 ± 0.14	11.20 ± 0.14	13.78 ± 0.14	12.84 ± 0.14	26.7 ± 2.3
WISE 0825+2805	Y0.5	10.5	155.8 ± 2.4	241.2 ± 1.8	Table 4	23.93 ± 0.14	...	15.54 ± 0.07	...	18.29 ± 0.07	15.61 ± 0.04	7.3 ± 0.1
WISE 0833+0052	(sd)T9	9	82.6 ± 4.5	1776.1 ± 3.8	Table 4	20.21 ± 0.15	...	14.56 ± 0.14	...	16.59 ± 0.12	14.43 ± 0.12	101.9 ± 5.6
WISE 0836–1859	T8pec	8	40.8 ± 3.6	157.8 ± 1.8	Table 4	16.84 ± 0.32	15.68 ± 0.26	13.20 ± 0.21	...	14.92 ± 0.20	13.14 ± 0.19	18.3 ± 1.6
WISE 0855–0714	[≥ Y4]	14	438.9 ± 3.0	8147.3 ± 2.7	Table 4	27.04 ± 0.24	23.02 ± 0.42	16.92 ± 0.04	14.35 ± 0.13	20.68 ± 0.07	17.13 ± 0.02	88.0 ± 0.6
WISE 0857+5604	T8	8	87.2 ± 2.4	752.0 ± 1.6	Table 4	17.19 ± 0.15	16.82 ± 0.12	13.80 ± 0.07	...	15.72 ± 0.07	13.84 ± 0.06	40.9 ± 1.1
ULAS 0859+1010	T7	7	50.3 ± 1.7	712.7 ± 1.6	Table 6	17.09 ± 0.09	16.26 ± 0.24	13.67 ± 0.11	67.2 ± 2.3
ULAS 0901–0306	T7.5	7.5	62.6 ± 2.6	264.0 ± 3.6	10	17.44 ± 0.16	16.17 ± 0.16	13.54 ± 0.11	...	15.42 ± 0.10	13.52 ± 0.09	20.0 ± 0.9
WISE 0906+4735	T8	8	48.4 ± 3.4	895.3 ± 1.7	Table 4	16.23 ± 0.22	15.98 ± 0.23	12.97 ± 0.16	...	14.90 ± 0.16	12.97 ± 0.15	87.7 ± 6.2
WISE 0914–3459	T8	8	45.2 ± 4.2	177.0 ± 3.2	Table 4	...	15.89 ± 0.26	13.33 ± 0.21	...	15.02 ± 0.21	13.32 ± 0.20	18.6 ± 1.8
WISE 0929+0409	T6.5	6.5	41.0 ± 2.2	695.3 ± 3.5	Table 6	15.43 ± 0.14	14.61 ± 0.14	12.32 ± 0.13	10.44 ± 0.53	13.78 ± 0.12	12.30 ± 0.12	80.4 ± 4.3

Table 7
(Continued)

Object Name (1)	Spec. Type (2)	Spec. Code (3)	τ_{abs} (mas) (4)	μ_{total} (mas yr $^{-1}$) (5)	π , μ_{total} Reference (6)	M_H (mag) (7)	M_{W1} (mag) (8)	M_{W2} (mag) (9)	M_{W3} (mag) (10)	M_{ch1} (mag) (11)	M_{ch2} (mag) (12)	v_{tan} (km s $^{-1}$) (13)
2MASS 0937+2931	T6pec	6	162.8 ± 3.9	1622.0 ± 7.1	4	15.73 ± 0.06	15.15 ± 0.06	12.73 ± 0.06	11.75 ± 0.11	14.21 ± 0.05	12.75 ± 0.05	47.2 ± 1.2
2MASS 0939–2448	T8	8	187.3 ± 4.6	1191.7 ± 3.4	11	17.32 ± 0.10	16.27 ± 0.06	13.00 ± 0.06	12.03 ± 0.10	15.14 ± 0.06	12.98 ± 0.06	30.2 ± 0.7
WISE 0940–2208	T8	8	38.1 ± 4.7	224.3 ± 3.3	Table 4	...	14.77 ± 0.28	12.54 ± 0.27	...	14.30 ± 0.27	12.58 ± 0.27	27.9 ± 3.5
WISE 0943+3607	T9.5	9.5	93.8 ± 2.8	839.4 ± 1.9	Table 4	20.18 ± 0.08	18.04 ± 0.30	14.27 ± 0.08	12.15 ± 0.40	16.61 ± 0.08	14.15 ± 0.07	42.4 ± 1.3
ULAS 0950+0117	T8	8	57.9 ± 2.3	434.1 ± 1.3	Table 6	17.21 ± 0.10	16.45 ± 0.20	13.32 ± 0.10	...	15.12 ± 0.09	13.24 ± 0.09	35.5 ± 1.4
WISE 0952+1955	T6	6	41.1 ± 3.9	47.1 ± 2.0	Table 4	15.29 ± 0.23	14.91 ± 0.24	12.53 ± 0.21	...	13.88 ± 0.21	12.57 ± 0.21	5.4 ± 0.6
WISE 1018–2445	T8	8	83.6 ± 3.6	823.2 ± 1.8	Table 4	17.61 ± 0.25	16.88 ± 0.17	13.74 ± 0.10	...	15.74 ± 0.10	13.75 ± 0.10	46.7 ± 2.0
WISE 1019+6529	T6	6	42.9 ± 1.8	150.6 ± 1.1	Table 5	14.68 ± 0.15	14.44 ± 0.10	12.16 ± 0.10	...	13.47 ± 0.09	12.16 ± 0.09	17.3 ± 0.8
WISE 1025+0307	T8.5	8.5	85.4 ± 2.5	1208.0 ± 1.9	Table 4	18.02 ± 0.08	17.14 ± 0.20	13.79 ± 0.08	...	15.97 ± 0.07	13.85 ± 0.07	67.0 ± 2.0
CFBDS 1028+5654	T8	8	45.0 ± 2.9	201.2 ± 2.1	Table 4	16.65 ± 0.16	14.63 ± 0.14	12.74 ± 0.14	21.2 ± 1.4
ULAS 1029+0935	T8	8	66.8 ± 4.2	436.9 ± 3.2	Table 6	16.75 ± 0.14	15.90 ± 0.18	13.50 ± 0.16	...	15.21 ± 0.14	13.58 ± 0.14	31.0 ± 2.0
WISE 1039–1600	T7.5	7.5	53.4 ± 2.6	223.8 ± 1.9	Table 4	15.83 ± 0.11	15.11 ± 0.13	12.81 ± 0.11	...	14.51 ± 0.11	12.84 ± 0.11	19.9 ± 1.0
WISE 1042–3842	T8.5	8.5	65.4 ± 3.4	93.7 ± 6.2	3	18.27 ± 0.12	17.34 ± 0.32	13.61 ± 0.12	...	15.83 ± 0.12	13.63 ± 0.12	6.9 ± 0.6
ULAS 1043+1048	T8	8	20.8 ± 7.0	141.9 ± 3.7	Table 4	15.12 ± 0.73	15.03 ± 0.87	12.28 ± 0.74	...	13.61 ± 0.73	12.00 ± 0.73	32.3 ± 10.
2MASS 1047+2124	T6.5	6.5	94.7 ± 3.8	1728.4 ± 7.7	4	15.71 ± 0.09	15.26 ± 0.09	12.89 ± 0.09	11.75 ± 0.32	14.29 ± 0.09	12.88 ± 0.09	86.5 ± 3.5
WISE 1050+5056	T8	8	49.7 ± 5.0	432.3 ± 3.3	Table 4	16.79 ± 0.22	16.42 ± 0.32	13.34 ± 0.23	...	15.03 ± 0.22	13.38 ± 0.22	41.2 ± 4.2
WISE 1051–2138	T8.5	8.5	67.0 ± 3.0	207.9 ± 2.0	Table 4	18.32 ± 0.40	16.43 ± 0.17	13.73 ± 0.11	...	15.55 ± 0.10	13.73 ± 0.10	14.7 ± 0.7
WISE 1052–1942	T7.5	7.5	62.3 ± 4.4	453.5 ± 2.7	Table 4	16.03 ± 0.19	15.56 ± 0.17	13.08 ± 0.16	...	14.64 ± 0.16	13.19 ± 0.15	34.5 ± 2.4
WISE 1055–1652	T9.5	9.5	72.2 ± 2.7	1074.6 ± 2.0	Table 4	14.36 ± 0.11	...	16.59 ± 0.10	14.34 ± 0.08	70.6 ± 2.6
2MASS 1114–2618	T7.5	7.5	179.2 ± 1.4	3043.2 ± 1.1	1	17.09 ± 0.05	16.52 ± 0.04	13.54 ± 0.03	12.61 ± 0.18	15.45 ± 0.03	13.62 ± 0.02	80.5 ± 0.6
WISE 1118+3125	T8.5	8.5	113.2 ± 4.6	745.4 ± 2.8	18, 12	18.42 ± 0.11	16.43 ± 0.10	13.61 ± 0.09	12.51 ± 0.34	15.87 ± 0.09	13.64 ± 0.09	31.2 ± 1.3
WISE 1122+2550	T6	6	66.3 ± 2.3	1028.6 ± 1.2	Table 5	15.75 ± 0.13	15.19 ± 0.10	13.20 ± 0.09	...	14.47 ± 0.08	13.21 ± 0.08	75.4 ± 2.7
WISE 1124–0421	T7	7	61.6 ± 3.1	556.5 ± 2.3	Table 4	...	15.39 ± 0.14	13.00 ± 0.12	...	14.32 ± 0.11	13.04 ± 0.11	42.8 ± 2.2
WISE 1139–3324	T7	7	27.0 ± 3.9	110.2 ± 3.1	Table 4	15.10 ± 0.32	15.63 ± 0.50	12.06 ± 0.32	...	14.05 ± 0.32	12.15 ± 0.31	19.3 ± 2.8
WISE 1141–3326	Y0	10	99.7 ± 4.2	907.6 ± 3.4	Table 4	...	17.07 ± 0.15	14.60 ± 0.11	11.72 ± 0.23	16.41 ± 0.10	14.65 ± 0.09	43.2 ± 1.8
WISE 1143+4431	T8.5	8.5	38.1 ± 6.5	104.7 ± 7.2	Table 4	16.94 ± 0.38	16.63 ± 0.53	13.09 ± 0.38	...	15.05 ± 0.37	13.06 ± 0.37	13.1 ± 2.4
WISE 1150+6302	T8	8	124.5 ± 3.0	678.0 ± 2.2	Table 4	...	17.43 ± 0.10	13.88 ± 0.06	12.85 ± 0.31	16.09 ± 0.06	13.90 ± 0.06	25.8 ± 0.6
ULAS 1152+1134	T8.5	8.5	49.7 ± 5.1	493.0 ± 4.2	Table 4	17.14 ± 0.24	15.31 ± 0.25	13.13 ± 0.23	...	14.76 ± 0.23	13.26 ± 0.22	47.0 ± 4.8
WISE 1206+8401	Y0	10	81.9 ± 2.5	629.3 ± 1.7	Table 4	20.63 ± 0.09	...	14.62 ± 0.09	...	16.91 ± 0.09	14.79 ± 0.07	36.4 ± 1.1
2MASS 1217–0311	T7.5	7.5	91.7 ± 2.2	1057.1 ± 1.7	13	15.79 ± 0.06	15.08 ± 0.07	13.02 ± 0.06	11.52 ± 0.27	14.56 ± 0.06	13.10 ± 0.06	54.6 ± 1.3
WISE 1217+1626	T9	9	104.4 ± 4.7	1463.8 ± 2.3	Table 4	18.26 ± 0.10	16.64 ± 0.13	13.22 ± 0.10	12.12 ± 0.33	15.53 ± 0.10	13.20 ± 0.10	66.5 ± 3.0
WISE 1220+5407	T9.5	9.5	42.7 ± 7.1	365.3 ± 9.6	Table 4	...	17.38 ± 0.63	13.91 ± 0.37	...	16.16 ± 0.37	13.87 ± 0.36	40.6 ± 6.8
WISE 1221–3136	T6.5	6.5	73.8 ± 3.3	728.5 ± 3.0	Table 4	15.40 ± 0.20	15.22 ± 0.11	13.21 ± 0.10	11.46 ± 0.34	14.43 ± 0.10	13.23 ± 0.10	46.8 ± 2.1
2MASS 1225–2739	T6	6	76.0 ± 2.5	736.8 ± 2.9	13	14.50 ± 0.11	14.07 ± 0.08	12.13 ± 0.08	10.56 ± 0.16	13.30 ± 0.07	12.15 ± 0.07	46.0 ± 1.5
WISE 1225–1013	T6	6	43.3 ± 3.0	361.2 ± 2.3	Table 4	14.59 ± 0.15	14.38 ± 0.16	12.18 ± 0.16	10.47 ± 0.43	13.49 ± 0.15	12.14 ± 0.15	39.5 ± 2.8
2MASS 1231+0847	T5.5	5.5	75.8 ± 4.8	1564.0 ± 4.7	Table 4	14.71 ± 0.18	14.47 ± 0.14	12.48 ± 0.14	11.63 ± 0.41	13.67 ± 0.14	12.48 ± 0.14	97.8 ± 6.2
2MASS 1237+6526	T6.5	6.5	96.1 ± 4.8	1131.4 ± 8.9	4	15.85 ± 0.15	15.29 ± 0.11	12.85 ± 0.11	11.85 ± 0.25	14.34 ± 0.11	12.86 ± 0.11	55.8 ± 2.8
ULAS 1238+0953	T8	8	44.1 ± 6.1	448.4 ± 4.0	Table 6	17.42 ± 0.30	16.76 ± 0.55	13.56 ± 0.32	...	15.36 ± 0.30	13.59 ± 0.30	48.2 ± 6.7
WISE 1243+8445	T9	9	48.6 ± 4.5	745.5 ± 3.9	Table 4	17.64 ± 0.21	16.99 ± 0.34	14.00 ± 0.21	...	15.79 ± 0.21	13.84 ± 0.20	72.7 ± 6.7
WISE 1254–0728	T7	7	47.2 ± 4.4	131.6 ± 4.7	Table 4	16.00 ± 0.20	15.15 ± 0.23	13.22 ± 0.22	...	14.70 ± 0.21	13.19 ± 0.20	13.2 ± 1.3
WISE 1257+4008	T7	7	45.7 ± 8.2	365.4 ± 7.3	Table 4	15.26 ± 0.41	14.97 ± 0.40	12.73 ± 0.39	...	14.22 ± 0.39	12.79 ± 0.39	37.9 ± 6.8
VHS 1258–4412	T6	6	63.8 ± 4.0	208.2 ± 3.2	Table 4	...	14.69 ± 0.14	13.04 ± 0.14	11.13 ± 0.30	13.93 ± 0.14	13.02 ± 0.14	15.5 ± 1.0
GI 494C	T8	8	86.9 ± 0.2	633.2 ± 0.5	2	16.71 ± 0.04	15.74 ± 0.06	13.54 ± 0.04	11.40 ± 0.27	15.06 ± 0.02	13.55 ± 0.02	34.5 ± 0.1
WISE 1301–0302	T8.5	8.5	53.8 ± 5.6	381.6 ± 3.6	Table 4	17.04 ± 0.23	16.27 ± 0.29	13.52 ± 0.24	...	15.29 ± 0.23	13.55 ± 0.23	33.6 ± 3.5

Table 7
(Continued)

Object Name (1)	Spec. Type (2)	Spec. Code (3)	π_{abs} (mas) (4)	μ_{total} (mas yr ⁻¹) (5)	π, μ_{total} Reference (6)	M_H (mag) (7)	M_{W1} (mag) (8)	M_{W2} (mag) (9)	M_{W3} (mag) (10)	M_{ch1} (mag) (11)	M_{ch2} (mag) (12)	v_{tan} (km s ⁻¹) (13)
WISE 2325-4105	T9pec	9	108.4 ± 3.7	837.0 ± 6.7	3	19.38 ± 0.13	17.23 ± 0.14	14.27 ± 0.08	...	16.43 ± 0.08	14.25 ± 0.08	36.8 ± 1.3
ULAS 2326+0201	T8	8	49.5 ± 4.6	310.4 ± 3.3	Table 4	16.93 ± 0.23	16.43 ± 0.36	14.00 ± 0.24	...	15.35 ± 0.20	13.92 ± 0.20	29.7 ± 2.8
WISE 2332-4325	T9:	9	65.3 ± 2.6	353.3 ± 1.9	Table 4	18.64 ± 0.17	17.05 ± 0.26	14.03 ± 0.11	...	16.35 ± 0.10	14.09 ± 0.09	25.6 ± 1.0
WISE 2340-0745	T7	7	47.8 ± 3.1	293.1 ± 1.4	Table 5	14.59 ± 0.15	14.33 ± 0.15	12.00 ± 0.15	...	13.59 ± 0.14	12.02 ± 0.14	30.1 ± 2.0
ULAS 2342+0856	T6.5	6.5	39.9 ± 2.8	265.8 ± 2.1	Table 6	14.73 ± 0.16	13.97 ± 0.16	11.96 ± 0.16	...	13.29 ± 0.15	11.99 ± 0.15	31.6 ± 2.2
WISE 2343-7418	T6	6	58.8 ± 2.7	426.8 ± 1.8	Table 4	14.99 ± 0.11	14.52 ± 0.11	12.60 ± 0.10	11.63 ± 0.51	13.88 ± 0.10	12.60 ± 0.10	34.4 ± 1.6
WISE 2344+1034	T9	9	64.7 ± 3.7	942.4 ± 1.9	Table 4	18.12 ± 0.17	17.19 ± 0.37	14.00 ± 0.15	...	15.79 ± 0.13	13.96 ± 0.13	69.0 ± 4.0
WISE 2348-1028	T7	7	58.4 ± 3.5	642.5 ± 1.5	Table 5	15.76 ± 0.18	15.48 ± 0.16	13.21 ± 0.14	...	14.70 ± 0.13	13.19 ± 0.13	53.6 ± 3.3
WISE 2354+0240	Y1	11	124.1 ± 4.9	629.1 ± 4.1	Table 4	23.35 ± 0.31	...	15.48 ± 0.12	...	18.57 ± 0.14	15.48 ± 0.09	24.0 ± 1.0
WISE 2357+1227	T6	6	59.5 ± 4.1	501.1 ± 4.1	Table 4	15.36 ± 0.15	14.61 ± 0.16	12.89 ± 0.15	10.97 ± 0.40	14.13 ± 0.15	12.98 ± 0.15	40.0 ± 2.9

References. References for parallax and total motions: (1) Dupuy & Liu (2012), (2) Gaia Collaboration et al. (2018), (3) Tinney et al. (2014), (4) Vrba et al. (2004), (5) Gaia Collaboration et al. (2016), (6) Leggett et al. (2012), (7) Faherty et al. (2012), (8) Subasavage et al. (2009), (9) Artigau et al. (2010), (10) Marocco et al. (2010), (11) Burgasser et al. (2008b), (12) Zacharias et al. (2012), (13) Tinney et al. (2003), (14) Manjavacas et al. (2013), (15) Henry et al. (2006), (16) Harrington & Dahn (1980), (17) Smart et al. (2013), (18) van Altena et al. (1995).

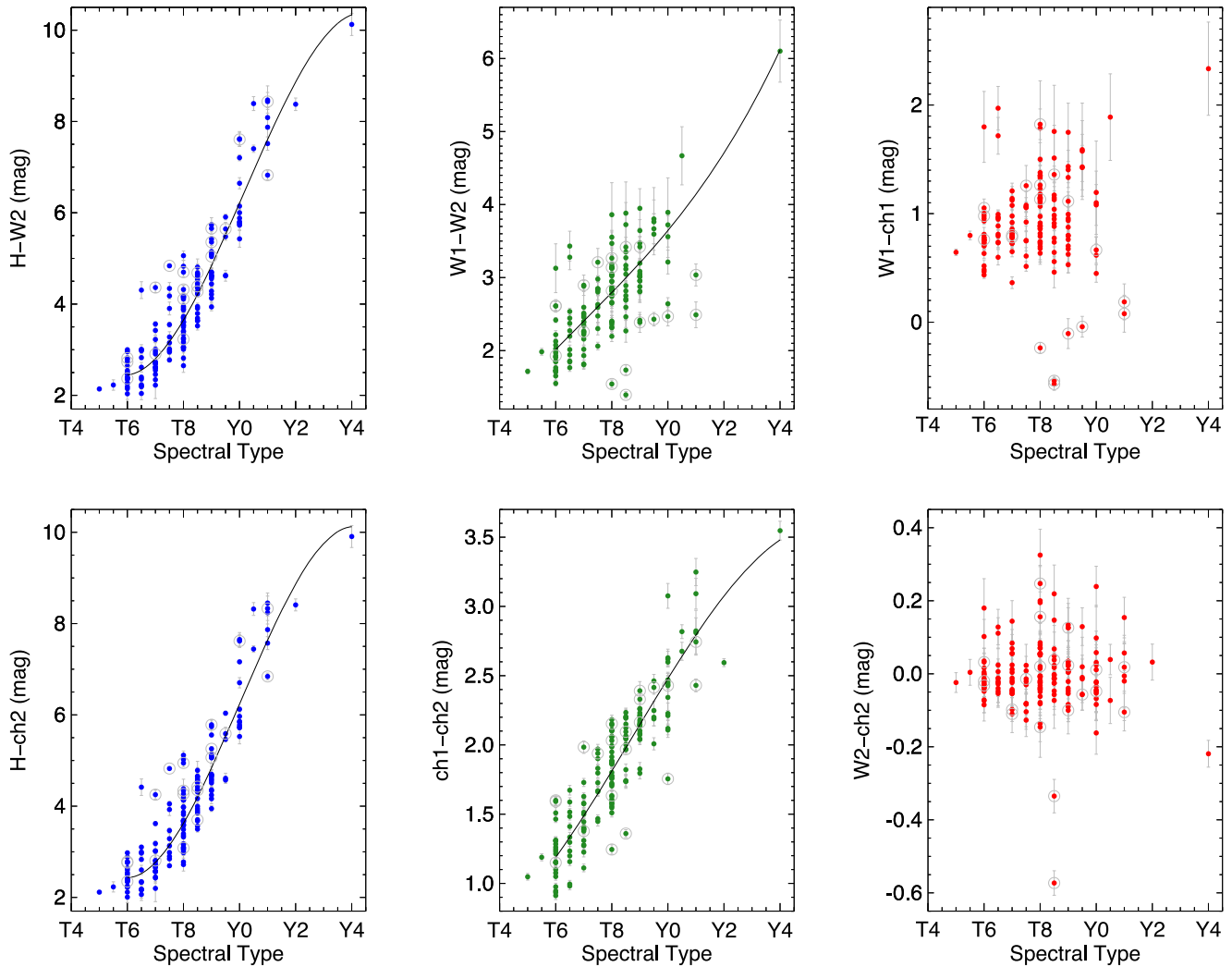


Figure 4. Trends of color with spectral type for all objects from Table 7 that fall within 20 pc of the Sun ($\pi_{\text{abs}} \geq 50$ mas). Shown as blue points in the two leftmost panels are trends with $H-W2$ and $H\text{-}ch2$ color. The two middle panels show trends of $W1-W2$ and $ch1\text{-}ch2$ color (green points). The two rightmost panels show trends of $W1\text{-}ch1$ and $W2\text{-}ch2$ color (red points). Polynomial fits to the relations in the four leftmost panels are shown by the black curves, and the functional forms are presented in Table 8. Points ignored by the fitting (see Section 8.3) are circled in gray.

we list the *WISE* $W1$, $W2$, and $W3$ photometry, although the last of these bands is generally not sensitive enough to detect these brown dwarfs well. In some cases, the object is sufficiently faint in the $W1$ band that it is not detected well there, either. We also list photometry in the *Spitzer*/*IRAC* $ch1$ and $ch2$ bands.

8.1. Identifying Outliers from the Mean Trends

As we have large numbers of objects with accurate parallaxes, motions, and photometry, we can now examine trends across the late-T and early-Y spectral types, particularly in relation to the 20 pc sample we are building for mass function analysis. The goal of this section is to examine these trends in an effort to identify outliers that may need special handling in Section 9.3. In some cases, outliers may indicate unresolved binarity, and this is an issue because we want to have the most accurate accounting possible of the number of objects within our sample volume. In other cases, outliers may indicate unusual spectroscopic features which may confuse our translation of an observational parameter such as spectral type or color into a physical parameter such as effective

temperature. In this subsection, we identify plots useful for identifying unusual objects, and in Section 8.2 we discuss each of these objects in detail so that they will be properly handled during the mass function computation. In the following figures, only those objects with solid measurements in both axes are plotted—i.e., objects having absolute magnitude limits or color limits are removed.

Shown in the leftmost panels of Figure 4 (blue points) are trends of $H-W2$ and $H\text{-}ch2$ color with spectral type. These colors are very similar because the $W2$ and $ch2$ bands sample a similar range in wavelength near the peak flux in cold brown dwarfs (see Figure 2 of Mainzer et al. 2011). A number of outliers stand out as having unusually red colors for their types between T6.5 and T8.

The middle panels of Figure 4 (green points) show the trends of $W1-W2$ and $ch1\text{-}ch2$ color with spectral type. Notable here are a handful of objects with significantly blue colors, especially on the $ch1\text{-}ch2$ plot.

The rightmost panels in Figure 4 (red points) show the trends of $W1\text{-}ch1$ and $W2\text{-}ch2$ color with spectral type. Given the similarity of the $W2$ and $ch2$ filters, one would expect the

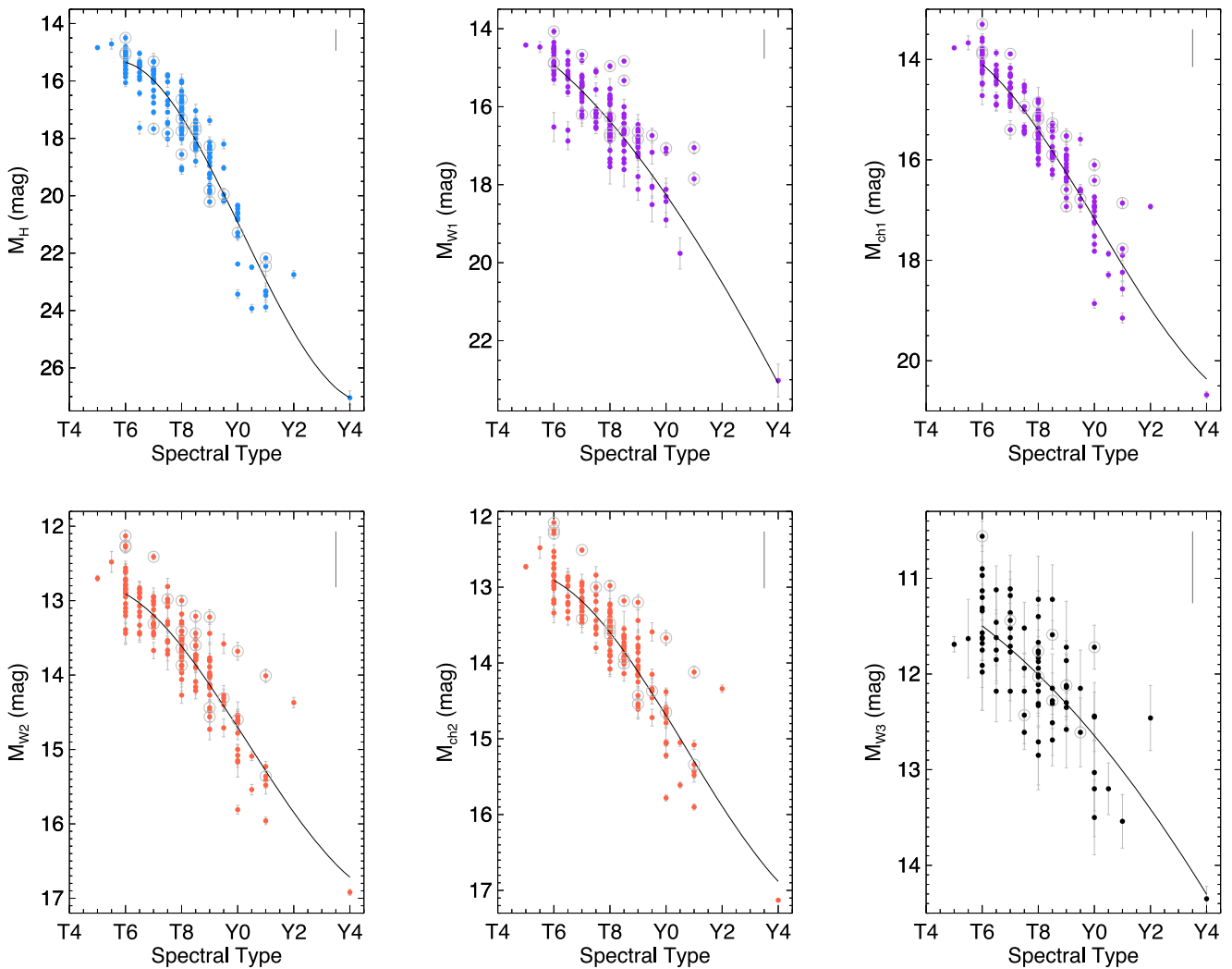


Figure 5. Trends of absolute magnitude with spectral type for all objects from Table 7 that fall within 20 pc of the Sun ($\pi_{\text{abs}} \geq 50$ mas). The top row shows trends with absolute H -band magnitude (light blue) and the similar absolute $W1$ and $ch1$ magnitudes (purple). The bottom row shows trends with the similar absolute $W2$ and $ch2$ magnitudes (orange red) and the absolute $W3$ magnitude (black). Polynomial fits to the relations are shown by the black curves, and the functional forms are presented in Table 8. Points ignored by the fitting (see Section 8.3) are circled in gray. The light gray bar at the upper right of each panel shows the size of the 0.75 mag offset expected for an equal-magnitude binary.

$W2$ – $ch2$ color to fall near zero, which it does. Objects falling significantly far from zero color are probably contaminated by a background source in one of the two bands. The $W1$ and $ch1$ filters, on the other hand, sample slightly different wavelengths, with the $W1$ band centered squarely on the fundamental methane absorption feature near $3.3 \mu\text{m}$ and the $ch1$ band lying somewhat redward of this and sampling more of the rise in the brown dwarf spectrum near $4.0 \mu\text{m}$ (Figure 2 of Mainzer et al. 2011). As expected, objects are generally fainter in the $W1$ band than in the $ch1$ band, but the plot shows a few exceptions that again are likely to be objects with contaminated photometry in one of the bands.

Shown in Figure 5 are trends of absolute magnitude with spectral type. Despite the small uncertainties on these measurements, there is a surprisingly large scatter of absolute magnitude in all bands at each spectral subclass. At $W2$ and $ch2$, there is typically a magnitude of scatter at each late-T subclass, and this increases to two magnitudes at H , $W1$, and $ch1$. (The uncertainties at $W3$ are large enough that interpretation is more difficult.) At $Y0$, this scatter increases by roughly

another magnitude in all bands. Despite this dispersion, we nonetheless can identify some objects that fall significantly further off the trends than the others.

On the absolute $W1$ and $ch1$ plots of Figure 5, we consider a T dwarf to be unusual if it is a clear outlier on *both* plots, since the T dwarfs in our sample generally have solid photometry in both bands. For the absolute $W2$ and $ch2$ plots, we consider an object to be unusual only if it appears as a significant outlier at both bands, and we can apply this strategy to T *and* Y dwarfs because both are easily detected at these wavelengths.

Figure 6 shows trends of absolute magnitudes with $ch1$ – $ch2$ color. There is a linear trend of decreasing absolute magnitude with increasing $ch1$ – $ch2$ color, but with a notable inflection point in most of the plots near $ch1$ – $ch2 \approx 2.2$ mag, corresponding to the transition between types T and Y (see Figure 4).

Figure 7 shows the trend of absolute magnitudes with H – $W2$ color. These trends appear more linear than those with $ch1$ – $ch2$ color above in that there is not a clear inflection point at the T/Y transition, corresponding to H – $W2 \approx 6.5$ mag,

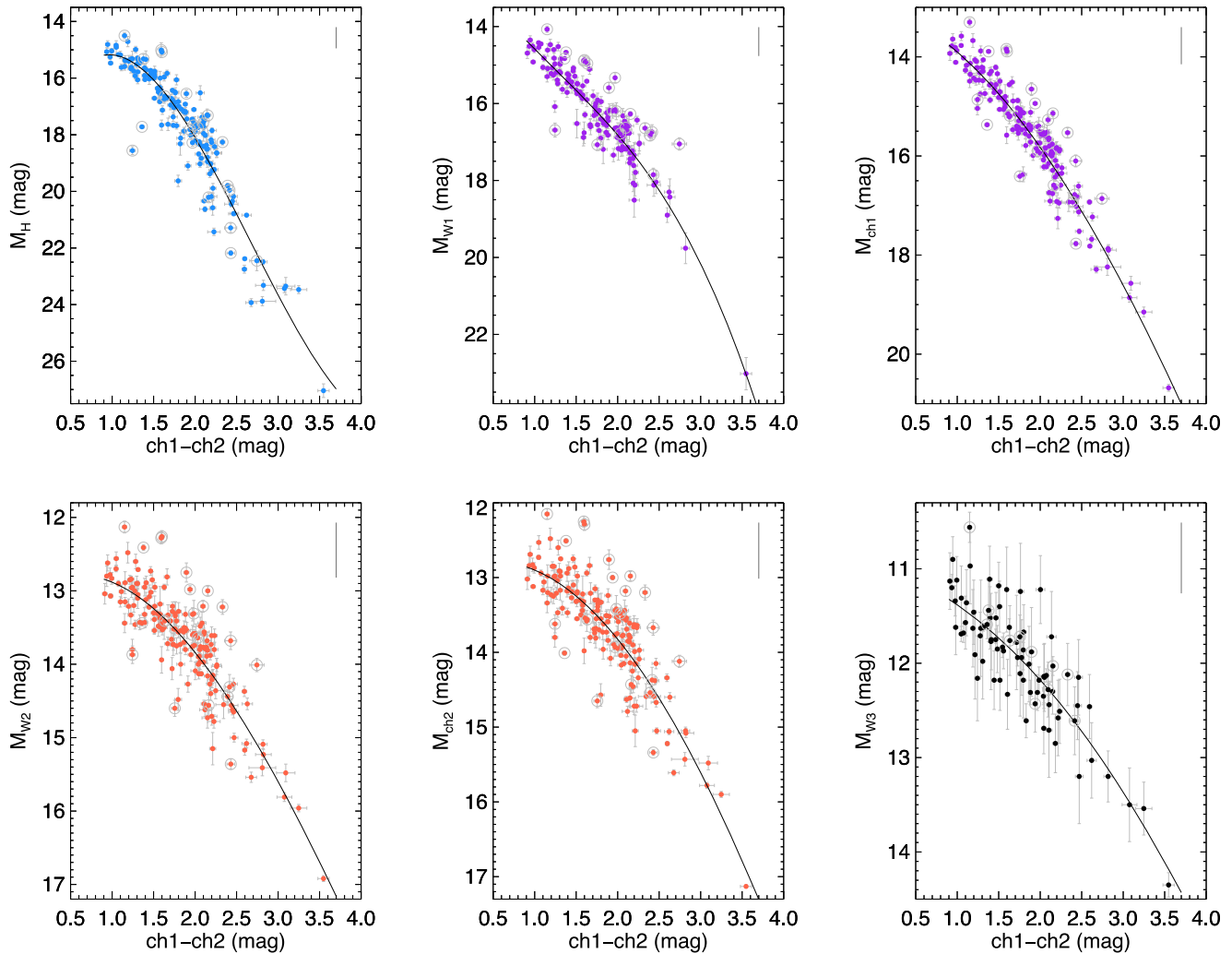


Figure 6. Trends of absolute magnitude with $\text{ch1}-\text{ch2}$ color for all objects from Table 7 that fall within 20 pc of the Sun ($\pi_{\text{abs}} \geq 50$ mas). The top row shows trends with absolute H -band magnitude (light blue) and the similar absolute W1 and ch1 magnitudes (purple). The bottom row shows trends with the similar absolute W2 and ch2 magnitudes (orange red) and the absolute W3 magnitude (black). Polynomial fits to the relations are shown by the black curves, and the functional forms are presented in Table 8. Points ignored by the fitting (see Section 8.3) are circled in gray. The light gray bar at the upper right of each panel shows the size of the 0.75 mag offset expected for an equal-magnitude binary.

although data redder than this value are not plentiful. The plot of M_H versus $H-W2$ color shows a tight correlation between quantities, so we examine this plot in detail in Figure 8. The tight correlation allows us to identify close binary systems that may or may not already be known. Unresolved, equal-magnitude doubles would be expected to fall 0.75 mag above the canonical sequence, and there are a number of objects that appear to lie at roughly this level above the mean trend. For reference, we label and circle in red all of the known doubles. Other objects, not known to be doubles, exhibit the same overluminosity. We also label the locations of the known subdwarfs on this diagram with blue circles. This shows that—with the exception of ULAS 1416+1348, which may itself be an unresolved double—these objects fall on the main locus. There are a few objects that also inhabit an area below the main trend.

Finally, we plot a histogram of the measured tangential velocities in Figure 9 along with trends of v_{tan} as a function of $H-W2$ color and M_H . Spectroscopically identified subdwarfs are circled in blue in the right-hand panels. The two highest v_{tan}

values belong to the subdwarfs WISE 2005+5424 (110 km s^{-1}) and WISE 0833+0052 (102 km s^{-1}). In comparison, for a sample of 841 late-M, L, and T dwarfs, Faherty et al. (2009) find a median v_{tan} value of 26 km s^{-1} and only 1.7% (14/841) with v_{tan} values in excess of 100 km s^{-1} , similar to the percentage we find at late-T and Y types ($2/180 = 1.1\%$).

Objects appearing as outliers on any of these plots or having high reduced χ^2 values from our *Spitzer*-based astrometric fitting are discussed below.

8.2. Notes of Interest on Individual Objects within 20 pc

8.2.1. WISE 0146+4234AB

As noted by Dupuy et al. (2015), this is a tight binary of separation $0''.0875 \pm 0''.0021$ with components believed to be of types T9 and Y0. The reduced χ^2 value of 1.579 for our *Spitzer* astrometric solution does not indicate any serious issue with the single-object fit despite the double nature of the system and the relatively short orbital period, estimated to be ~ 6 yr

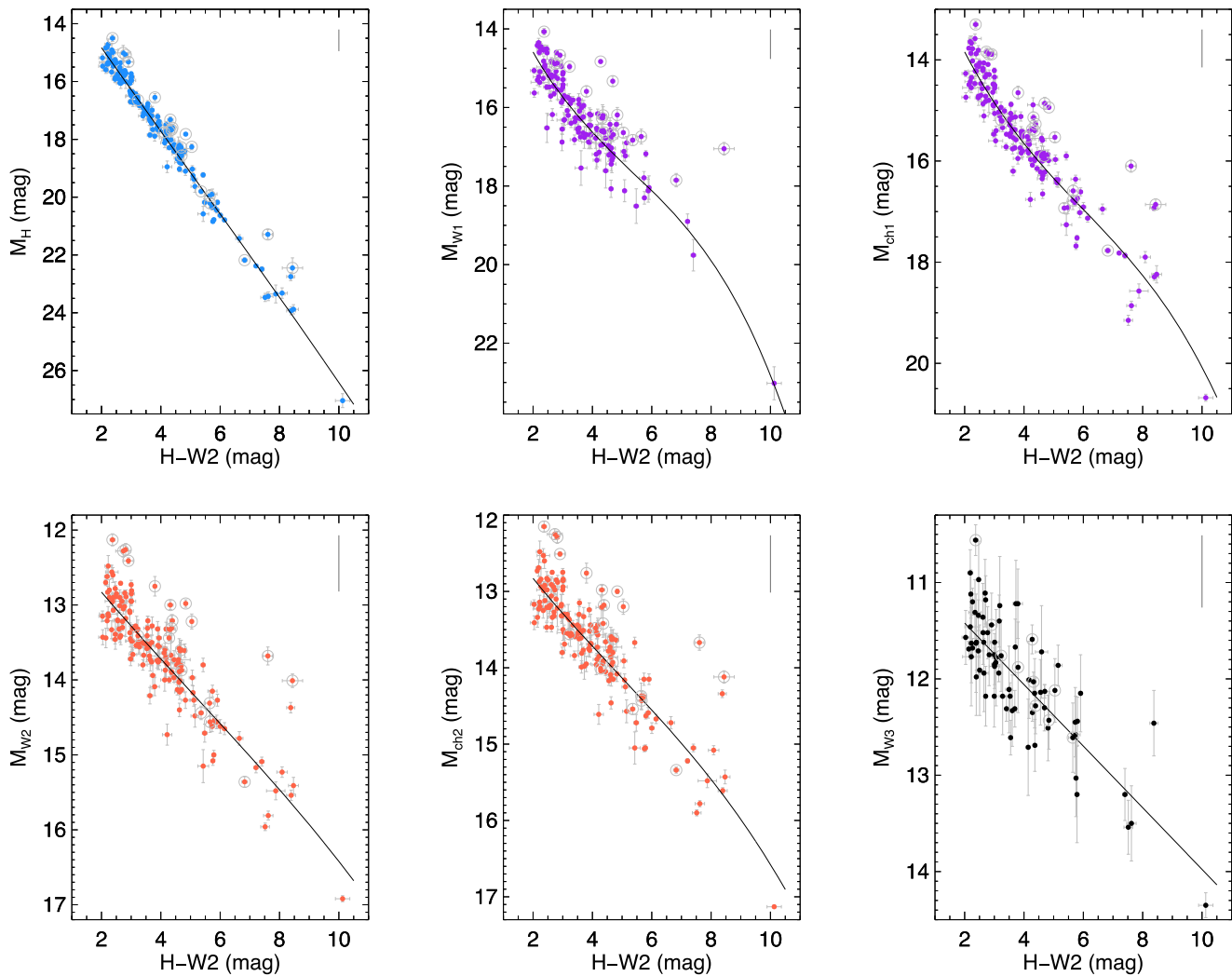


Figure 7. Trends of absolute magnitude with $H-W2$ color for all objects from Table 7 that fall within 20 pc of the Sun ($\pi_{\text{abs}} \geq 50$ mas). The top row shows trends with absolute H -band magnitude (light blue) and the similar absolute $W1$ and $ch1$ magnitudes (purple). The bottom row shows trends with the similar absolute $W2$ and $ch2$ magnitudes (orange red) and the absolute $W3$ magnitude (black). (Plots of absolute magnitude with H - $ch2$ color look virtually identical to the plots shown here.) Polynomial fits to the relations are shown by the black curves, and the functional forms are presented in Table 8. Points ignored by the fitting (see Section 8.3) are circled in gray. The light gray bar at the upper right of each panel shows the size of the 0.75 mag offset expected for an equal-magnitude binary.

(Dupuy et al. 2015). As seen in Figure 8, its overluminosity is nonetheless evident relative to other late-T and early-Y dwarfs.

8.2.2. WISE 0226–0211AB

This is a previously unreported common-proper-motion double with a separation of $\sim 2''.1$ arcsec. This object has the worst reduced χ^2 value of any of our *Spitzer* targets (23.645) because the MOPEX/APEX software is unable to successfully centroid on either the A or the B component individually. Figure 10 shows the motion of the pair over a 6.6 yr baseline. This pair was observed with Keck/NIRC2 at J and H bands on dates 2013 September 21 and August 22 (UT), respectively, from which we measure PRF-fit magnitudes of $J = 18.57 \pm 0.05$ and $H = 18.88 \pm 0.10$ mag for the northern A component and $J = 22.33 \pm 0.07$ and $H = 22.33 \pm 0.12$ mag for the southern B component. Aperture photometry was measured on the first-epoch *Spitzer* AOR images (which had contemporaneous $ch1$ and $ch2$ images), and we obtained measurements of $ch1 = 16.67 \pm 0.17$ and $ch2 = 14.86 \pm 0.05$ mag for A and $ch1 = 18.38 \pm 0.92$ and $ch2 = 15.59 \pm 0.08$ mag for B. The corresponding H - $ch2$ colors are 4.02 ± 0.11 mag for A and

6.74 ± 0.14 mag for B, suggesting types of $\sim T8$ – $T8.5$ for A and $\sim Y0$ for B (Figure 4). Using our measured parallax, which is somewhat suspect given our inability to properly centroid the pair, we find absolute magnitudes of $M_H = 17.67$ and $M_{ch2} = 13.65$ mag for A and $M_H = 21.12$ and $M_{ch2} = 14.38$ mag for B, suggesting types of $\sim T8$ – $T8.5$ and $\sim T9.5$ – $Y0$ for the two components (Figure 5), consistent with the type derived above from the colors and the absolute magnitudes, despite the agreement between the colors and the absolute magnitudes, the combined-light spectrum is that of a T7 dwarf (Kirkpatrick et al. 2011), when expectations would suggest a type closer to T8 or T9. This spectral type determination, based on a noisy H -band-only spectrum, should be revisited in light of the dual nature of the source. This source is the reddest T7 in H - $W2$ color and is very faint in M_H for its spectral type despite being a binary, suggesting that the type itself is probably in error.

8.2.3. WISE 0254+0223

This T8 dwarf has a higher-than-average v_{tan} value of 84.4 ± 0.9 km s $^{-1}$, but it shows no oddities in the color and magnitude trends. High-quality spectra from 0.8 to 2.5 μm

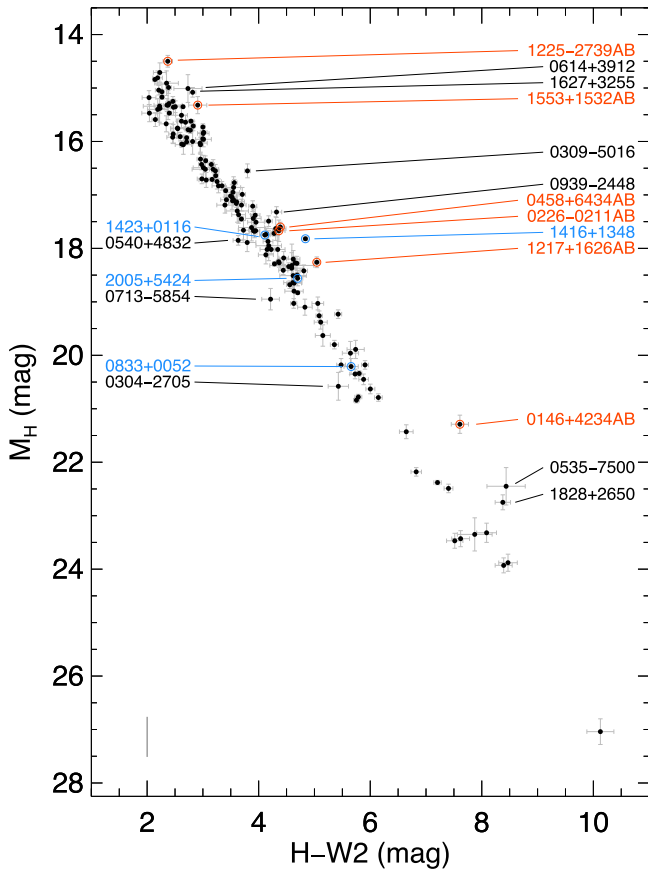


Figure 8. Trends of absolute H -band magnitude with H - $W2$ color for all objects from Table 7 that fall within 20 pc of the Sun ($\pi_{\text{abs}} \geq 50$ mas). Known binary systems are circled and labeled in red, and known subdwarfs are circled and labeled in blue. Other objects falling significantly above or below the mean trend are labeled in black. The light gray bar at the lower left shows the size of the 0.75 mag offset expected for an equal-magnitude binary.

(Figure 22 of Kirkpatrick et al. 2011; Figure 3 of Liu et al. 2011) show it to be a normal T8 dwarf of presumably solar metallicity.

8.2.4. WISE 0304–2705

The *Spitzer* astrometric fit for this object has a reduced χ^2 value of 2.812. Additional observations of this object are warranted, particularly since this is a peculiar Y0 dwarf. Pinfield et al. (2014b) argued that the peculiar spectrum was most likely caused by an unusual metallicity and/or gravity. However, the fact that the object is too dim in M_H for its H - $W2$ color (Figure 8) while other known subdwarfs do not share this effect may suggest that metallicity is not the sole cause. Continued astrometric monitoring is needed to determine if binarity may be complicating the analysis, but in our subsequent analysis we consider this to be a single Y dwarf.

8.2.5. WISE 0309–5016

This source is much brighter in M_H than other objects of similar H - $W2$ color, and also much brighter in M_{W1} and M_{ch1} than other objects of similar ch1 - ch2 color. This evidence points at WISE 0309–5016 being an unresolved double. There is no spectrum yet of this object, but methane on/off imaging suggests a spectral type of \sim T7 (Tinney et al. 2018).

8.2.6. WISE 0316+4307

In H - $W2$ and H - ch2 colors, this is an abnormally red T8, and it is faint in M_H for its type. The spectral type is robust, since it is based on separate, high-quality spectra at J and H bands (Mace et al. 2013a), so the reasons for these peculiarities are not known.

8.2.7. WISE 0323–5907

This object is too faint in M_{W1} and M_{ch1} for its ch1 - ch2 color. There is no spectrum yet of this object, but the ch1 - ch2 color of 1.244 ± 0.034 mag suggests a type of \sim T6 (Figure 4), in agreement with the photometric type assigned by Schneider et al. (2016) using 2MASS and AllWISE photometry.

8.2.8. WISE 0335+4310

The poor reduced χ^2 value of 3.227 for this object's *Spitzer* astrometric fit is driven primarily by large residuals in the final year of data. For these later epochs, the T9 has moved within $\sim 4''$ of a fainter background star, but that should not be complicating the astrometric measurement.

8.2.9. WISE 0350–5658

This Y1 dwarf is too faint for its spectral type in both M_{W2} and M_{ch2} . It should be acknowledged, however, that there are very few Y dwarfs as late as this one, so judging observational trends at these late types is still difficult. Leggett et al. (2017) argue that this object's placement on the J - ch2 versus M_{ch2} diagram relative to model predictions suggest that it may be metal-rich.

8.2.10. WISE 0359–5401

This Y0 dwarf's *Spitzer* astrometric fit has a reduced χ^2 value of 2.512, and our *Spitzer* images show no complications. Opitz et al. (2016) used adaptive optics imaging to rule out a binary nature for this object, but only for a companion of equal magnitude more distant than 1.9 au from the primary. Given that this is one of the few Y dwarfs known, further astrometric monitoring might prove fruitful. Based on its location on the J - ch2 versus ch1 - ch2 plot and the trends shown by model atmosphere calculations, Leggett et al. (2017) argue that this object may be metal-poor.

8.2.11. WISE 0430+4633

In H - $W2$ and H - ch2 colors, this is an abnormally red T8, and it is faint in M_H for its type. The spectral type is based on single J -band spectrum (Mace et al. 2013a), but this type appears robust since these data have high S/N.

8.2.12. WISE 0458+6434AB

Despite being a known binary with $0''.5$ separation (Gelino et al. 2011), this object has a *Spitzer* astrometric fit that is remarkably good. We note, however, that the estimated period ~ 70 yr suggest very little orbital motion over the timespan of our *Spitzer* observations. The reduced χ^2 value of 0.190—the lowest of any of our targets—indicates either that our measurement uncertainties are inflated or that this is a statistical fluke. We note that this object is nonetheless clearly indicated as a binary because it is abnormally bright in M_{W1} and M_{ch1} for its ch1 - ch2 color. Resolved spectroscopy of the two

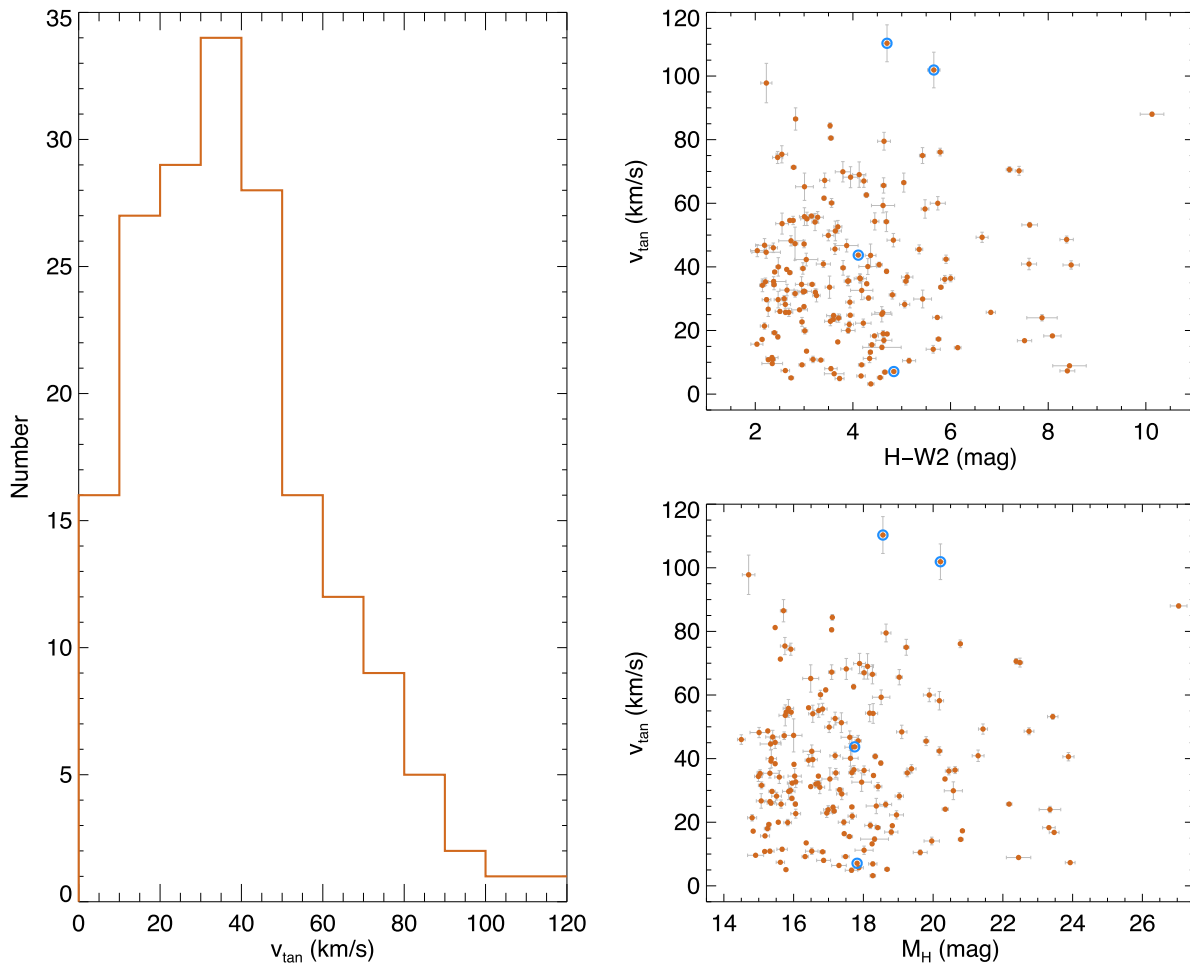


Figure 9. Distributions in number, color, and absolute magnitude for our tangential velocity measurements for objects in Table 7 that fall within 20 pc of the Sun ($\pi_{\text{abs}} \geq 50$ mas). On the left is the histogram of the v_{tan} values. At upper right is the distribution with respect to $H-W2$ color, and at bottom right is the distribution with respect to M_H . In these rightmost panels, spectroscopically identified subdwarfs (WISE 0833+0052, ULAS 1416+1348, GI 547B, and WISE 2005+5424) are circled in blue.

components gives spectral types of T8.5 and T9.5 (Burgasser et al. 2012).

8.2.13. UGPS 0521+3640

This T8.5 dwarf appears as an outlier on a number of diagrams. It is unusually blue for a T8.5 in both $W1-W2$ and $ch1-ch2$ color; it has a blue $W1-ch1$ color unlike that of most other late-T dwarfs and a $W2-ch2$ color significantly off zero; and it appears as an outlier on various absolute magnitude versus color diagrams. As noted in Table 2, the $W1$ photometry for this source is contaminated by the halo of a much brighter star. Moreover, the only extant *Spitzer* imaging comes from the shallow GLIMPSE survey (program 61070; PI: B. Whitney). This object is located at a Galactic latitude of only $b = -0^\circ 04$, so source confusion in the Galactic Plane is likely an issue in bands other than just $W1$.

8.2.14. WISE 0535-7500

This $\geq Y1$: dwarf may be abnormally bright in M_H , M_{W1} , and M_{W2} for its spectral type and $H-W2$ and $ch1-ch2$ colors. However, there are very few Y dwarfs known that are as late as this one, so judging observational trends is still difficult. The overluminosity may indicate an unresolved double, as was pointed out by Tinney et al. (2014). Opitz et al. (2016) used

high-resolution adaptive optics imaging in the near-infrared to rule out an equal-magnitude binary with a separation >1.9 au. This source is located in a dense field at the outskirts of the Large Magellanic Cloud, so contamination of some of the filter measurements is a possibility. The small motion of this source (125.2 ± 1.6 mas yr^{-1}) means that the object has not yet moved significantly in the *WISE* and *Spitzer* imaging since its discovery to reveal whether a background source may have complicated earlier photometry. Leggett et al. (2017) favor the binary hypothesis, although Tinney et al. (2014) suggests that an unusual atmosphere with thick clouds might provide an alternative explanation.

8.2.15. WISE 0540+4832

This T8.5 dwarf is abnormally dim in M_H for its $H-W2$ color. The spectral type is based on a J -band spectrum from Mace et al. (2013a), but it has high S/N. The reason for this peculiarity is unknown.

8.2.16. WISE 0614+3912

This T6 dwarf shows overluminosity in M_H (Figure 8), M_{W1} , M_{ch1} , M_{W2} , and M_{ch2} for its spectral type and for its $ch1-ch2$ and $H-W2$ colors. Keck/NIRC2 data obtained on 2013 January 17 UT (PI: M. Liu) and downloaded from the Keck

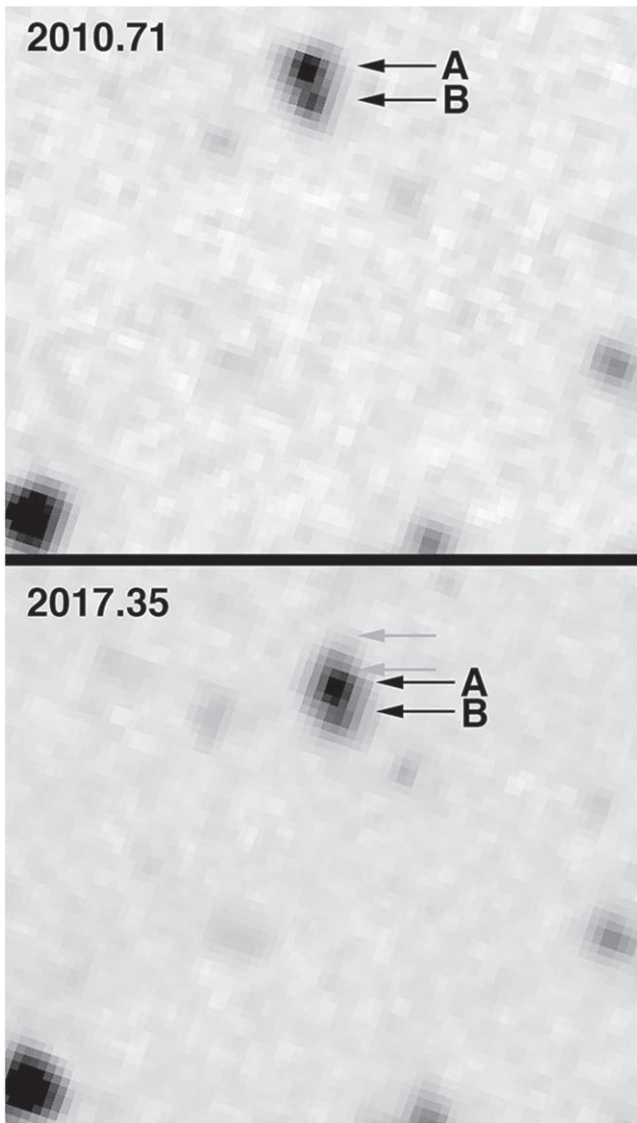


Figure 10. $33'' \times 38''$ section of the IRAC ch2 mosaics from AOR 40824064 (epoch 2010.71, top) and 61480192 (epoch 2017.35, bottom) illustrating the common proper motion and binary nature of the WISE 0226–0211AB system. In the bottom panel, the two gray arrows indicate the location of the binary at the earlier epoch.

Observatory Archive²³ (KOA) show this to be a binary with separation 195 mas and $\Delta H \approx 2.4$ mag. The KOA also includes Keck/NIRC2 imaging obtained on 2017 March 20 UT (PI: M. Liu) that confirms the pair to be a physical, co-moving system. Using the composite H -band magnitude from Table 2 and the parallax listed in Table 7, this gives magnitudes of $H \approx 16.5$ mag and $M_H \approx 15.2$ mag for the A component and $H \approx 18.9$ mag and $M_H \approx 17.6$ mag for the B component. These absolute magnitudes suggest individual spectral types of T6 and T8, based on the relation between spectral type and M_H in Table 8.

8.2.17. WISE 0647–6232

The *Spitzer* astrometric fit for this Y1 dwarf has a reduced χ^2 value of 2.309. Given that this is one of the coolest Y dwarfs

currently known, continued astrometric monitoring would be instructive.

8.2.18. WISE 0713–5854

This T9 dwarf is abnormally dim in M_H for its H – $W2$ color. The spectral type is based on a high-quality 0.95 – $1.65 \mu\text{m}$ spectrum from Tinney et al. (2018) and shows no peculiarities with respect to a standard T9 spectrum. The reason for this underluminosity is unknown.

8.2.19. WISE 0723+3403

Very little follow-up has been done on this T9: dwarf, whose plot of the *Spitzer* astrometric fit residuals (Figure 2) and reduced χ^2 value of 2.204 may be suggestive of a companion. The possible cyclical variation in the residuals is, however, based on only nine data points. We note, however, that there is other evidence for binarity given its overluminosity in M_H for its spectral type.

8.2.20. WISE 0734–7157

This Y0 dwarf has a *Spitzer* astrometric fit with a reduced χ^2 value of 3.049. As pointed out by Martin et al. (2018), this is likely one of the warmest Y0 dwarfs known, based on colors and its absolute J -band magnitude. Even though *HST*/WFC2 images at F105W and F125W show no evidence for binarity (Schneider et al. 2015), more detailed analysis into the possibility of its being a tighter double is warranted.

8.2.21. WISE 0751–7634

This T9 dwarf is underluminous in M_H , M_{W1} , and M_{ch1} for its ch1 – ch2 color. Another object that shows this same behavior is the sdT8 WISE 2005+5424, which might indicate that WISE 0751–7634 is also metal-poor. On the other hand, the three other T subdwarfs in the 20 pc sample do not share these traits. Leggett et al. (2017) also argue that a metal-poor explanation would better explain this object’s location on the J – ch2 versus ch1 – ch2 diagram based on atmospheric model trends.

8.2.22. WD 0806–661B

This object is a very cold companion to a white dwarf, and its spectral type is currently an educated guess. This object is sufficiently faint ($H = 25.29 \pm 0.14$ mag) that no spectrum has yet been acquired. Leggett et al. (2017) argue that the object may be metal-poor based on its location on the J – ch2 versus ch1 – ch2 diagram.

8.2.23. WISE 0811–8051

This T9.5: dwarf is one of the objects with a strangely blue $W1$ – ch1 color, which is almost certainly indicative of a corrupted measurement, most likely through contamination by a background source in $W1$. The object, however, does not distinguish itself as an outlier on any other plots.

8.2.24. WISE 0825+2805

This Y0.5 dwarf may be underluminous in M_H for its spectral type, but there are very few known Y dwarfs with types this late, so accurately gauging trends is difficult.

²³ See <https://koa.ipac.caltech.edu>.

Table 8
Coefficients for the Fitted Relations in Figures 4–7, and 14

x	y	c_0	c_1	c_2	c_3	Valid Range	rms ^a
(1)	(2)	(3)	(4)	(5)	(6)	(7)	(8)
SpT	$H-W2$	19.7444 ± 3.43923	-6.76528 ± 1.18653	0.806149 ± 0.132423	$-0.0264937 \pm 0.00477809$	$6 \leq \text{SpT} \leq 14$	0.51
SpT	$W1-W2$	-1.29441 ± 3.12275	0.812400 ± 1.08525	-0.0609403 ± 0.121097	$0.00290939 \pm 0.00431632$	$6 \leq \text{SpT} \leq 14$	0.39
SpT	$H-\text{ch2}$	21.3744 ± 3.46898	-7.36894 ± 1.19729	0.876955 ± 0.133654	$-0.0291438 \pm 0.00482272$	$6 \leq \text{SpT} \leq 14$	0.51
SpT	$\text{ch1}-\text{ch2}$	0.769877 ± 1.27185	-0.229115 ± 0.438774	0.0645336 ± 0.0489775	$-0.00245289 \pm 0.00176859$	$6 \leq \text{SpT} \leq 14$	0.19
SpT	M_H	36.9714 ± 4.51031	-8.66856 ± 1.55879	1.05122 ± 0.174229	$-0.0344809 \pm 0.00629456$	$6 \leq \text{SpT} \leq 14$	0.67
SpT	M_{W1}	13.8175 ± 4.00383	-0.276439 ± 1.39146	0.0844831 ± 0.155265	$-0.00124337 \pm 0.00553417$	$6 \leq \text{SpT} \leq 14$	0.50
SpT	M_{ch1}	17.0849 ± 2.61678	-1.78453 ± 0.902762	0.267153 ± 0.100769	$-0.00878279 \pm 0.00363881$	$6 \leq \text{SpT} \leq 14$	0.39
SpT	M_{W2}	16.3585 ± 1.95871	-1.59820 ± 0.675466	0.211474 ± 0.0753817	$-0.00682090 \pm 0.00272193$	$6 \leq \text{SpT} \leq 14$	0.29
SpT	M_{ch2}	16.3304 ± 1.89109	-1.56047 ± 0.652409	0.203183 ± 0.0728241	$-0.00635074 \pm 0.00262970$	$6 \leq \text{SpT} \leq 14$	0.28
SpT	M_{W3}	10.7315 ± 0.856890	0.0319455 ± 0.201454	0.0159426 ± 0.0115214	...	$6 \leq \text{SpT} \leq 14$	0.41
$\text{ch1}-\text{ch2}$	M_H	18.9087 ± 1.86865	-8.38783 ± 2.95532	5.32802 ± 1.47233	-0.667961 ± 0.231272	$0.9 \leq \text{ch1}-\text{ch2} \leq 3.7$	0.69
$\text{ch1}-\text{ch2}$	M_{W1}	11.9192 ± 1.04102	3.39859 ± 1.66875	-0.992429 ± 0.838003	0.258689 ± 0.131855	$0.9 \leq \text{ch1}-\text{ch2} \leq 3.7$	0.38
$\text{ch1}-\text{ch2}$	M_{ch1}	12.9757 ± 0.772255	0.381900 ± 1.22714	0.565159 ± 0.613775	-0.0221107 ± 0.0968472	$0.9 \leq \text{ch1}-\text{ch2} \leq 3.7$	0.30
$\text{ch1}-\text{ch2}$	M_{W2}	13.0115 ± 0.769282	-0.766700 ± 1.22244	0.684058 ± 0.611271	-0.0469633 ± 0.0964210	$0.9 \leq \text{ch1}-\text{ch2} \leq 3.7$	0.30
$\text{ch1}-\text{ch2}$	M_{ch2}	12.9611 ± 0.771287	-0.595238 ± 1.22560	0.554636 ± 0.613005	-0.0206577 ± 0.0967258	$0.9 \leq \text{ch1}-\text{ch2} \leq 3.7$	0.30
$\text{ch1}-\text{ch2}$	M_{W3}	10.9722 ± 0.333633	0.214034 ± 0.353496	0.194726 ± 0.0877464	...	$0.9 \leq \text{ch1}-\text{ch2} \leq 3.7$	0.32
$H-W2$	M_H	11.8526 ± 0.421256	1.51647 ± 0.275830	-0.0165129 ± 0.0551863	$0.00105023 \pm 0.00336992$	$2.0 \leq H-W2 \leq 10.5$	0.30
$H-W2$	M_{W1}	11.1276 ± 0.734096	2.22600 ± 0.493686	-0.283468 ± 0.100002	0.0177808 ± 0.00596974	$2.0 \leq H-W2 \leq 10.5$	0.44
$H-W2$	M_{ch1}	11.0097 ± 0.550438	1.75712 ± 0.360520	-0.191409 ± 0.0720912	0.0106380 ± 0.00439955	$2.0 \leq H-W2 \leq 10.5$	0.39
$H-W2$	M_{W2}	11.8484 ± 0.421319	0.520033 ± 0.275872	-0.0174249 ± 0.0551946	$0.00111599 \pm 0.00337042$	$2.0 \leq H-W2 \leq 10.5$	0.30
$H-W2$	M_{ch2}	11.7507 ± 0.423322	0.607561 ± 0.277263	-0.0398259 ± 0.0554427	$0.00273370 \pm 0.00338353$	$2.0 \leq H-W2 \leq 10.5$	0.30
$H-W2$	M_{W3}	10.7836 ± 0.276352	0.318603 ± 0.123162	$8.03680e-05 \pm 0.0117702$...	$2.0 \leq H-W2 \leq 10.5$	0.37
M_H	T_{eff}	11610.9 ± 1165.61	-1424.48 ± 177.512	61.2423 ± 8.88772	-0.892386 ± 0.146389	$14.5 \leq M_H \leq 27.0$	41
M_{W2}	T_{eff}	40669.7 ± 16715.8	-7272.51 ± 3476.93	440.398 ± 240.300	-8.96515 ± 5.51811	$12.5 \leq M_{W2} \leq 17.0$	70
M_{ch2}	T_{eff}	35476.5 ± 15647.4	-6198.65 ± 3231.62	366.839 ± 221.694	-7.29548 ± 5.05173	$12.5 \leq M_{\text{ch2}} \leq 17.2$	73
$H-W2$	T_{eff}	1821.84 ± 109.420	-490.635 ± 68.2886	59.1937 ± 12.9725	-2.55531 ± 0.760092	$2.0 \leq H-W2 \leq 10.5$	57
SpT	T_{eff}	2335.64 ± 139.416	-286.401 ± 31.8992	9.89240 ± 1.78104	...	$6 \leq \text{SpT} \leq 14$	68
$\text{ch1}-\text{ch2}$	T_{eff}	1603.55 ± 94.2015	-658.290 ± 94.2278	79.4503 ± 22.5429	...	$0.9 \leq \text{ch}-\text{ch2} \leq 3.6$	81

Notes. These are simple polynomial equations of the form

$$y = \sum_{i=0}^n c_i x^i.$$

For spectral types, SpT = 6 for T6, SpT = 7 for T7, ... SpT = 14 for Y4.

^a The units are magnitudes for all but the last six entries, whose units are K.

8.2.25. *WISE 0833+0052*

This is an (sd)T9 with a high v_{tan} value of $101.9 \pm 5.6 \text{ km s}^{-1}$. It does not appear as an outlier on any of our color or absolute magnitude plots.

8.2.26. *WISE 0855-0714*

This, the least luminous brown dwarf known, has a relatively high tangential velocity of $88.0 \pm 0.6 \text{ km s}^{-1}$. The only extant spectra of this object are low-resolution data at *L* and *M* bands from Skemer et al. (2016) and Morley et al. (2018). Fits to model atmospheres by Morley et al. (2018) indicate that the object may have slightly subsolar abundance.

8.2.27. *2MASS 0939-2448*

Our analysis indicates that this T8 dwarf is overluminous in M_H for its *H*–*W2* color (Figure 8) and overluminous in M_{W1} and M_{ch1} for its ch1–ch2 color. This has been a suspected binary for a decade: Burgasser et al. (2008b) noted its overluminosity early and favored a binary hypothesis and slightly subsolar metallicity, and Leggett et al. (2009) reached the same conclusion in analyzing the same data set. Line et al. (2017) note that the object appears to be single down to $0''.07$ resolution with near-infrared adaptive optics imaging, and their own analysis reaches the same conclusion of binarity and slightly subsolar abundance. For subsequent analyses, we consider this object to be an unresolved double.

8.2.28. *2MASS 1047+2124*

This T6.5 has a higher-than-average v_{tan} value of $86.5 \pm 3.5 \text{ km s}^{-1}$, but it appears to be a normal, solar metallicity T dwarf (Burgasser et al. 2002). Its claim to fame is that it is the first T dwarf with detected bursts in the radio (Williams & Berger 2015 and references therein).

8.2.29. *WISE 1050+5056*

The reduced χ^2 value for this T8 dwarf's *Spitzer* astrometric fit is 2.940, but this is based on only seven epochs of information. Additional astrometric measurements of this object are needed not only to further study the residuals but also to determine whether or not this object falls inside of or outside of the 20 pc sample, as our current fit gives $\pi_{\text{abs}} = 49.7 \pm 5.0 \text{ mas}$. For subsequent analyses, this object is assumed to fall beyond 20 pc.

8.2.30. *2MASS 1114-2618*

This T7.5 dwarf has a relatively high v_{tan} value of $86.5 \pm 3.5 \text{ km s}^{-1}$. Both Burgasser et al. (2006b) and Leggett et al. (2007) agree that this object's near-infrared spectrum is best explained by slightly subsolar metallicity ($[M/H] \approx -0.3$).

8.2.31. *WISE 1141-3326*

This Y0 dwarf is anomalously blue in ch1–ch2 color for its type, and is too faint in both M_{W1} and M_{ch1} for its ch1–ch2 color. It is quite likely that these anomalies can be attributed to confusion at early epochs by a background galaxy (see Figure 2 of Tinney et al. 2018). A new round of photometry, now that the Y dwarf has moved clear of the background source, would be informative.

8.2.32. *ULAS 1152+1134*

The fit to this object's *Spitzer* astrometry has a reduced χ^2 value of 2.551, but this is based on only six data points. Additional astrometric measurements of this object are needed not only to further study the residuals but also to determine whether or not this object falls within the 20 pc sample. Our current fit gives $\pi_{\text{abs}} = 49.7 \pm 5.1 \text{ mas}$. For subsequent analyses, this object is assumed to fall beyond 20 pc.

8.2.33. *WISE 1217+1626AB*

This T9 dwarf is overluminous in M_{W1} and M_{ch1} for its ch1–ch2 color and clearly sits above the standard sequence in the M_H versus *H*–*W2* plot (Figure 8). This object was found to be a $0''.8$ binary with component spectral types of T9 and Y0 by Liu et al. (2012). Our *Spitzer* astrometric fit for this object has a reduced χ^2 value of 5.776, which also strongly hints at its binary nature.

8.2.34. *2MASS 1225-2739*

This T6 dwarf is overluminous in all measured bands for its spectral type and colors. Burgasser et al. (2003b) showed that the source was a binary with separation of $0''.28$ on *HST*/WFPC2 images at F814W and F1042M. Using the parallax of the system and photometry from the *HST* images, Vrba et al. (2004) estimate spectral types of T6: and T8: for the pair. This was later revised with additional photometric data to T5.5 and T8 by Dupuy & Liu (2012).

8.2.35. *2MASS 1231+0847*

This T5.5 dwarf has a relatively high V_{tan} value of $97.8 \pm 6.3 \text{ km s}^{-1}$. Burgasser et al. (2004) noted that this object has broad KI lines, indicating that it is either rapidly rotating or has a higher photospheric pressure, the latter of which could point to a higher surface gravity that is the consequence of somewhat subsolar metallicity. However, this object, which was originally given a spectral type of T6 by Burgasser et al. (2004), was revised to T5.5 by Burgasser et al. (2006b) and thus falls outside of the spectral type sample we consider in further analyses.

8.2.36. *WISE 1322-2340*

This is an abnormally blue T8 in both *H*–*W2* and *H*–ch2 color, but it is not noted as peculiar on any other plots. Gelino et al. (2011) did not find any evidence for binarity using adaptive optics near-infrared imaging, ruling out any companions with $\Delta H < 4 \text{ mag}$ outside of $0''.2$. No peculiarities were noted in the $0.8\text{--}2.5 \mu\text{m}$ spectrum by Kirkpatrick et al. (2011).

8.2.37. *WISE 1405+5534*

This object is an outlier in M_{W1} for its type, but it is known to have an unusual spectrum for an early-Y dwarf. Its *H*-band emission peak is shifted to longer wavelengths by $\sim 60 \text{ \AA}$ relative to other late-T and early-Y dwarfs (Cushing et al. 2011).

8.2.38. *ULAS 1416+1348*

This is the reddest T7.5 dwarf in *H*–*W2* and *H*–ch2 color. It is also overluminous in M_{W1} and M_{ch1} for its ch1–ch2 color and in M_H for its *H*–*W2* color. This object is a common-proper-motion

companion to SDSS J141624.08+134826.7, which is often regarded as an sdL7 or d/sdL7 (Kirkpatrick et al. 2011; Burningham et al. 2010a). ULAS 1416+1348 has somewhat conflicting spectral types of T7.5 (blue), T7.5 pec, and sdT7.5 (Burgasser et al. 2010b; Burningham et al. 2010a; Kirkpatrick et al. 2011), all of which highlight its unusual spectrum. Given that its peculiarities and those of its primary are often attributed to subsolar metallicity, a designation of sdT7.5 seems appropriate. Whereas the three other late-T subdwarfs known (WISE 0833+0052, Gl 547B, and WISE 2005+5424) show no overluminosity relative to normal dwarfs, ULAS 1416+1348 very clearly does. We therefore conclude that this object is a close, unresolved double and consider it as such in subsequent analyses.

8.2.39. WISE 1501–4004

The *Spitzer* astrometric fit for this T6 dwarf has a reduced χ^2 value of 2.493, but that is based on only seven epochs of data. Continued monitoring is indicated to see if this may indicate the presence of a lower-mass companion. The object does not, however, appear as an outlier in any of our color/magnitude/type plots.

8.2.40. WISE 1523+3125

This T6.5pec dwarf is the reddest T6.5 in H – $W2$ and H – $ch2$ colors. It is also underluminous in M_H for its spectral type. Mace et al. (2013a) showed that the J -band flux best matched that of a T7 standard whereas the H -band flux best matched that of a T6 standard, which is similar to the spectral behavior of 2MASS 0937+2931, which may be slightly metal-poor itself (Burgasser et al. 2002). However, this same spectral behavior is not seen in the T subdwarfs such as Gl 547B, and 2MASS 0937+2931 does not stand out as an outlier on any of our plots. The cause for the peculiar spectra and photometry of WISE 1523+3125 is unknown.

8.2.41. WISE 1541–2250

This Y1 dwarf is another of the objects with a strangely blue $W1$ – $ch1$ color. This is almost certainly due to an erroneous $W1$ measurement (see discussion in Kirkpatrick et al. 2012) caused by its passage near a brighter background source.

8.2.42. WISE 1542+2230

The reduced χ^2 value for this T9.5 object’s *Spitzer* astrometric fit is 2.181. The only high-resolution imaging reported for this object is from *HST*/WFC2 by Schneider et al. (2015) at F105W, F125W, and F140W. No evidence of a companion is seen. Continued monitoring is suggested.

8.2.43. 2MASS 1553+1532

This T7 dwarf is overluminous in M_{W2} and M_{ch2} for its spectral type. This object was confirmed as a close binary by Burgasser et al. (2002) using *HST*/NICMOS imaging. Using available photometry and combined-light spectroscopy, Dupuy & Liu (2012) estimate spectral types for the individual components of T6.5 and T7.5.

8.2.44. WISE 1627+3255

This T6 dwarf is consistently overluminous in all bands for its colors. It is a dramatic outlier, for example, on the M_H versus

H – $W2$ plot of Figure 8. Gelino et al. (2011) found no evidence for a companion down to $\Delta H \approx 5$ mag for separations larger than $0''.2$. Because of the strong evidence favoring binarity, we consider this object to be a tight, unresolved double in subsequent analyses.

8.2.45. WISE 1804+3117

This T9.5: dwarf is overluminous in M_H , M_{W2} , and M_{ch2} for its spectral type. Because the type is uncertain, this discrepancy would disappear if a slightly earlier spectral type were indicated. We note that the object is not overluminous on the absolute magnitude versus color plots, so we will assume this object is single for subsequent analyses.

8.2.46. WISE 1813+2835

This T8 is unusually blue in both $W1$ – $W2$ and $W1$ – $ch1$ color. This indicates that the $W1$ measurement from WISE is contaminated (made too bright) by a background object. Indeed, recent imaging from *NEOWISE* shows the T dwarf has now moved away from a bluer source behind it. Mace et al. (2013a) do not note anything peculiar about the spectrum.

8.2.47. WISE 1828+2650

This $\geq Y2$ dwarf is overluminous for its spectral type in M_{W2} and M_{ch2} and is also overluminous in M_H for its H – $W2$ color (Figure 8). On the M_{W2} versus H – $W2$ plot, it falls ~ 1 mag above the trend, and in the M_{ch1} versus H – $W2$ plot, it falls at least 1 mag above the trend. However, WISE 1828+2650 falls in line with other Y dwarfs on the plot of M_H versus $ch1$ – $ch2$. This Y dwarf has been an object of much speculation since its broadband colors cannot be fit by any of the current suite of models (e.g., Beichman et al. 2013). Leggett et al. (2017) speculate that the object may be an equal-magnitude binary (which explains only 0.75 mag worth of overluminosity) as well as having a subsolar metallicity ($[M/H] \approx -0.5$), the latter based on model atmosphere trends seen in the M_{ch2} versus J – $ch2$ diagram. Inexplicably, though, their best fitting atmospheric model suggests a young system (~ 1.5 Gyr). Such a young age is hard to reconcile with the subsolar metallicity, so the more likely explanation is that the current suite of atmospheric models simply fails to contain the physics necessary to explain this object’s near-infrared spectrum and broadband colors.

8.2.48. WISE 1928+2356

This T6 dwarf lies near the Galactic Plane at $l = 58^\circ 3$ and $b = +3^\circ 1$, and our *Spitzer* astrometric fit has a reduced χ^2 value of 2.347. The motion over our 5.2 yr of *Spitzer* observations shows that there are no background sources that might be confusing the astrometric measurements. Continued monitoring is suggested to test for the presence of an unseen companion.

8.2.49. WISE 2005+5424

This object has a relatively high v_{\tan} value of 110.3 ± 5.8 km s $^{-1}$, and appears as an outlier on some of our other plots. This is a known sdT8 (Mace et al. 2013b, 2018) and is a distant, common-proper-motion companion to the Wolf 1130 (Gl 781) system.

Table 9
Mass Functions Considered for Masses $<0.1M_{\odot}$

Name	Functional Form	Parameters Used	Notation in Figures
(1)	(2)	(3)	(4)
Power law	$CM^{-\alpha}$	$\alpha = -1.0$	A
...	...	$\alpha = -0.5$	B
...	...	$\alpha = 0.0$	C
...	...	$\alpha = 0.5$	D
...	...	$\alpha = 1.0$	E
...	...	$\alpha = 1.5$	F
Log-normal	$Ce^{-(\ln(M)-\mu)^2/2\sigma^2}$	$\mu = \ln(0.079), \sigma = 0.69 \ln(10)$	G
...	...	$\mu = \ln(0.10), \sigma = 0.627 \ln(10)$	H
...	...	$\mu = \ln(0.22), \sigma = 0.57 \ln(10)$	I
Bi-partite power law	$C\left(\frac{M}{0.07}\right)^{-\alpha_1}$ for $M > 0.07M_{\odot}$, $\frac{C}{3}\left(\frac{M}{0.07}\right)^{-\alpha_2}$ for $M < 0.15M_{\odot}$	$\alpha_1 = 1.3, \alpha_2 = 0.3$	J
...	...	$\alpha_1 = 1.0, \alpha_2 = 0.7$	K
...	...	$\alpha_1 = 1.6, \alpha_2 = -0.1$	L

8.2.50. ULAS 2146–0010

This object is also known as Wolf 940B, so the near-solar metallicity of the primary star can be assumed to apply to the companion as well (Burningham et al. 2009; Leggett et al. 2010b). Surprisingly, this T8 dwarf is an outlier on many of our plots. Because of the high proper motion of this late-T dwarf, we now know that during the time of its *Spitzer*/IRAC observations in 2008 (see the *Spitzer* Heritage Archive), which represents the only ch1 observation that exists, it was contaminated by a background object now clearly visible in later *NEOWISE* images at these same wavelengths (see *NEOWISE* data at IRSA). Thus, we conclude that the odd placement of this object on many of our diagrams is simply due to contaminated measurements.

8.2.51. WISE 2209+2711

This is the faintest Y0 dwarf in M_H , M_{ch1} , M_{ch2} , and M_{W2} . Its spectral type is uncertain, though. Schneider et al. (2015) suggests that the noisy *HST*/WFC3 spectrum on which the type is based may be, despite its poor signal, hinting at sharper *Y*-, *J*-, and *H*-band peaks that point to a type closer to Y1. A later spectral type would solve the discrepancy.

8.2.52. WISE 2212–6931

The reduced χ^2 value for the *Spitzer* astrometric fit of this T9 dwarf is 2.422. High-resolution *HST*/WFC3 imaging at F105W and F125W by Schneider et al. (2015) shows no evidence of binarity. However, this object also shows an abnormally blue *W1*–ch1 color. This suggests possible contamination by a background object in the *W1* photometry, which later *NEOWISE* imaging strongly suggests. This contamination at *W1* should not, however, affect the ch2 astrometry, so continued monitoring is still warranted.

8.2.53. WISE 2226+0440

This T8 is abnormally blue in *H*–*W2* and *H*–ch2 color and overluminous in M_H for its type. It does not, however, appear overluminous in M_H for its *H*–*W2* color. We consider this to be a single object.

8.2.54. WISE 2344+1034

The reduced χ^2 value for this T9 dwarf’s *Spitzer* astrometric fit is 3.157. No high-resolution imaging has been published for this source. Astrometric monitoring will continue in an attempt to determine whether the poor fit is due to an unseen companion.

8.3. Fits to the Trends

With the examination of the outliers complete, we fit polynomial relations to trends seen in Figures 4–7 using a standard least-squares approach. Removed from consideration from the fits, and shown by the circled points in each of the four figures, are known binaries (WISE 0146+4324AB, WISE 0226–0211AB, WISE 0458+6434AB, WISE 1217+1626AB, 2MASS 1225–2739AB, and 2MASS 1553+1532AB), objects with strong indication of binarity even if this is not yet proven (WISE 0309–5016, WISE 0614+3912, 2MASS 0939–2448, ULAS 1416+1348, and WISE 1627+3255), subdwarfs (WISE 0833+0052, Gl 547B, and WISE 2005+5424), and objects proven to have poor photometry in any band (UGPS 0521+3640, WISE 0535–7500, WISE 0811–8051, WISE 1141–3326, WISE 1541–2250, WISE 1813+2835, ULAS 2146–0010, WISE 2212–6931). The coefficients for the resulting fitted polynomials are given in Table 8.

9. Analysis of the Underlying Mass Function

9.1. Transforming from the Theoretical to the Observational Plane

Determining the form of the stellar mass function enlightens us about the physical mechanisms underlying star formation and the creation efficiency for objects of all masses. For hydrogen-burning stars in a well-defined observational sample, this is a relatively straightforward measurement: the spectral type or broadband color of each star determines its location on the HR diagram’s main sequence, which in turn determines its mass.

The lowest-mass end of the mass function, which is comprised solely of brown dwarfs, is, however, much more difficult to measure. Unlike stars, brown dwarfs lack a simple relationship

between spectral type/color and mass because they never settle onto a main sequence. Instead, they cool with time, so mass cannot be deduced without some determination of the age, which is a notoriously difficult measurement for field objects.

For brown dwarfs, an alternate method is to assume various functional forms of the mass function and to draw objects from those distributions according to an assumed rate of star formation. Using an assigned birth time, each brown dwarf is allowed to cool to the present time as predicted from an assumed suite of evolutionary models. Then the distribution of these objects as a function of color, spectral type, or other quantity is compared to the empirical distribution.

Burgasser (2004) undertook this kind of analysis to produce predicted empirical distributions assuming several different power-law mass functions and a single version of the log-normal function favored by Chabrier (2001). For evolutionary models, Burgasser (2004) employed models by Burrows et al. (1997) and the new (at the time) models of Baraffe et al. (2003). Here we attempt to expand that formalism and to produce empirical distributions over a wider range of assumed mass function models. We also include a newer suite of evolutionary models from Saumon & Marley (2008) that better predicts behavior across the L/T transition.

9.1.1. Formalism

Each assumed mass function, once properly normalized, can be thought of as a probability distribution function (PDF) describing the likelihood of finding a randomly selected object of mass M (in units of M_\odot). Integrating the area under this PDF gives the cumulative distribution function (CDF), which gives the probability of a randomly selected object having a mass less than or equal to M . In order to sample from this distribution, one can use the inverse transform sampling method, which is done by switching the dependent and independent variables in the CDF and re-solving for the dependent variable, thus giving the inverse CDF. Random seeds can then be generated from a uniform distribution over the interval $[0, 1]$ and passed through the inverse CDF to produce samples of objects whose mass distribution is described by the assumed mass function.

As an example, consider a power-law mass function with an exponent of α :

$$f(M) = \text{PDF} = CM^{-\alpha},$$

where C is a constant and M is the mass. If we wish to sample this distribution over the range of masses $m_1 < M < m_2$, then the CDF would be

$$\begin{aligned} \text{CDF} &= C \int_{m_1}^{m_2} M^{-\alpha} dM \\ &= \begin{cases} \frac{M^{1-\alpha} - m_1^{1-\alpha}}{m_2^{1-\alpha} - m_1^{1-\alpha}}, & \text{for } \alpha \neq 1 \\ \frac{\ln(M) - \ln(m_1)}{\ln(m_2) - \ln(m_1)}, & \text{for } \alpha = 1. \end{cases} \end{aligned}$$

Note that at the low-mass limit of $M = m_1$ we have $\text{CDF} = 0$, and at the high-mass limit of $M = m_2$ we have $\text{CDF} = 1$. The

inverse CDF would then be

$$\text{CDF}^{-1} = \begin{cases} [x(m_2^{1-\alpha} - m_1^{1-\alpha}) + m_1^{1-\alpha}]^{\frac{1}{1-\alpha}}, & \text{for } \alpha \neq 1 \\ e^{x[\ln(m_2) - \ln(m_1)] + \ln(m_1)}, & \text{for } \alpha = 1. \end{cases}$$

Note that at $x = 0$ we have $\text{CDF}^{-1} = m_1$ and at $x = 1$ we have $\text{CDF}^{-1} = m_2$.

9.1.2. Functional Forms

We considered several different forms of the mass function, as summarized in Table 9: (1) a single power law, (2) a log-normal distribution, and (3) a bi-partite power law:

1. For the single power law, we ran simulations with six different values of the exponent ranging from $\alpha = -1.0$ to $\alpha = 1.5$ in half-integer increments. This encompasses the range of α values generally discussed in the literature for the substellar mass function (see Figure 2 of Bastian et al. 2010).
2. For the log-normal function shown in Table 9, we chose three different values of the mean, μ , and standard deviation, σ , corresponding to published values in the literature²⁴: $(\mu, \sigma) = (\ln(0.079), 0.69 \ln(10))$ from Chabrier (2003b), $(\ln(0.10), 0.627 \ln(10))$ from Chabrier (2001), and $(\ln(0.22), 0.57 \ln(10))$ from Chabrier (2003a). The first two of these are applicable to the single-object mass function, and the third is applicable to the system mass function (which includes unresolved binaries).
3. For the bi-partite power law, we took the functional form shown in Table 9, taken from Equation (55) of Kroupa et al. (2013). The two power laws overlap in the mass range $0.07M_\odot < M < 0.15M_\odot$, with the high-mass component having $\alpha_1 = 1.3 \pm 0.3$ and the low-mass component having $\alpha_2 = 0.3 \pm 0.4$. We have taken three versions of this bi-partite law, the first of which is taken at the canonical values of α_1 and α_2 . We have also considered two other versions—one in which the contribution from the lower-mass portion is increased (to $\alpha_2 - \sigma_{\alpha_2}$) while the higher-mass portion is decreased (to $\alpha_1 + \sigma_{\alpha_1}$), and another for which we did the opposite (using $\alpha_1 - \sigma_{\alpha_1}$ and $\alpha_2 + \sigma_{\alpha_2}$)—to account for the full range of variation within the quoted α uncertainties.

9.1.3. Evolutionary Models

Objects with a variety of birth times are randomly selected from the above mass functions and allowed to evolve to the present day. This latter step requires that we use evolutionary models to predict the object's current effective temperature and luminosity. For each form of the mass function, we considered two different sets of evolutionary models, both of which are for objects of solar metallicity. The first is the set of COND models from Baraffe et al. (2003), which neglect dust opacity and are most applicable in the spectral ranges mid-M and mid- to late-T, where atmospheres are believed to be largely cloud-free. The second set is from Saumon & Marley (2008)—specifically, their hybrid suite of models. These hybrid models should be applicable to our full range of T_{eff} because they include clouds for objects warmer than the L/T transition region (a zone in

²⁴ We quote these values for the natural (base e) logarithmic version of the log-normal function that the R software environment uses.

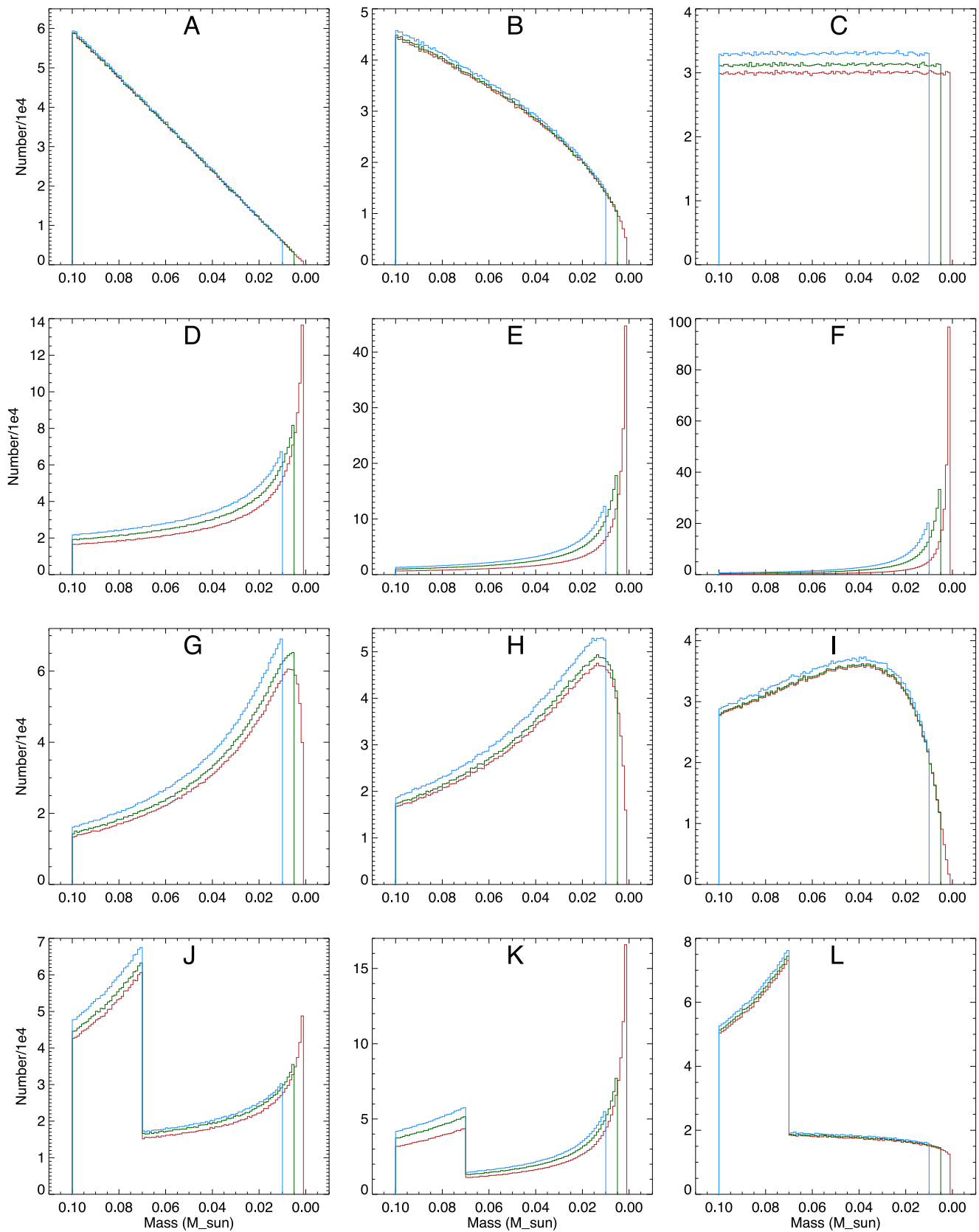


Figure 11. Simulated mass functions. Each panel is labeled with a capital letter that refers back to the code in column 4 of Table 9 and specifies the functional form assumed. Each panel shows the results of three different assumed values of the low-mass cutoff: $10 M_{\text{Jup}}$ (blue), $5 M_{\text{Jup}}$ (green), and $1 M_{\text{Jup}}$ (red). Bins are $0.001 M_{\odot}$ wide.

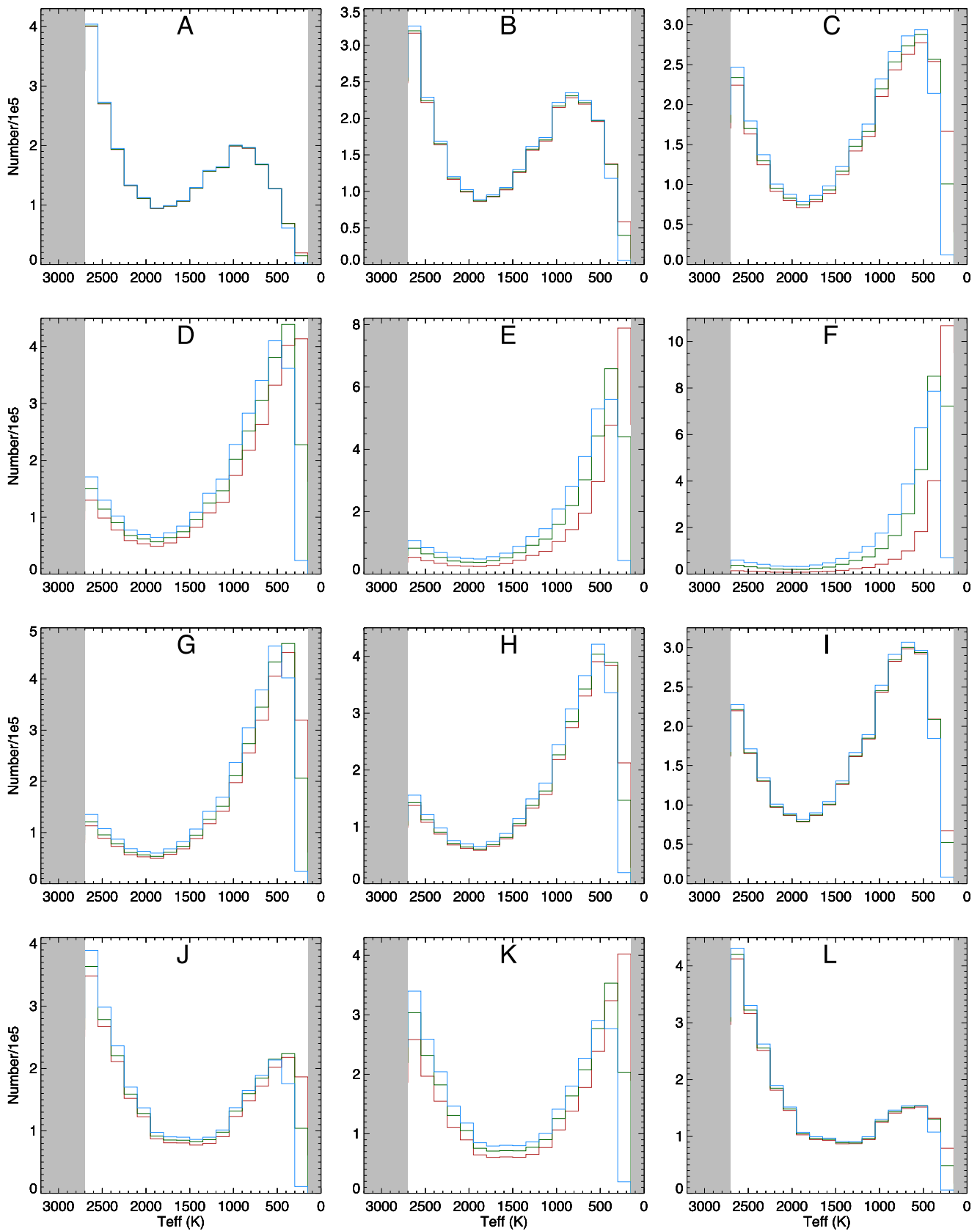


Figure 12. Distribution of our simulated sample in T_{eff} for each of the mass function and low-mass cutoff assumptions shown in Figure 11 and passed through the evolutionary models of Baraffe et al. (2003). Color coding is the same as in Figure 11. Gray zones mark areas in T_{eff} that are not covered by the Baraffe et al. (2003) models. Bins are 150 K wide.

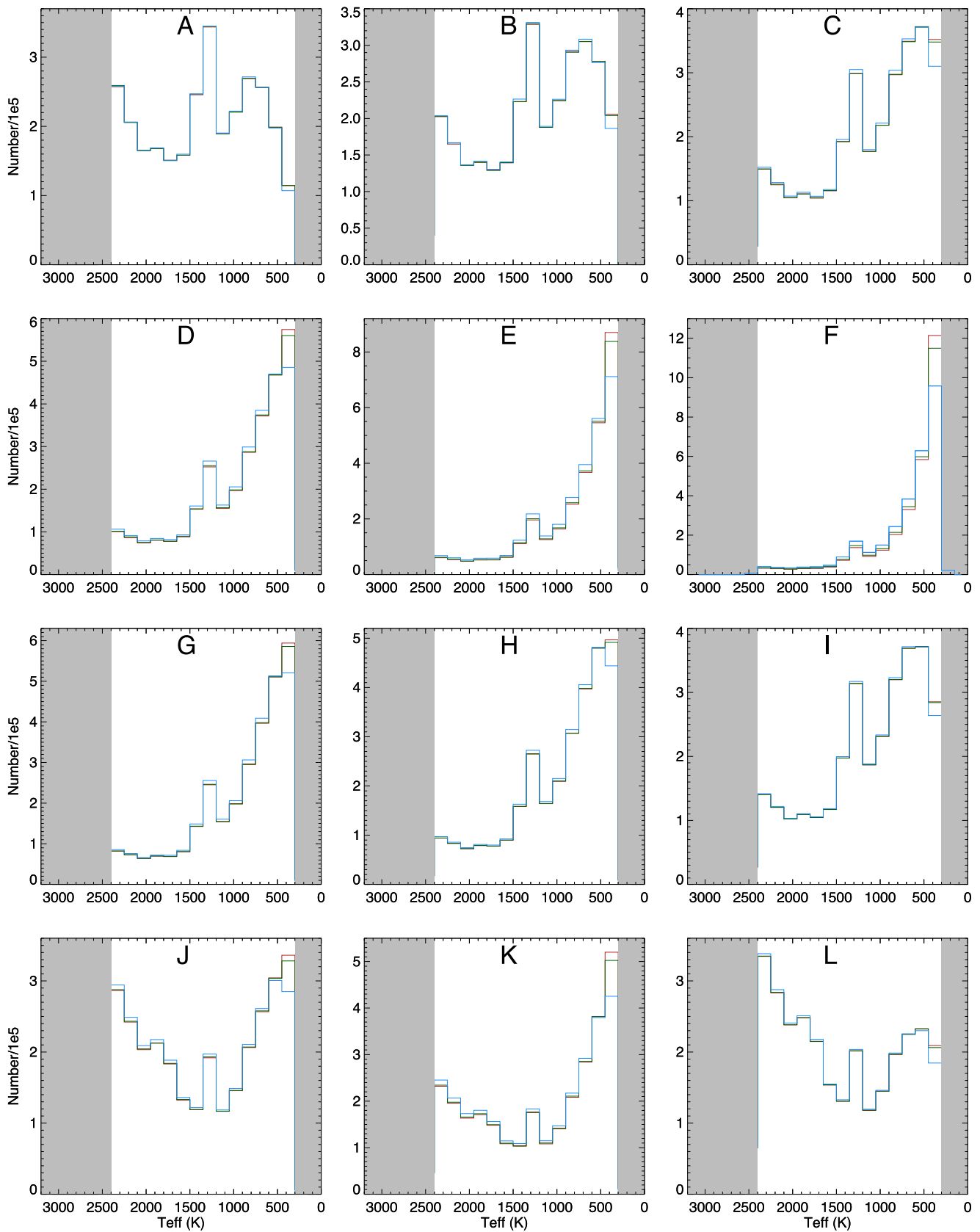


Figure 13. Distribution of our simulated sample in T_{eff} for each of the mass function and low-mass cutoff assumptions shown in Figure 11 and passed through the evolutionary models of Saumon & Marley (2008). Color coding is the same as in Figure 11. Gray zones mark areas in T_{eff} that are not covered by the Saumon & Marley (2008) models. Bins are 150 K wide.

which rapid cloud growth and subsequent clearing are believed to occur; Burrows et al. 2006) and are cloudless for temperatures cooler than this.

Both sets of models have restrictions that need to be taken into account when drawing object samples. The model grids of Baraffe et al. (2003) are presented at five different ages (0.1, 0.5, 1, 5, and 10 Gyr) and fully sample the range $125 \text{ K} \lesssim T_{\text{eff}} \lesssim 2800 \text{ K}$, corresponding roughly to masses $0.01 M_{\odot} < M < 0.10 M_{\odot}$. Objects younger than 100 Myr were not included. Values of T_{eff} were obtained through linear interpolation of grid points.

The models of Saumon & Marley (2008) are presented at twenty-six different ages covering $3 \text{ Myr} < \text{age} < 10 \text{ Gyr}$ and cover the temperature range $300 \text{ K} \lesssim T_{\text{eff}} \lesssim 2400 \text{ K}$ for objects with masses $0.002 M_{\odot} < M < 0.085 M_{\odot}$. As with the Baraffe models, values of T_{eff} for our sample objects were obtained through linear interpolation of grid points.

9.1.4. Birthrates

Both Allen et al. (2005) and Burgasser et al. (2004) have studied the effect of differing birthrates on the shape of the resulting luminosity function. Allen et al. (2005) noted that most empirically derived birthrate distributions for field stars are roughly consistent with a constant formation rate over the past 10 Gyr. They found that differences in the assumed birthrate produced small variations in the shape of the resulting luminosity function, but these were much smaller than the effects produced by the assumed functional form of the mass function itself. Burgasser et al. (2004) expanded this discussion to more extreme birthrate scenarios and found that the resulting empirical luminosity function in the T dwarf regime is relatively insensitive to the assumed star formation rate, whereas the L dwarf regime is not. Nonetheless, we will simply assume constant star formation over the last 10 Gyr and leave analysis of other star formation rates to a future study.

9.1.5. Sampling Method

Using the above assumptions, one of us (AJC) wrote code in the *R* software environment²⁵ to produce simulated versions of the T_{eff} distributions. A random number generator was used to draw 3×10^6 values in the interval $[0, 1]$, and each was assigned an age depending upon the order of its selection. The n th draw was given an age of $n \times 3333.\bar{3} \text{ yr}$ so that the full sample covered an age spread of 0–10 Gyr uniformly. Its random seed value in the $[0, 1]$ interval was passed through the inverse CDF to provide a mass. This mass and age were then compared to the evolutionary model grids to determine the present-day effective temperature of the object.

9.2. Simulation Results

Results are shown in the following figures. Figure 11 shows the 12 forms of the mass function from Table 9. Overplotted on each panel are three different versions, one for each of three different low-mass cutoffs assumed: $10 M_{\text{Jup}}$, $5 M_{\text{Jup}}$, and $1 M_{\text{Jup}}$. Subsequent figures show the resulting T_{eff} histograms for each of these mass functions when paired with evolutionary code of Baraffe et al. (2003) in Figure 12 or Saumon & Marley (2008) in Figure 13.

The simulations in Figure 12 probe sufficiently low masses that the effects of varying the low-mass cutoff can be studied.

This has already been explored by Burgasser (2004), but we reiterate here that the lowest T_{eff} bins, particularly the one from 150 to 300 K, are very sensitive to the mass cutoff. In Model D (power law of $\alpha = 0.5$), for example, the space densities vary wildly between the 450–300 K and 150–300 K bins depending upon the cutoff mass. From the 450–300 K bin to the 150–300 K bin, the space density drops by $\sim 16\times$ for the $10 M_{\text{Jup}}$ cutoff, by $\sim 2\times$ for the $5 M_{\text{Jup}}$ cutoff, and is roughly identical for the $1 M_{\text{Jup}}$ cutoff. This is a consequence of the fact that for the $10 M_{\text{Jup}}$ cutoff, there has not been enough time in the 10 Gyr allotted for any but the lowest mass, oldest objects to cool to these temperatures. For lower-mass cutoffs, there are larger populations of low-mass objects capable of cooling to these values. Measuring the space density of these coldest objects thus provides a powerful tool in determining the cutoff mass itself.

Note also that the T_{eff} simulations using the Baraffe et al. (2003) models are generally smooth whereas those from Saumon & Marley (2008) show substructure along the range of T_{eff} . Namely, all simulations show a bump in the number counts in the 1200–1350 K bin. This was noted in Figure 13 of Saumon & Marley (2008) and is a consequence of the hybrid models in which the cooling timescale increases from 1400 K to 1200 K, at the transition between L and T dwarfs. This is the T_{eff} zone at which objects are transitioning from cloudy to clear photospheres. It is worth noting that the 1050–1500 K range over which this overdensity is seen corresponds to $\sim L6$ to $\sim T6$, a wide spectral type range that itself reflects the breadth of change in spectral morphology as the clouds clear.

9.3. Comparison to Empirical Data

9.3.1. Late-T and Y Dwarfs

To compare the output from our mass function simulations to our observational sample, we need to determine the effective temperature for each object within the 20 pc volume. Using the subset of objects from Table 7 that have effective temperature estimates in the literature (Table 10), we can estimate T_{eff} values for the entire set.

As the division in Table 10 shows, three main methods have been used in the determinations. Method 1 is forward modeling, which has been the traditional method for determining temperatures. In this method, a grid of model atmospheres is calculated using a complete theoretical description wherein a few vital physical parameters are varied to simulate those likely to be encountered in real atmospheres. Observational spectrophotometric data are then compared to the grid to find the model that best reproduces the observations. Method 2 is inverse modeling, which is also referred to as retrieval analysis. This method strives to deduce physical parameters directly from the data. As explained in Line et al. (2014), this method uses fewer assumptions than forward modeling and has the potential of discerning physical processes (e.g., non-equilibrium chemistry) missing from the forward models, or revealing poor assumptions (e.g., solar elemental abundances) made in those models. Method 3 uses the Stefan–Boltzmann Law to compute the value of T_{eff} directly. In this method, the absolute bolometric luminosity—computed using a measured parallax and spectrophotometry over a wide range of wavelengths—is used with an assumed radius ($\sim 1 R_{\text{Jup}}$ for old brown dwarfs) to determine the temperature directly from $T_{\text{eff}} = (L/(4\pi R^2\sigma))^{0.25}$.

²⁵ See <https://www.r-project.org/>.

Table 10
Effective Temperature Determinations for Objects from Table 7

Name	Spec. Type	T_{eff} (K) from Forward Modeling (Reference)	T_{eff} (K) from Retrieval Analysis (Reference)	T_{eff} (K) from Stefan–Boltzmann (Reference)	Adopted T_{eff} (K)
(1)	(2)	(3)	(4)	(5)	(6)
ULAS 0034–0052	T8.5	625, 540 (5, 10)	583
2MASS 0034+0523	T6.5	840 (11)	...	899 (4)	870
Gl 27B	T8	...	719 (3)	...	719
2MASS 0050–3322	T7	980 (11)	815 (3)	836 (4)	836
CFBDS 0059–0114	T8.5	573, 520 (5, 10)	547
WISE 0146+4234AB	Y0	570 (7)	570
WISE 0146+4234A	T9	333 (16)	330
WISE 0146+4234B	Y0	415, 320 (2, 16)	368
WISE 0148–7202	T9.5	600 (5)	600
ULAS 0150+1359	T7.5	775 (6)	775
2MASS 0243–2453	T6	1070 (11)	...	972 (4)	1021
WISE 0254+0223	T8	690 (5)	...	621 (4)	656
WISE 0304–2705	Y0pec	475 (2)	475
WISE 0313+7807	T8.5	662 (7)	662
WISE 0325–5044	T8	575 (1)	575
WISE 0335+4310	T9	525, 605 (1, 7)	565
2MASS 0348–6022	T7	950 (8)	950
WISE 0350–5658	Y1	325, 325, 253 (1, 2, 5)	325
WISE 0359–5401	Y0	400, 435, 268 (1, 2, 5)	400
WISE 0404–6420	T9	575 (1)	575
WISE 0410+1502	Y0	400, 425, 415, 491 (1, 2, 5, 7)	420
2MASS 0415–0935	T8	704, 750 (5, 11)	680 (3)	677 (4)	692
WISE 0458+6434A	T8.5	765 (5)	765
WISE 0458+6434B	T9.5	615 (5)	615
UGPS 0521+3640	T8.5	625 (9)	625
WISE 0535–7500	$\geq Y1$:	475, 375, 595 (1, 2, 5)	475
Gl 229B	T7pec	927 (4)	927
WISE 0647–6232	Y1	375, 335 (1, 2)	355
WISE 0713–2917	Y0	450, 513 (2, 7)	482
UGPS 0722–0540	T9	521 (5)	...	569 (4)	545
2MASS 0727+1710	T7	920 (11)	807 (3)	845 (4)	845
2MASS 0729–3954	T8pec	755 (5)	737 (3)	752 (4)	752
WISE 0734–7157	Y0	450, 450 (1, 2)	450
WD 0806B	$[\geq Y3]$	338, 353 (2, 5)	346
DENIS 0817–6155	T6	1004 (4)	1004
WISE 0825+2805	Y0.5	400, 325 (1, 2)	363
WISE 0836–1859	T8pec	765 (7)	765
WISE 0855–0714	$[\geq Y4]$	250 (2)	250
ULAS 0901–0306	T7.5	670 (10)	670
2MASS 0937+2931	T6pec	810 (11)	...	881 (4)	846
2MASS 0939–2448	T8	709 (5)	611 (3)	686 (4)	686
WISE 0943+3607	T9.5	475 (1)	475
2MASS 1047+2124	T6.5	880 (4)	880
2MASS 1114–2618	T7.5	...	678 (3)	669 (4)	674
WISE 1118+3125	T8.5	560 (5)	560
WISE 1141–3326	Y0	425 (2)	425
WISE 1206+8401	Y0	425, 435 (1, 2)	430
2MASS 1217–0311	T7.5	870 (11)	726 (3)	885 (4)	870
WISE 1217+1626A	T9	575, 583 (5, 13)	579
WISE 1217+1626B	Y0	435, 435, 401 (2, 5, 13)	435
2MASS 1225–2739B	T8	850 (5)	850
2MASS 1231+0847	T5.5	1070 (11)	1070
2MASS 1237+6526	T6.5	851 (4)	851
Gl 494C	T8	671 (5)	...	721 (4)	696
WISE 1311+0122	T9:	672 (7)	672
ULAS 1315+0826	T7.5	580 (10)	580
ULAS 1335+1130	T8.5	565, 550 (5, 10)	558
SDSS 1346–0031	T6.5	990 (11)	...	1011 (4)	1001
WISE 1405+5534	Y0.5pec?	375, 385, 415 (1, 2, 5)	385
ULAS 1416+1348	(sd)T7.5	...	605 (3)	656 (4)	631
Gl 547B	sdT8, T8	618 (5)	618

Table 10
(Continued)

Name	Spec. Type	T_{eff} (K) from Forward Modeling (Reference)	T_{eff} (K) from Retrieval Analysis (Reference)	T_{eff} (K) from Stefan–Boltzmann (Reference)	Adopted T_{eff} (K)
(1)	(2)	(3)	(4)	(5)	(6)
Gl 570D	T7.5	800 (11)	715 (3)	759 (4)	759
2MASS 1503+2525	T5	1016 (4)	1016
SDSS 1504+1027	T7	992 (4)	992
WISE 1541–2250	Y1	400, 375, 550, 441 (1, 2, 5, 7)	421
WISE 1542+2230	T9.5	475, 563 (1, 7)	519
2MASS 1553+1532AB	T7	...	803 (3)	...	803
2MASS 1615+1340	T6	906 (4)	906
WISE 1617+1807	T8	600 (12)	600
SDSS 1624+0029	T6	1010 (11)	...	936 (4)	973
WISE 1639–6847	Y0pec	400, 375, 255 (1, 2, 5)	375
WISE 1711+3500A	T8	761 (13)	761
WISE 1711+3500B	T9.5	465 (13)	465
WISE 1738+2732	Y0	400, 425, 440, 514 (1, 2, 5, 7)	433
WISE 1741+2553	T9	615 (5)	615
SDSS 1758+4633	T6.5	980 (11)	980
WISE 1804+3117	T9.5:	620, 706 (5, 7)	663
WISE 1812+2721	T8.5:	620 (12)	620
WISE 1828+2650	\geq Y2	325, 540, 400 (2, 5, 7)	400
SCR 1845–6357B	T6	1000 (14)	1000
WISE 2005+5424	sdT8	750 (15)	750
WISE 2018–7423	T7	710 (12)	710
WISE 2056+1459	Y0	425, 425, 425, 488 (1, 2, 5, 7)	425
ULAS 2146–0010	T8.5	554, 560 (5, 12)	557
Gl 845C	T6	952 (17)	952
WISE 2209+2711	Y0:	525, 325, 400 (1, 2, 7)	400
WISE 2212–6931	T9	550 (1)	550
WISE 2220–3628	Y0	425, 425, 525 (1, 2, 7)	425
2MASS 2228–4310	T6	891, 1110 (4, 11)	1001
WISE 2313–8037	T8	600 (12)	600
ULAS 2321+1354	T7.5	800 (6)	800
WISE 2354+0240	Y1	350, 350 (1, 2)	350

Note. The T_{eff} values taken from Beichman et al. (2014) are those using the models of Morley et al. (2012). Dupuy & Kraus (2013) and Dupuy et al. (2015) used model-dependent bolometric corrections to a limited set of photometry to derive bolometric luminosities, which in turn were used to derive T_{eff} value using model-derived radii. Because this method is so dependent upon a model grid—albeit an evolutionary grid as opposed to an atmospheric one—we categorize these estimates under the forward modeling technique rather than the Stefan–Boltzmann one.

References. References to discovery and spectral classification papers: (1) Schneider et al. (2015), (2) Leggett et al. (2017), (3) Line et al. (2017), (4) Filippazzo et al. (2015), (5) Dupuy & Kraus (2013), (6) Leggett et al. (2010a), (7) Beichman et al. (2014), (8) Manjavacas et al. (2016), (9) Burningham et al. (2011), (10) Marocco et al. (2010), (11) Burgasser et al. (2006a), (12) Burgasser et al. (2010b), (13) Liu et al. (2012), (14) Vigan et al. (2012), (15) Mace et al. (2013b), (16) Dupuy et al. (2015), (17) King et al. (2010).

For objects in Table 7, we have searched for T_{eff} measures in the literature. If an object from Table 7 is not listed in Table 10, that indicates that no T_{eff} measures were readily found for that source. However, if measurements were found, only a sample of the measurements from forward modeling are reproduced in the table, since some of the brighter objects and most of the Y dwarfs have many such references. However, we have listed all instances of the T_{eff} measures from retrieval analysis (all from Line et al. 2017) and from the Stefan–Boltzmann method (all from Filippazzo et al. 2015).²⁶ Many of the T_{eff} measures from forward modeling lack quoted uncertainties, partly due to the

fact that the sparse sampling of the model grids makes interpretation of the actual uncertainty difficult, particularly when the perceived uncertainty is comparable to the T_{eff} step size in the grid itself. For uncertainties in the other values, the reader is referred to the cited paper.

For the nine objects having T_{eff} measures from both retrieval analysis and the Stefan–Boltzmann method, the retrieval values tend to run cooler by ~ 40 K on average. For the seven objects having T_{eff} measures from both forward modeling and retrieval analysis, the retrieval values tend to run cooler by ~ 90 K on average. Indeed, Line et al. (2017) has noted that the retrieval values generally run cooler than the values obtained by other methods. Finally, for the 15 objects having T_{eff} measures from both forward modeling and Stefan–Boltzmann, 9 are warmer in the forward modeling value and 6 are warmer in the Stefan–Boltzmann value. The mean offset for these is ~ 25 K on average, with the T_{eff} measure from forward modeling generally being the warmer one. Because of the sparseness of

²⁶ In actuality, Filippazzo et al. (2015) do not assume $1R_{\text{Jup}}$ radius for all of their T dwarfs but use the radius predicted by evolutionary models matching their age estimates. They use gravity diagnostics, or knowledge of the primary if the T dwarf is a companion, to rule out youth for these T dwarfs, which generally sets the ages to a very large range of 0.5–10 Gyr. However, brown dwarfs at these ages are predicted to have contracted to their final radii, so all of the Filippazzo et al. (2015) sources in Table 10 were found to have radii of essentially $1R_{\text{Jup}}$ anyway (0.94 to $1.06R_{\text{Jup}}$).

Table 11
Effective Temperature Determinations for the 20 pc Census of T6 and Later Dwarfs

Name	Adopted Spec. Type	π_{abs} (mas)	T_{eff} (K)	T_{eff} Methods ^a	(<i>l</i> , <i>b</i>) (deg)	Note
(1)	(2)	(3)	(4)	(5)	(6)	(7)
Warmer objects (>1050 K)						
2MASS 1231+0847	5.5	75.8 ± 4.8	1064	1, 2, 3, 4, 5, 6	287.8 71.1	Section 8.2.35
2MASS 1225-2739A	5.5	76.0 ± 2.5	1060	5	296.0 34.9	Section 8.2.34
900–1050 K						
WISE 2237+7228	6.0	62.3 ± 2.5	1014	1, 2, 3, 4, 5, 6	113.1 12.2	...
2MASS 1503+2525	5.0	157.2 ± 2.2	1009	1, 2, 3, 4, 5, 6	37.2 60.5	...
WISE 0627-1114	6.0	74.8 ± 3.6	1008	1, 2, 3, 4, 5, 6	220.3 -10.4	...
WISE 2343-7418	6.0	58.8 ± 2.7	993	1, 2, 3, 4, 5, 6	309.0 -42.0	...
DENIS 0817-6155	6.0	203.0 ± 13.0	979	1, 2, 3, 4, 5, 6	276.1 -14.4	...
WISE 1928+2356	6.0	149.9 ± 2.4	977	1, 2, 3, 4, 5, 6	58.3 3.1	Section 8.2.48
2MASS 2228-4310	6.0	92.1 ± 2.6	974	1, 2, 3, 4, 5, 6	354.4 -57.0	...
WISE 1627+3255A	[6.0]	54.4 ± 1.9	973	5	53.8 43.4	Section 8.2.44
WISE 1627+3255B	[6.0]	54.4 ± 1.9	973	5	53.8 43.4	Section 8.2.44
WISE 0614+3912A	[6.0]	53.7 ± 1.7	973	5	173.9 10.2	Section 8.2.16
SCR 1845-6357B	6.0	259.5 ± 1.1	968	1, 5	331.5 -23.5	...
SDSS 1346-0031	6.5	69.2 ± 2.3	961	1, 2, 3, 4, 5, 6	330.9 59.3	...
2MASS 0243-2453	6.0	93.6 ± 3.6	954	1, 2, 3, 4, 5, 6	214.2 -64.8	...
WISE 1250+2628	6.5	[53]	953	4, 5	280.8 89.3	...
WISE 1506+7027	6.0	193.5 ± 0.6	952	1, 2, 3, 4, 5, 6	108.3 42.6	...
Gl 845C	6.0	276.1 ± 0.3	949	1, 5	336.1 -48.1	...
WISE 2357+1227	6.0	59.5 ± 4.1	939	1, 2, 3, 4, 5, 6	102.8 -48.3	...
2MASS 1615+1340	6.0	58.4 ± 2.5	930	1, 2, 3, 4, 5, 6	27.7 40.8	...
WISE 1501-4004	6.0	69.5 ± 4.0	929	1, 2, 3, 4, 5, 6	328.3 16.3	Section 8.2.39
SDSS 1624+0029	6.0	91.8 ± 1.2	924	1, 2, 3, 4, 5, 6	14.6 32.5	...
WISE 1906+4508	6.0	64.1 ± 1.6	923	1, 2, 3, 4, 5, 6	75.7 16.4	...
2MASS 0937+2931	6.0	162.8 ± 3.9	920	1, 2, 3, 4, 5, 6	197.9 47.6	...
WISE 0513+0608	6.5	70.8 ± 1.5	917	1, 2, 3, 4, 5, 6	195.5 -18.6	...
VHS 1258-4412	6.0	63.8 ± 4.0	914	2, 3, 5, 6	304.2 18.6	...
Gl 576B	6.0	52.7 ± 0.3	914	1, 2, 3, 4, 5, 6	4.9 51.7	...
WISE 1221-3136	6.5	73.8 ± 3.3	910	1, 2, 3, 4, 5, 6	295.6 30.9	...
SDSS 1758+4633	6.5	71.4 ± 0.3	909	1, 2, 3, 4, 5, 6	73.5 28.2	...
WISE 2301+0216	6.5	53.0 ± 2.8	902	1, 2, 3, 4, 5, 6	76.6 -50.4	...
750–900 K						
WISE 0542-1628	6.5	61.5 ± 2.7	895	1, 2, 3, 4, 5, 6	220.6 -22.5	...
2MASS 1553+1532A	6.5	75.1 ± 0.9	892	5	27.1 46.4	Section 8.2.43
WISE 1122+2550	6.0	66.3 ± 2.3	890	1, 2, 3, 4, 5, 6	211.6 70.2	...
2MASS 1047+2124	6.5	94.7 ± 3.8	890	1, 2, 3, 4, 5, 6	217.7 61.3	Section 8.2.28
WISE 1320+6034	6.5	60.6 ± 2.5	879	1, 2, 3, 4, 5, 6	116.6 56.2	...
WISE 0241-3653	7.0	52.4 ± 2.7	879	1, 2, 3, 4, 5, 6	242.7 -64.8	...
2MASS 1237+6526	6.5	96.1 ± 4.8	878	1, 2, 3, 4, 5, 6	125.2 51.6	...
WISE 0325+0831	7.0	78.5 ± 3.0	876	1, 2, 3, 4, 5, 6	174.8 -38.3	...
WISE 0040+0900	7.0	69.8 ± 1.5	870	1, 2, 3, 4, 5, 6	118.3 -53.8	...
Gl 229B	7.0	172.7 ± 0.3	864	1, 5	228.6 -18.4	...
2MASS 0034+0523	6.5	120.1 ± 3.0	859	1, 2, 3, 4, 5, 6	115.3 -57.2	...
WISE 2213+0911	7.0	54.5 ± 2.5	855	1, 2, 3, 4, 5, 6	71.0 -37.3	...
WISE 1124-0421	7.0	61.6 ± 3.1	853	2, 3, 5, 6	266.0 52.2	...
WISE 1039-1600	7.5	53.4 ± 2.6	839	1, 2, 3, 4, 5, 6	262.4 36.2	...
2MASS 1217-0311	7.5	91.7 ± 2.2	839	1, 2, 3, 4, 5, 6	286.4 58.6	...
2MASS 0050-3322	7.0	94.6 ± 2.4	835	1, 2, 3, 4, 5, 6	305.0 -83.7	...
2MASS 0348-6022	7.0	120.1 ± 1.8	832	1, 2, 3, 4, 5, 6	273.6 -45.4	...
WISE 0614+0951	7.0	65.6 ± 2.2	829	1, 2, 3, 4, 5, 6	199.9 -3.6	...
WISE 1735-8209	6.0	75.1 ± 4.6	828	1, 2, 3, 4, 5, 6	311.1 -24.4	...
WISE 0645-0302	6.0	50.7 ± 4.2	827	1, 2, 3, 4, 5, 6	215.0 -2.7	...
WISE 1852+3537	7.0	72.0 ± 1.9	825	1, 2, 3, 4, 5, 6	65.5 15.2	...
WISE 1457+5815	7.0	55.0 ± 2.3	825	1, 2, 3, 4, 5, 6	96.5 51.9	...
WISE 1052-1942	7.5	62.3 ± 4.4	821	1, 2, 3, 4, 5, 6	268.3 35.1	...
2MASS 0727+1710	7.0	112.5 ± 0.9	817	1, 2, 3, 4, 5, 6	201.3 15.5	...
WISE 0309-5016A	[7.0]	66.8 ± 3.9	816	5	263.8 -55.0	Section 8.2.5
WISE 0309-5016B	[7.0]	66.8 ± 3.9	816	5	263.8 -55.0	Section 8.2.5
WISE 2348-1028	7.0	58.4 ± 3.5	806	1, 2, 3, 4, 5, 6	78.4 -67.7	...
SDSS 1628+2308	7.0	75.1 ± 0.9	805	1, 2, 3, 4, 5, 6	40.9 41.0	...

Table 11
(Continued)

Name (1)	Adopted Spec. Type (2)	π_{abs} (mas) (3)	T_{eff} (K) (4)	T_{eff} Methods ^a (5)	(l, b) (deg) (6)	Note (7)
WISE 2226+0440	8.0	54.4 ± 5.9	791	1, 2, 3, 4, 5, 6	69.6 –42.7	Section 8.2.53
WISE 0521+1025	7.5	[171]	786	4, 5	192.8 –14.6	...
WISE 0245–3450	8.0	[59]	780	4, 5, 6	237.6 –64.5	...
WISE 2157+2659	7.0	59.7 ± 2.2	779	1, 2, 3, 4, 5, 6	81.7 –21.7	...
WISE 1612–3420	6.5	78.3 ± 3.5	770	1, 2, 3, 4, 5, 6	343.4 12.3	...
WISE 2000+3629	8.0	133.1 ± 2.5	768	1, 2, 3, 4, 5, 6	72.7 3.3	...
WISE 2209–2734	7.0	78.2 ± 3.9	764	1, 2, 3, 4, 5, 6	22.6 –54.2	...
WISE 2018–7423	7.0	83.2 ± 1.9	761	1, 2, 3, 4, 5, 6	320.0 –31.9	...
Gl 570D	7.5	171.2 ± 0.9	755	1, 2, 3, 4, 5, 6	338.2 32.7	...
WISE 0628–8057	[9.0]	[50]	754	6	292.8 –27.7	...
600–750 K						
WISE 2005+5424	8.0	62.9 ± 3.3	750	7	88.6 11.9	Section 8.2.49
WISE 2211–4758	[8.0]	55.8 ± 4.6	746	1, 2, 3, 4, 6	348.1 –52.7	...
ULAS 1416+1348A	[7.5]	109.7 ± 1.3	744	5	3.3 66.1	Section 8.2.38
ULAS 1416+1348B	[7.5]	109.7 ± 1.3	744	5	3.3 66.1	Section 8.2.38
2MASS 1553+1532B	7.5	75.1 ± 0.9	744	5	27.1 46.4	Section 8.2.43
2MASS 0729–3954	8.0	126.3 ± 8.3	736	1, 2, 3, 4, 5, 6	252.6 –10.4	...
WISE 1523+3125	6.5	61.4 ± 3.8	735	1, 2, 3, 4, 5, 6	49.6 56.8	Section 8.2.40
WISE 1322–2340	8.0	77.5 ± 4.2	735	1, 2, 3, 4, 5, 6	312.1 38.6	Section 8.2.36
ULAS 2321+1354	7.5	83.6 ± 2.4	735	1, 2, 3, 4, 5, 6	92.1 –43.5	...
WISE 1813+2835	8.0	74.9 ± 2.5	731	1, 2, 3, 4, 5, 6	55.5 20.3	Section 8.2.46
WISE 2302–7134	[4.5]	65.1 ± 4.7	726	1, 2, 3, 4, 6	314.3 –43.1	...
WISE 1959–3338	8.0	85.3 ± 2.2	724	1, 2, 3, 4, 5, 6	7.3 –27.9	...
Gl 494C	8.0	85.5 ± 1.5	724	1, 2, 3, 4, 5, 6	311.7 75.1	...
ULAS 1029+0935	8.0	66.8 ± 4.2	718	1, 2, 3, 4, 5, 6	233.8 52.3	...
ULAS 0859+1010	7.0	50.3 ± 1.7	716	1, 2, 4, 5	218.4 32.9	...
WISE 2255–3118	8.0	70.7 ± 4.2	713	1, 2, 3, 4, 5, 6	16.5 –64.5	...
Gl 27B	8.0	90.4 ± 0.3	711	1, 3, 5, 6	119.2 –41.5	...
WISE 0223–2932	7.5	80.7 ± 2.6	709	1, 2, 3, 4, 5, 6	225.2 –69.7	...
WISE 1653+4444	8.0	78.0 ± 4.2	699	1, 2, 3, 4, 5, 6	70.0 39.3	...
WISE 0623–0456	8.0	87.4 ± 2.9	699	1, 2, 3, 4, 5, 6	214.1 –8.5	...
WISE 1318–1758	8.0	57.8 ± 2.7	696	1, 2, 3, 4, 5, 6	312.0 44.4	...
WISE 1301–0302	8.5	53.8 ± 5.6	694	1, 2, 3, 4, 5, 6	308.0 59.7	...
WISE 0744+5628	8.0	67.1 ± 2.5	693	1, 2, 3, 4, 5, 6	161.1 29.6	...
WISE 2313–8037	8.0	93.5 ± 2.7	692	1, 2, 3, 4, 5, 6	307.7 –35.6	...
2MASS 1114–2618	7.5	179.2 ± 1.4	692	1, 2, 3, 4, 5, 6	277.4 31.7	Section 8.2.30
WISE 2319–1844	7.5	79.2 ± 3.1	688	1, 2, 3, 4, 5, 6	49.8 –67.3	...
WISE 0015–4615	8.0	71.8 ± 2.7	688	1, 2, 3, 4, 5, 6	321.2 –69.6	...
WISE 0759–4904	8.0	89.1 ± 2.4	685	1, 2, 3, 4, 5, 6	263.5 –10.0	...
WISE 0254+0223	8.0	146.1 ± 1.5	685	1, 2, 3, 4, 5, 6	172.8 –48.2	Section 8.2.3
2MASS 0415–0935	8.0	175.2 ± 1.7	685	1, 2, 3, 4, 5, 6	202.9 –38.9	...
ULAS 0950+0117	8.0	57.9 ± 2.3	682	1, 2, 3, 4, 5, 6	236.0 39.6	...
WISE 0226–0211A	[8.0]	57.3 ± 4.7	678	5	169.3 –56.3	Section 8.2.2
WISE 0614+3912B	[8.0]	53.7 ± 1.7	678	5	173.9 10.2	Section 8.2.16
2MASS 0939–2448A	[8.0]	187.3 ± 4.6	678	5	256.9 20.5	Section 8.2.27
2MASS 0939–2448B	[8.0]	187.3 ± 4.6	678	5	256.9 20.5	Section 8.2.27
2MASS 1225–2739B	8.0	76.0 ± 2.5	678	5	296.0 34.9	Section 8.2.34
WISE 0247+3725	8.0	64.8 ± 2.6	674	1, 2, 3, 4, 5, 6	147.1 –20.0	...
ULAS 0901–0306	7.5	62.6 ± 2.6	673	1, 2, 3, 4, 5, 6	232.1 26.9	...
WISE 0857+5604	8.0	87.2 ± 2.4	661	1, 2, 3, 4, 5, 6	161.1 39.6	...
WISE 0723+3403	9.0	56.3 ± 3.5	660	1, 2, 3, 4, 5, 6	184.4 20.9	Section 8.2.19
ULAS 1302+1308	8.0	65.0 ± 5.0	659	1, 2, 3, 4, 5, 6	313.7 75.8	...
WISE 2203+4619	8.0	66.0 ± 4.2	658	1, 2, 3, 4, 5, 6	95.1 –7.3	...
WISE 1519+7009	8.0	77.6 ± 2.8	652	1, 2, 3, 4, 5, 6	107.0 42.1	...
WISE 1448–2534	8.0	52.5 ± 2.5	652	1, 2, 3, 4, 5, 6	333.5 30.3	...
CFBDS 0133+0231	8.5	56.3 ± 3.4	652	1, 2, 3, 4, 5, 6	143.2 –58.7	...
WISE 2019–1148	8.0	77.5 ± 3.5	651	1, 2, 3, 4, 5, 6	32.0 –24.8	...
ULAS 0034–0052	8.5	68.7 ± 1.4	645	1, 2, 3, 4, 5, 6	113.2 –63.4	...
WISE 1617+1807	8.0	84.6 ± 4.2	641	1, 2, 3, 4, 5, 6	33.4 42.0	...
WISE 1018–2445	8.0	83.6 ± 3.6	640	1, 2, 3, 4, 5, 6	264.0 26.3	...
WISE 0323–6025	8.5	71.4 ± 2.9	629	1, 2, 3, 4, 5, 6	275.9 –47.9	...
WISE 0049+2151	8.5	139.9 ± 2.5	629	1, 2, 3, 4, 5, 6	122.4 –41.0	...

Table 11
(Continued)

Name	Adopted Spec. Type	π_{abs} (mas)	T_{eff} (K)	T_{eff} Methods ^a	(<i>l</i> , <i>b</i>) (deg)	Note
(1)	(2)	(3)	(4)	(5)	(6)	(7)
ULAS 1315+0826	7.5	50.5 ± 5.7	628	1, 2, 4, 5	320.7 70.5	...
WISE 1051–2138	8.5	67.0 ± 3.0	625	1, 2, 3, 4, 5, 6	269.2 33.2	...
UGPS 0521+3640	8.5	122.2 ± 1.6	625	1, 2, 3, 4, 5, 6	170.7 –0.0	Section 8.2.13
WISE 0323–5907	[6.0]	71.5 ± 4.3	623	2, 3, 6	274.4 –48.7	Section 8.2.7
VHS 1433–0837	8.0	50.9 ± 4.5	622	1, 2, 3, 4, 5, 6	341.1 46.6	...
GI 547B	8.0	58.2 ± 0.5	618	7	347.2 56.0	...
WISE 0458+6434A	8.5	109.2 ± 3.6	616	5	145.8 13.4	Section 8.2.12
ULAS 0745+2332	8.5	[63]	616	5	196.8 21.8	...
WISE 0500–1223	8.0	95.1 ± 3.6	614	1, 2, 3, 4, 5, 6	211.8 –30.3	...
WISE 1025+0307	8.5	85.4 ± 2.5	612	1, 2, 3, 4, 5, 6	241.2 47.8	...
WISE 0032–4946	8.5	63.6 ± 2.9	610	1, 2, 3, 4, 5, 6	310.8 –67.1	...
WISE 0615+1526	8.5	[64]	607	5, 6	195.2 –0.6	...
WISE 0750+2725	8.5	68.4 ± 3.4	605	1, 2, 3, 4, 5, 6	193.2 24.2	...
ULAS 2146–0010	8.5	79.8 ± 4.5	604	1, 2, 3, 4, 5, 6	56.4 –38.1	Section 8.2.50
WISE 1042–3842	8.5	65.4 ± 3.4	601	1, 2, 3, 4, 5, 6	277.1 17.6	...
CFBDS 0059–0114	8.5	103.2 ± 2.1	601	1, 2, 3, 4, 5, 6	127.4 –64.0	...
450–600 K						
WISE 1150+6302	8.0	124.5 ± 3.0	599	2, 3, 5, 6	134.3 52.7	...
WISE 0540+4832	8.5	70.0 ± 2.6	598	1, 2, 3, 4, 5, 6	162.7 9.4	Section 8.2.15
WISE 1804+3117	9.5	62.7 ± 3.4	597	1, 2, 3, 4, 5, 6	57.5 23.0	Section 8.2.45
WISE 1118+3125	8.5	113.2 ± 4.6	595	1, 2, 3, 4, 5, 6	195.4 69.4	...
WISE 0313+7807	8.5	134.3 ± 3.6	595	1, 2, 3, 4, 5, 6	130.1 17.3	...
ULAS 1335+1130	8.5	99.9 ± 1.6	593	1, 2, 3, 4, 5, 6	338.8 71.2	...
WISE 2344+1034	9.0	64.7 ± 3.7	592	1, 2, 3, 4, 5, 6	97.5 –49.0	Section 8.2.54
WISE 0316+4307	8.0	73.3 ± 2.8	582	1, 2, 3, 4, 5, 6	149.1 –12.3	Section 8.2.6
WISE 1741+2553	9.0	214.3 ± 2.8	578	1, 2, 3, 4, 5, 6	50.1 26.1	...
WISE 0325–3854	9.0	57.2 ± 5.4	574	1, 2, 3, 4, 5, 6	243.1 –56.0	...
WISE 2102–4429	9.0	92.9 ± 1.9	573	1, 2, 3, 4, 5, 6	356.2 –41.5	...
WISE 1311+0122	9.0	68.8 ± 2.7	567	1, 2, 3, 4, 5, 6	314.1 63.8	...
WISE 0005+3737	9.0	127.0 ± 2.4	564	1, 2, 3, 4, 5, 6	112.9 –24.4	...
WISE 2159–4808	9.0	75.7 ± 2.7	562	1, 2, 3, 4, 5, 6	348.8 –50.8	...
WISE 2332–4325	9.0	65.3 ± 2.6	559	1, 2, 3, 4, 5, 6	342.2 –67.2	...
WISE 1217+1626A	9.0	104.4 ± 4.7	559	5	265.2 76.8	Section 8.2.33
WISE 1112–3857	9.0	[56]	559	4, 5, 6	282.7 20.0	...
WISE 0146+4234A	9.0	52.5 ± 2.3	559	5	133.7 –19.1	Section 8.2.1
WISE 0038+2758	9.0	89.7 ± 2.5	557	1, 2, 3, 4, 5, 6	119.4 –34.8	...
WISE 0430+4633	8.0	93.9 ± 4.1	553	1, 2, 3, 4, 5, 6	157.2 –1.2	Section 8.2.11
WISE 1812+2721	8.5	98.5 ± 4.4	552	1, 2, 3, 4, 5, 6	54.2 20.1	...
UGPS 0722–0540	9.0	242.8 ± 2.4	552	1, 2, 3, 4, 5, 6	221.5 4.3	...
WISE 0713–5854	9.0	78.2 ± 4.6	546	1, 2, 3, 4, 5, 6	269.7 –20.3	Section 8.2.18
WISE 0335+4310	9.0	72.1 ± 2.4	545	1, 2, 3, 4, 5, 6	152.0 –10.3	Section 8.2.8
WISE 2134–7137	9.0	109.7 ± 3.7	538	1, 2, 3, 4, 5, 6	320.5 –38.0	...
WISE 1614+1739	9.0	97.6 ± 3.4	538	1, 2, 3, 4, 5, 6	32.6 42.4	...
WISE 2325–4105	9.0	108.4 ± 3.7	523	1, 2, 3, 4, 5, 6	349.1 –67.5	...
WISE 0148–7202	9.5	91.7 ± 3.4	520	1, 2, 3, 4, 5, 6	296.9 –44.4	...
WISE 1055–1652	9.5	72.2 ± 2.7	509	2, 3, 5, 6	267.1 37.8	...
WISE 0458+6434B	9.5	109.2 ± 3.6	508	5	145.8 13.4	Section 8.2.12
WISE 0226–0211B	[9.5]	57.3 ± 4.7	508	5	169.3 –56.3	Section 8.2.2
WISE 0751–7634	9.0	97.9 ± 6.7	507	1, 2, 3, 4, 5, 6	288.8 –23.0	Section 8.2.21
WISE 0811–8051	9.5	99.1 ± 7.7	493	1, 2, 3, 4, 5, 6	293.5 –23.7	Section 8.2.23
WISE 2212–6931	9.0	81.9 ± 2.5	489	1, 2, 3, 4, 5, 6	320.4 –41.8	Section 8.2.52
WISE 0943+3607	9.5	93.8 ± 2.8	489	1, 2, 3, 4, 5, 6	188.1 49.3	...
WISE 0833+0052	9.0	82.6 ± 4.5	486	1, 2, 3, 4, 5, 6	224.4 23.0	Section 8.2.25
WISE 1542+2230	9.5	85.6 ± 4.2	481	1, 2, 3, 4, 5, 6	35.8 51.2	Section 8.2.42
WISE 0302–5817	10.0	56.1 ± 4.4	471	2, 3, 5, 6	275.8 –51.4	...
WISE 2056+1459	10.0	138.3 ± 2.2	467	1, 2, 3, 4, 5, 6	62.0 –19.2	...
WISE 0734–7157	10.0	75.0 ± 2.4	466	1, 2, 3, 4, 5, 6	283.7 –22.4	Section 8.2.20
WISE 0713–2917	10.0	107.5 ± 2.4	466	1, 2, 3, 4, 5, 6	241.5 –8.6	...
WISE 0336–0143	10.0	99.0 ± 2.4	464	2, 3, 5, 6	187.3 –43.1	...
WISE 1141–3326	10.0	99.7 ± 4.2	463	2, 3, 5, 6	286.7 27.2	Section 8.2.31
WISE 1217+1626B	10.0	104.4 ± 4.7	461	5	265.2 76.8	Section 8.2.33
WISE 0146+4234B	10.0	52.5 ± 2.3	461	5	133.7 –19.1	Section 8.2.1

Table 11
(Continued)

Name (1)	Adopted Spec. Type (2)	π_{abs} (mas) (3)	T_{eff} (K) (4)	T_{eff} Methods ^a (5)	(<i>l</i> , <i>b</i>) (deg) (6)	Note (7)
WISE 1206+8401	10.0	81.9 ± 2.5	459	1, 2, 3, 4, 5, 6	124.3 33.0	...
WISE 2220–3628	10.0	97.0 ± 2.4	458	1, 2, 3, 4, 5, 6	7.0 –56.9	...
WISE 0304–2705	10.0	81.5 ± 7.7	458	1, 2, 3, 4, 5, 6	220.6 –60.4	Section 8.2.4
WISE 0410+1502	10.0	150.2 ± 2.4	454	1, 2, 3, 4, 5, 6	177.9 –25.9	...
300–450 K						
WISE 0359–5401	10.0	75.8 ± 2.5	445	1, 2, 3, 4, 5, 6	264.3 –46.5	Section 8.2.10
WISE 1738+2732	10.0	131.0 ± 2.4	435	1, 2, 3, 4, 5, 6	51.6 27.2	...
WISE 1828+2650	12.0	100.7 ± 2.3	412	1, 2, 3, 4, 5, 6	55.1 16.6	Section 8.2.47
WISE 1639–6847	10.0	211.9 ± 2.7	403	1, 2, 3, 4, 5, 6	321.2 –14.5	...
WISE 1405+5534	10.5	157.9 ± 3.1	402	1, 2, 3, 4, 5, 6	102.8 58.6	Section 8.2.37
WISE 0535–7500	11.0	66.4 ± 2.4	398	1, 2, 3, 4, 5, 6	286.3 –31.0	Section 8.2.14
WISE 1541–2250	11.0	167.1 ± 2.3	395	1, 2, 3, 4, 5, 6	346.5 25.3	Section 8.2.41
WISE 0647–6232	11.0	100.3 ± 2.4	381	1, 2, 3, 4, 5, 6	272.5 –24.3	Section 8.2.17
WISE 2354+0240	11.0	124.1 ± 4.9	374	1, 2, 3, 4, 5, 6	95.8 –57.1	...
WD 0806B	[11.0]	52.2 ± 1.7	369	1, 2, 3, 4, 6	279.4 –17.5	Section 8.2.22
WISE 0825+2805	10.5	155.8 ± 2.4	364	1, 2, 3, 4, 5, 6	195.2 31.8	Section 8.2.24
WISE 2209+2711	10.0	161.6 ± 2.4	360	1, 2, 3, 4, 5, 6	83.9 –23.1	Section 8.2.51
WISE 0350–5658	11.0	174.6 ± 2.6	355	1, 2, 3, 4, 5, 6	269.0 –46.7	Section 8.2.9
150–300 K						
WISE 0855–0714	[14.0]	438.9 ± 3.0	250	0	235.0 23.4	Section 8.2.26

Note. Spectral types and parallaxes in brackets are estimates, not actual measures. Spectral types are coded as T6 = 6.0, T6.5 = 6.5, T7 = 7.0, ... Y0 = 10.0, etc.
^a These are the methods used in determining the T_{eff} value for the source: 1 = M_H relation, 2 = M_{W2} relation, 3 = M_{ch2} relation, 4 = $H-W2$ relation, 5 = spectral type relation, 6 = ch1–ch2 relation, 7 = value taken from Table 10. All relations are those shown in Figure 14 and described in the last six lines of Table 8.

these comparison data, we have not attempted a correction from one method to the other since there are likely to be correlations with spectral type and/or color as well. So, for each object we merely take a median of all available measures and list that as the adopted T_{eff} value in Table 10. These adopted values are the ones used in the analysis below.

Figure 14 shows the adopted T_{eff} values from Table 10 and the collected photometry and parallax information from Table 7 to illustrate the trend of temperature with absolute magnitudes, colors, and spectral type. Fits to the relations, excluding known binaries and subdwarfs, are shown in the figure and described in Table 8.

Using these polynomial relations, we can assign T_{eff} values to all objects in the 20 pc sample. Table 11 gives these values and the method used in their determination. We use all relations if the supporting data have been measured, and take the median of the individual results as the adopted T_{eff} value. Table 11 lists which of the relations were used for each source. In the case of two of the subdwarfs, measured values from the literature were used instead.

The objects in Table 11 represent all of the T and Y dwarfs in Table 1 that have absolute parallax values ≥ 50 mas. Binaries are listed as separate objects, with individual spectral types being those discussed in Section 8.2. (For suspected binaries with no other corroborating information, equal-magnitude binaries were assumed for which the individual components have the same spectral type as the component system.) Objects are ordered by our T_{eff} determinations and grouped into 150 K bins to coincide with the binning given in Figures 12 and 13. There are six such bins running from 150 to 1050 K. The hottest of these bins, from 900 to 1050 K, primarily includes T6 and T6.5 dwarfs. We note that of the 28 objects in this bin, 13 fall in the 50 K range from

900 to 950 K, 12 fall in the range 950–1000 K, and only 3 fall in the range 1000–1050 K. By performing a spectral type cut of $\geq T6$, we have removed some earlier type objects that should otherwise be counted here. In fact, one such object that inadvertently was added to the sample—the T5 dwarf 2MASS 1503+2525—has a temperature determination of 1009 K. Thus, we should consider this bin to be incomplete.

A similar analysis shows that the two low-temperature bins are also incomplete. The 150–300 K bin contains only WISE 0855–0714, at $d = 2.3$ pc and $T_{\text{eff}} = 250$ K. Cooler and/or more distant brown dwarfs are expected to be missing from this bin because of their extreme faintness. The bin from 300 to 450 K contains 13 objects, but none of these fall in the 50 K bin from 300 to 350 K. Objects in this temperature range have also likely eluded detection.

In addition to incompleteness related to spectral type and intrinsically dim magnitudes, we need to determine if our goal of identifying a complete 20 pc sample has been successful. The standard analysis used for this is the V/V_{max} test of Schmidt (1968), which checks the distribution of objects in space. In each 150 K bin, each object is assigned a value V that is the volume of space interior to the object at the distance corresponding to its parallax. The value V_{max} is the full volume of space contained within the distance limit being considered. For a uniform sample, the average value, $\langle V/V_{\text{max}} \rangle$, should be ~ 0.5 because half of the sample should lie in the closer half of the volume and the rest should lie in the more distant half. If the value of $\langle V/V_{\text{max}} \rangle$ is significantly different from 0.5, then the sample is either non-homogeneous or incomplete. Given that we expect old, solivagant brown dwarfs to be isotropically distributed in space, this would indicate incompleteness to the distance limit being considered.

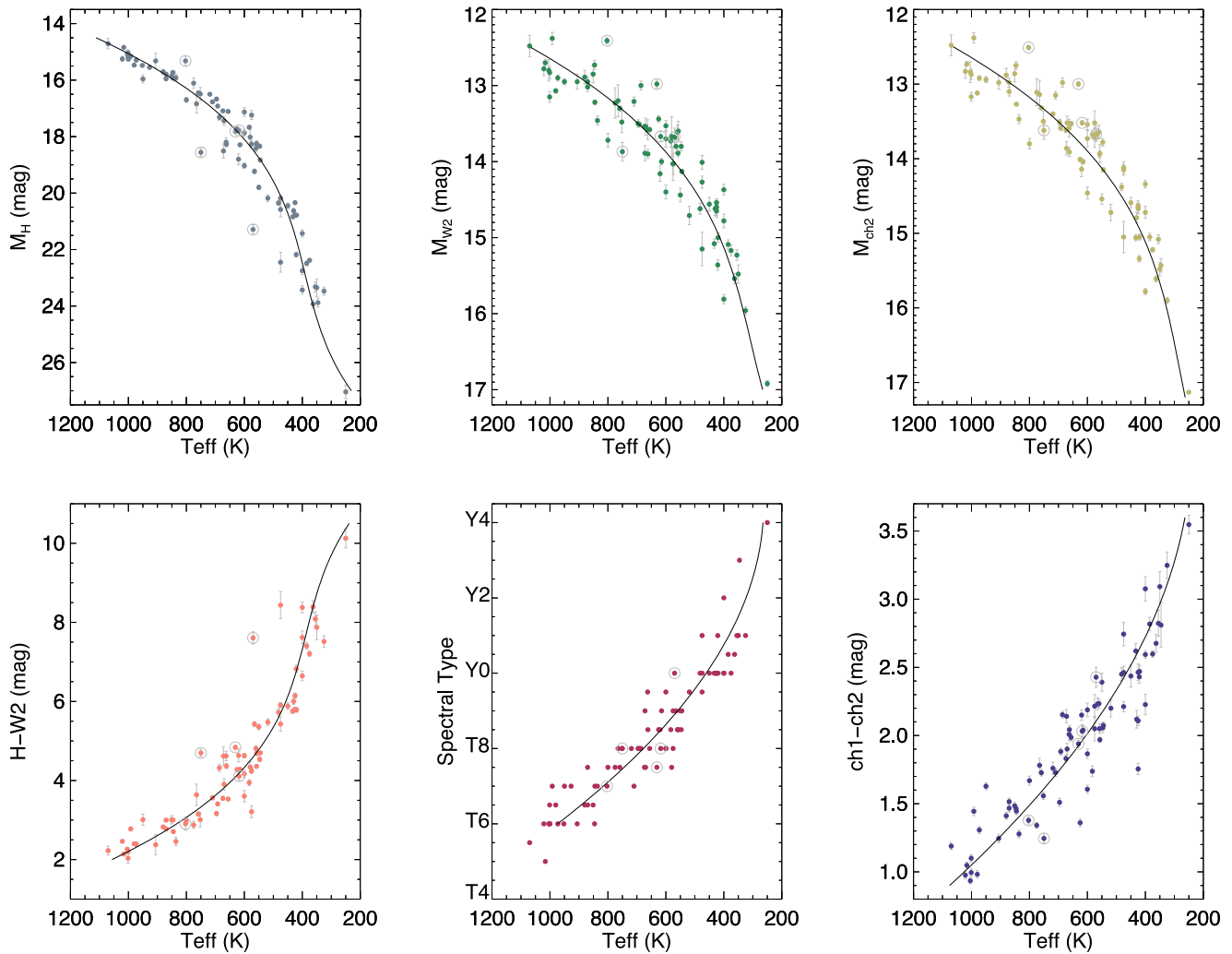


Figure 14. Trends of adopted T_{eff} with M_H , M_{W2} , and M_{ch2} magnitudes, $H-W2$ color, spectral type, and $\text{ch1}-\text{ch2}$ color, as taken from the data in Tables 7 and 10. Polynomial fits to the data are shown on the plots and described in Table 8. Open circles in these three panels indicate data points that were excluded from the fits because the objects are binary or known to be of low metallicity.

Using the parallaxes listed in Table 11, we can measure the value of $\langle V/V_{\text{max}} \rangle$ for many different assumed limiting distances. These results are shown in Figure 15, for five of our six 150 K bins. (The coldest bin, from 150–300 K, is not shown since it contains only one known object.) At distances of only a few parsecs, for which there are only a handful of objects, the values of $\langle V/V_{\text{max}} \rangle$ vary wildly. For most bins, however, this value stabilizes near 0.5 as larger distances and larger number of objects are considered. At distances beyond 20 pc, the value of $\langle V/V_{\text{max}} \rangle$ drops steadily since the list in Table 11 contains no objects more distant than this limit.

Given that there are, at most, only a few dozen objects in each 150 K temperature bin, random fluctuations due to poor statistics can naturally cause the value of $\langle V/V_{\text{max}} \rangle$ to deviate from 0.5. What value of $\langle V/V_{\text{max}} \rangle$ should we take to indicate true incompleteness? To answer this question, we assume a perfectly uniform sample and examine the scale of deviations from $\langle V/V_{\text{max}} \rangle = 0.5$ that can be imparted due to sample size. For instance, consider a sample of two marbles for which each marble is equally likely to fall in bucket A (representing the nearer half of the sky) or bucket B (representing the more distant half). There is a 50% probability that two marbles will

fall into different buckets, a 25% probability that both will fall in bucket A, and a 25% probability that both will fall in bucket B. By analogy with a sky distribution of brown dwarfs, $\langle V/V_{\text{max}} \rangle$ values can thus range as low as 0.0 and as high as 1.0, with only half of the values falling at or near 0.5.

We can generalize this argument to any number of marbles, although we consider only even numbers so that the average value becomes the same number of marbles in each bucket (roughly equivalent to $\langle V/V_{\text{max}} \rangle = 0.5$). The likelihood that the same number of marbles, n , falls in each bucket is given by

$$\frac{n!}{\left(\frac{n}{2}\right)! \left(\frac{n}{2}\right)! 2^n}.$$

The likelihood that we find a different number of marbles, differing by the integer a , is twice the following value (with the additional factor of two coming from the fact that the number in bucket A can be larger by a than that in bucket B or vice versa)

$$\frac{n!}{\left(\frac{n}{2} - a\right)! \left(\frac{n}{2} + a\right)! 2^n}.$$

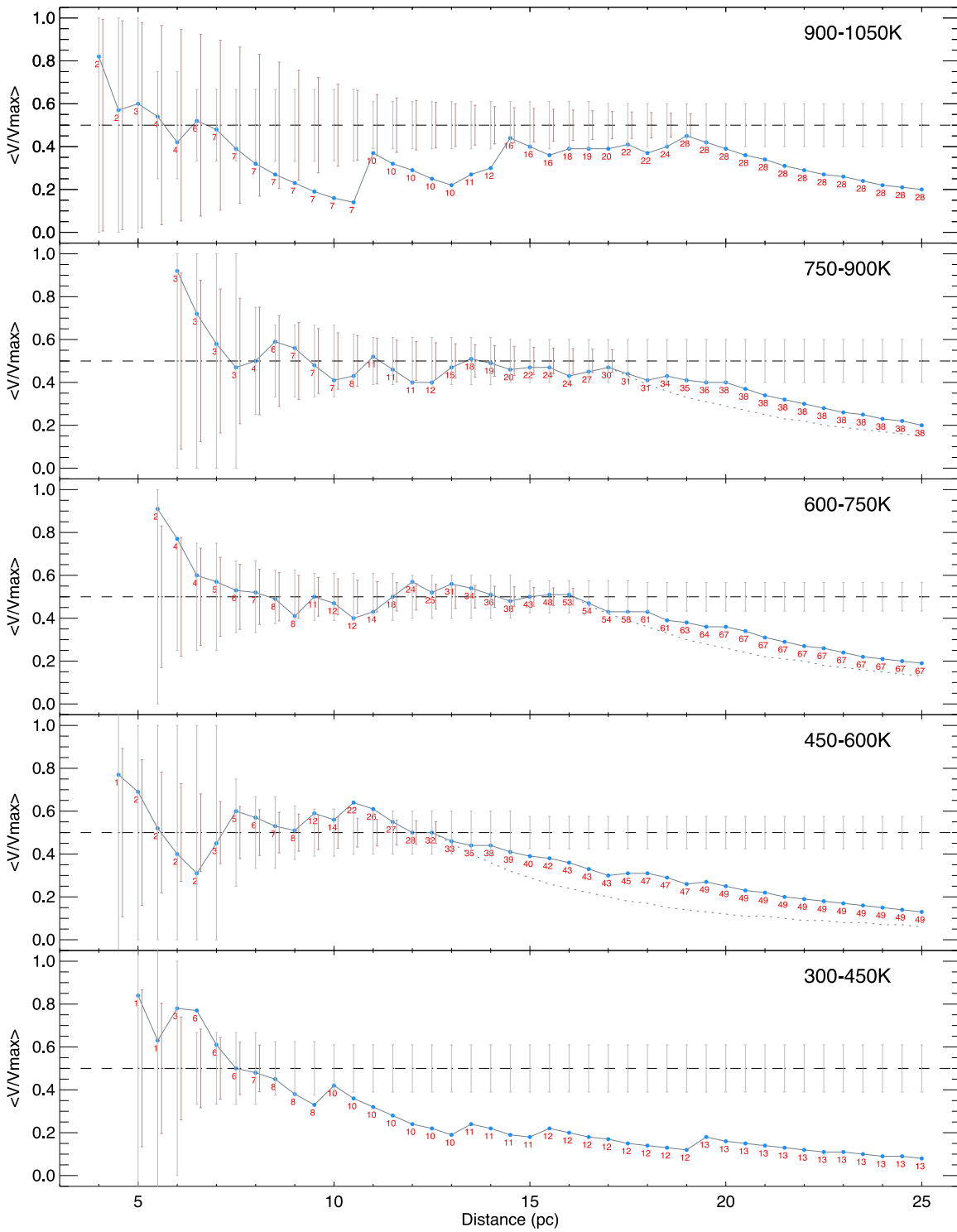


Figure 15. Average V/V_{\max} value in 0.5 pc intervals for five of the six 150 K bins encompassing our 20 pc T6-Y4 sample. (The sixth bin, from 150 to 300 K, is not shown because it contains only one object, WISE 0855–0714.) Blue dots represent our empirical sample. Red labels mark the number of objects in the computation at each 0.5 pc interval. The black dashed line shows the $\langle V/V_{\max} \rangle = 0.5$ level indicating a complete sample. The gray error bars show the approximate 1σ range around $\langle V/V_{\max} \rangle = 0.5$ that a complete sample of the size indicated by the red number would exhibit, given random statistics. The brown error bars, offset by +0.05 pc from the gray error bars for clarity, show the 1σ variation around 0.5 obtained by 10,000 Monte Carlo simulations having the same number of objects and the same completeness limit listed in Table 12. The gray dotted lines in the middle three panels show the drop in $\langle V/V_{\max} \rangle$ for a fixed number of objects, where the fixed value is set to the number of objects where $\langle V/V_{\max} \rangle$ last crosses ~ 0.5 . See text for details. (Data in support of this figure can be found in Table 15.)

We can determine the value of a_{\max} at which we reach a cumulative probability, summed over all values of a from $a_{\min} = 0$ (the case of equal numbers in both buckets) to a_{\max} ,

of $\sim 68\%$. This will allow us to determine a “most likely” range analogous to the Gaussian statistical concept of a 1σ likelihood. Because marbles, and brown dwarfs, are quantized, so are the

Table 12
Space Density Measurements for Early-L through Early-Y Dwarfs

T_{eff} Range (K) (1)	Completeness Limit (pc) (2)	No. of Objects (3)	Adjustment Factor (4)	Adopted Space Density ($\times 10^{-3} \text{ pc}^{-3}$) (5)
1950–2100	20.0	19	1.00	0.57 ± 0.20
1800–1950	20.0	16	1.00	0.48 ± 0.12
1650–1800	20.0	21	1.00	0.63 ± 0.09
1500–1650	20.0	26	1.00	0.78 ± 0.11
1350–1500
1200–1350
1050–1200
900–1050	19.0	28	1.15	>1.12
750–900	17.0	30	1.15	1.68 ± 0.23
600–750	16.0	53	1.15	3.55 ± 0.51
450–600	12.5	32	1.15	4.50 ± 0.81
300–450	8.0	7	1.15	>3.75
150–300	...	1

cumulative probabilities, so we consider the value of a_{max} for which the cumulative probability first exceeds 68%. We then take $0.5 - ((n/2) - a_{\text{max}})/n$ as the approximation for the 1σ range on $\langle V/V_{\text{max}} \rangle$ for a uniformly distributed set of n objects. We find that for $n = 100$, the 1σ value for $\langle V/V_{\text{max}} \rangle$ is ~ 0.050 ; for $n = 50$ it is ~ 0.075 ; and for $n = 30$ it is ~ 0.100 . For smaller values of n this 1σ value dramatically jumps: 0.11 for $n = 10$, 0.125 for $n = 8$, 0.167 for $n = 6$, and 0.25 for $n = 4$. These 1σ values are the ones shown as the gray uncertainties around the $\langle V/V_{\text{max}} \rangle = 0.5$ line on Figure 15. The 1σ value chosen is the one corresponding to the number of objects (in red on the plot and denoted as n here) being used in the computation at that distance. (When n is odd, we use the 1σ value measured for $n - 1$.)

With these likelihoods in mind, we can now better interpret the curves shown in Figure 15. For the 900–1050 K bin, the largest distance at which the $\langle V/V_{\text{max}} \rangle$ value is ~ 0.5 is $d = 19.0$ pc, and there are 28 objects out to this distance, for a space density of $0.97 \times 10^{-3} \text{ pc}^{-3}$. For the 750–900 K bin, we last reach $\langle V/V_{\text{max}} \rangle \approx 0.5$ at $d = 17.0$ pc, and there are 30 objects out to this distance, for a space density of $1.46 \times 10^{-3} \text{ pc}^{-3}$. For the 600–750 K bin, we last reach $\langle V/V_{\text{max}} \rangle \approx 0.5$ at $d = 16.0$ pc, and there are 53 objects out to this distance, for a space density of $3.09 \times 10^{-3} \text{ pc}^{-3}$. For the 450–600 K bin, we last reach $\langle V/V_{\text{max}} \rangle \approx 0.5$ at $d = 12.5$ pc, and there are 32 objects out to this distance, for a space density of $3.91 \times 10^{-3} \text{ pc}^{-3}$. For the 300–450 K bin, we last reach $\langle V/V_{\text{max}} \rangle \approx 0.5$ at $d = 8.0$ pc, and there are 7 objects out to this distance, for a space density of $3.26 \times 10^{-3} \text{ pc}^{-3}$. We know that the 900–1050 K and 300–450 K bins are inadequately sampled over the entire temperature ranges, so the space densities in these two bins are lower limits only. We make no claims about the completeness limit of the 150–300 K bin since it has only one known object in it.

For the three bins that are completely sampled in temperature, we can calculate uncertainties on their space densities as follows. For the 750–900 K bin, a sample of 30 objects would still have a $\langle V/V_{\text{max}} \rangle$ value within the 1σ envelope at $d = 18.0$ pc, as shown by the dotted gray line in the 750–900 K panel of Figure 15. For 30 objects, the space density for this distance would be $1.23 \times 10^{-3} \text{ pc}^{-3}$. For the 600–750 K bin, a sample

of 53 objects would still have a $\langle V/V_{\text{max}} \rangle$ value within the 1σ envelope at $d = 17.0$ pc, corresponding to a space density of $2.58 \times 10^{-3} \text{ pc}^{-3}$. For the 450–600 K bin, a sample of 32 objects would still have a $\langle V/V_{\text{max}} \rangle$ value within the 1σ envelope at $d = 13.5$ pc, corresponding to a space density of $3.10 \times 10^{-3} \text{ pc}^{-3}$. We adopt the difference between the space density at $\langle V/V_{\text{max}} \rangle \approx 0.5$ (from the previous paragraph) and that derived from the edge of the 1σ envelope (in this paragraph) to be the 1σ uncertainty in the space density measurement.

We can also use another method to determine when our measured value of $\langle V/V_{\text{max}} \rangle$ is significantly different from 0.5, given the size of our sample. We take the completeness limit, d_{max} , and sample size, N , judged from our analysis above and determine what the 1σ variation in $\langle V/V_{\text{max}} \rangle$ would be via Monte Carlo trials. The simulation assumes that the sample is complete and uniformly but randomly distributed within d_{max} . We generate a population of N objects within d_{max} by simply drawing N random numbers from a uniform distribution and converting them into distances $d_i = n_i^{1/3} d_{\text{max}}$, where i runs from 1 to N , d_i is the distance to the i th object, and n_i is the i th random number between 0 and 1. We then compute the $\langle V/V_{\text{max}} \rangle$ of this synthetic sample as a function of distance. We repeat the above process 10,000 times and at each distance take the standard deviation of the resulting distribution of $\langle V/V_{\text{max}} \rangle$ as our measure of the 1σ value variation from the ideal value of $\langle V/V_{\text{max}} \rangle = 0.5$. These standard deviations are plotted in brown on Figure 15. In general, these variations are smaller than the ones determined by our method above. However, the Monte Carlo method assumes a completeness at a set distance and predicts the variations likely to be seen at smaller distances. The previous method, on the other hand, predicts the likelihood of a uniform sample at each distance interval given the number of objects internal to that distance. Because it is a more direct measurement, we will continue to use the previous method to judge our completeness limits, and we further note that it also gives us more conservative estimates on our uncertainties.

Now that we have judged completeness in distance, we must further judge whether the sky distribution itself indicates a deficiency of objects toward the Galactic Plane. If we divide the hemisphere into eight equal-area slices cut along lines of constant $b = 0^\circ 00, \pm 14^\circ 47, \pm 30^\circ 00, \text{ and } \pm 48^\circ 59$ (Galactic coordinates for each object are given in column 6 of Table 11), we find 23, 24, 23, 10, 11, 17, 23, and 21 objects starting with the northernmost piece and ending with the southernmost. Indeed, there is a clear deficit concentrated toward the Galactic Plane. To account for this deficit, we multiply our derived space density values by $(4/3)(\text{total number with } |b| > 14^\circ 47)/(\text{total number at all } b \text{ values}) = (4/3)(131)/152 = 1.15$ to account for the missing objects toward the Plane. With this correction factor in hand, we derive our adopted space densities and their uncertainties as listed in Table 12.

9.3.2. Early- to Mid-L Dwarfs

Because our mass function simulations predict only relative space densities, our best metric for determining which simulation T_{eff} distributions best fit the data would be to have another set of space densities measured in a temperature range far removed from the late-T and Y dwarfs. The Baraffe et al. (2003) and Saumon & Marley (2008) models are both valid

Table 14
Analysis of the 20 pc Census for $1500 < T_{\text{eff}} < 2100$ K

T_{eff} Range (K)	Type Range Field obj.	Type Range Young obj.	Total Number	Completeness of <i>Gaia</i> DR2 ^a
(1)	(2)	(3)	(4)	(5)
1950–2100	L1, L1.5	L0, L0.5, L1	19	89%
1800–1950	L2, L2.5	L1.5, L2, L2.5	16	94%
1650–1800	L3, L3.5, L4	L3, L3.5	21	100%
1500–1650	L4.5, L5, L5.5	L4	26	81% ^b

Notes.

^a This is the percentage of objects with parallaxes listed in the Second Data Release from *Gaia*.

^b Note that only Gl 779A, not the L dwarf companion Gl 779B, is listed in *Gaia* DR2.

between 300 and 2500 K, so we will determine space densities for objects at the upper end of this T_{eff} range.

Objects at 2500 K land near the boundary between late-M dwarfs and early-L dwarfs (see Figure 9.19 of Gray & Corbally 2009). Fortunately, we can create a complete, volume-limited census of early- to mid-L dwarfs with reasonable ease, in no small part because these objects are much rarer than their late-T and Y brethren. We used the update to the data underlying the DwarfArchives compilation of published L, T, and Y dwarfs (see Section 3) to extract the list. All objects having either an optical or a near-infrared type from L0 to L5 were retained. Those with pre-*Gaia* parallaxes placing them within 20 pc of the Sun were kept. For the rest, we used the compiled J , H , and $W2$ magnitudes along with their spectral types to compute spectrophotometric distance estimates using the spectral type to absolute magnitude relations presented in Filippazzo et al. (2015) for field dwarfs and in Faherty et al. (2016) for low-gravity (young) dwarfs, whichever was applicable based on the spectral type. In order to ensure a complete 20 pc sample, we retained all objects having distance estimates of < 23 pc. We then consulted *Gaia* DR2 to obtain parallaxes of these objects and dropped any whose *Gaia* data ruled out membership in the 20 pc sample. Of the ninety-one objects, only six lacked parallaxes from either *Gaia* DR2 or another published source.

The full list is presented in Table 13. We list the discovery name and coordinates in column 1, the discovery reference in column 2, the adopted parallax and reference in columns 3 and 4, the optical spectral type and reference in columns 5 and 6, the near-infrared spectral type and reference in columns 7 and 8, approximate Galactic coordinates in column 9, and the final adopted type (for use in the discussion below) in column 10. Column 11 gives the T_{eff} bin into which each object is mapped, as discussed further below.

The adopted spectral types were determined as follows. For field objects, we averaged the optical and near-infrared types, but rounded any decimal type from Bardalez Gagliuffi et al. (2014) to its nearest half-type beforehand. For those averages landing at a quarter or three-quarters type, we chose the closest half type that fell in the direction of the optical value. For young objects, the optical type is used as the adopted type, unless only the near-infrared type is noted as low-gravity, in which case the averaging used above for the field objects is employed.

As was done with the late-T and Y dwarfs in the last section, we need to place these objects on a T_{eff} scale. Faherty et al. (2016) provide a mapping from spectral type to T_{eff} for the L dwarfs. They find that this mapping depends upon the age of the L dwarf. In the early- to mid-L dwarf range, young (low-gravity), higher-mass L dwarfs have slightly colder T_{eff} values compared to old field L dwarfs of the same spectral subclass (see their Figure 33). We note that the Faherty et al. (2016) spectral-type relation (which is the same one determined in Filippazzo et al. 2015) for field L dwarfs gives a ~ 150 K range for each full spectral class at early L, but this shrinks to ~ 100 K per full spectral class by mid-L. As shown in Table 14, we thus map field spectral types into T_{eff} as follows: L1–L1.5 is mapped to the 1950–2100 K bin, L2–L2.5 to 1800–1950 K, L3–L3.5–L4 to 1650–1800 K, and L4.5–L5–L5.5 to 1500–1650 K.

The adopted types of the young, low-gravity L dwarfs are mapped to T_{eff} using the “YNG” relations of Faherty et al. (2016).²⁷ Specifically, the mapping into our 150 K bins is L0–L0.5–L1 for 1950–2100 K, L1.5–L2–L2.5 for 1800–1950 K, L3–L3.5 for 1650–1800 K, and L4 for 1500–1650 K. Note that the young L dwarfs of type L4.5 and later from Table 13 fall in a cooler bin for which later-type field L dwarfs ($\geq L6$) are expected to have poorer coverage out to 20 pc by *Gaia*. Likewise, old field objects in Table 13 that are earlier in type than L0 share a temperature bin containing low-gravity late-M dwarfs, which we have not tabulated because DwarfArchives does not track objects with M dwarf types. Hence, not all objects in Table 13 were used in the space density arguments that follow.

In Table 14 we list the aforementioned mapping of types into each 150 K bin along with the number of objects found in each range. Because these objects were drawn from the literature using ground-based parallaxes and spectrophotometric distance estimates, we can use them to check the completeness of the *Gaia* DR2 sample over our spectral type and distance range. Overall we find that DR2 is 90% complete for early- to mid-L dwarfs within 20 pc, with the completeness dropping (slightly) at later types as expected, since *Gaia* has reduced sensitivity to those colder objects.

Figure 16 shows the results of our $\langle V/V_{\text{max}} \rangle$ test on this L dwarf sample. In all four temperature bins, we are within 1σ of the expected $\langle V/V_{\text{max}} \rangle$ value of 0.5 at $d = 20.0$ pc, giving space densities of $0.57 \times 10^{-3} \text{ pc}^{-3}$ (19 objects) for the 1950–2100 K bin, $0.48 \times 10^{-3} \text{ pc}^{-3}$ (16 objects) for the 1800–1950 K bin, $0.63 \times 10^{-3} \text{ pc}^{-3}$ (21 objects) for the 1650–1800 K bin, and $0.78 \times 10^{-3} \text{ pc}^{-3}$ (26 objects) for the 1500–1650 K bin. The values of $\langle V/V_{\text{max}} \rangle$ are still within the 1σ envelope at 23.0, 22.0, 21.0, and 21.0 pc for the four bins, giving densities of $0.37 \times 10^{-3} \text{ pc}^{-3}$, $0.36 \times 10^{-3} \text{ pc}^{-3}$, $0.54 \times 10^{-3} \text{ pc}^{-3}$, and $0.67 \times 10^{-3} \text{ pc}^{-3}$. We use the differences between these latter densities and the ones at our 20 pc limit as the 1σ uncertainties in our measurements. These values are listed in Table 12 along with the ones measured earlier for the late-T and Y dwarfs.

Unlike for the late-T and Y dwarfs, we find that this sample has no obvious incompleteness along the Galactic Plane. Because of the poorer statistics, we divide the celestial sphere into only four equal-area pieces sliced along lines of constant b values of $+30^\circ$, 0° , and -30° . (Galactic coordinates for

²⁷ Note that in Table 19 of Faherty et al. (2016), the coefficients of the T_{eff} YNG relation are accidentally listed in reverse order. Coefficient c_0 is actually c_4 , c_1 is actually c_3 , etc.

Table 15
Data in Support of Figures 15 and 16

Dist. (pc)	Number($\langle V/V_{\max} \rangle^a$)								
	1950– 2100 K (2)	1800– 1950 K (3)	1650– 1800 K (4)	1500– 1650 K (5)	900– 1500 K (6)	750– 900 K (7)	600– 750 K (8)	450– 600 K (9)	300– 450 K (10)
4.0	2(0.82)
4.5	2(0.57)	1(0.77)	...
5.0	3(0.60)	2(0.69)	1(0.84)
5.5	4(0.54)	...	2(0.91)	2(0.52)	1(0.63)
6.0	4(0.42)	3(0.92)	4(0.77)	2(0.40)	3(0.78)
6.5	6(0.52)	3(0.72)	4(0.60)	2(0.31)	6(0.77)
7.0	7(0.48)	3(0.58)	5(0.57)	3(0.45)	6(0.61)
7.5	7(0.39)	3(0.47)	6(0.53)	5(0.60)	6(0.50)
8.0	7(0.32)	4(0.50)	7(0.52)	6(0.57)	7(0.48)
8.5	7(0.27)	6(0.59)	8(0.49)	7(0.53)	8(0.45)
9.0	7(0.23)	7(0.56)	8(0.41)	8(0.51)	8(0.38)
9.5	7(0.19)	7(0.48)	11(0.50)	12(0.59)	8(0.33)
10.0	7(0.16)	7(0.41)	12(0.47)	14(0.56)	10(0.42)
10.5	7(0.14)	8(0.43)	12(0.40)	22(0.64)	10(0.36)
11.0	10(0.37)	11(0.52)	14(0.43)	26(0.61)	10(0.32)
11.5	1(0.94)	1(0.88)	3(0.74)	4(0.46)	10(0.32)	11(0.46)	18(0.50)	27(0.55)	10(0.28)
12.0	1(0.83)	4(0.90)	6(0.79)	5(0.50)	10(0.29)	11(0.40)	24(0.57)	28(0.50)	10(0.24)
12.5	2(0.85)	4(0.79)	7(0.74)	8(0.62)	10(0.25)	12(0.40)	25(0.52)	32(0.50)	10(0.22)
13.0	2(0.75)	4(0.70)	9(0.72)	10(0.63)	10(0.22)	15(0.47)	31(0.56)	33(0.46)	10(0.19)
13.5	2(0.67)	4(0.63)	10(0.67)	10(0.56)	11(0.27)	18(0.51)	34(0.54)	35(0.44)	11(0.24)
14.0	3(0.71)	5(0.65)	10(0.60)	10(0.50)	12(0.30)	19(0.49)	36(0.51)	38(0.44)	11(0.22)
14.5	4(0.72)	5(0.58)	10(0.54)	11(0.50)	16(0.44)	20(0.46)	38(0.48)	39(0.41)	11(0.19)
15.0	5(0.71)	5(0.53)	11(0.53)	11(0.45)	16(0.40)	22(0.47)	43(0.50)	40(0.39)	11(0.18)
15.5	5(0.64)	7(0.61)	11(0.48)	12(0.45)	16(0.36)	24(0.47)	48(0.51)	42(0.38)	12(0.22)
16.0	6(0.64)	8(0.60)	12(0.48)	12(0.41)	18(0.39)	24(0.43)	53(0.51)	43(0.36)	12(0.20)
16.5	7(0.64)	10(0.63)	13(0.48)	14(0.46)	19(0.39)	27(0.45)	54(0.47)	43(0.33)	12(0.18)
17.0	8(0.63)	10(0.57)	14(0.48)	17(0.52)	20(0.39)	30(0.47)	54(0.43)	43(0.30)	12(0.17)
17.5	10(0.65)	11(0.56)	14(0.44)	17(0.47)	22(0.41)	31(0.44)	58(0.43)	45(0.31)	12(0.15)
18.0	11(0.63)	12(0.55)	15(0.44)	19(0.49)	22(0.37)	31(0.41)	61(0.43)	47(0.31)	12(0.14)
18.5	15(0.68)	12(0.51)	18(0.50)	19(0.45)	24(0.40)	34(0.43)	61(0.39)	47(0.29)	12(0.13)
19.0	16(0.65)	13(0.51)	20(0.51)	23(0.51)	28(0.45)	35(0.41)	63(0.38)	47(0.26)	12(0.12)
19.5	17(0.62)	14(0.50)	20(0.47)	24(0.49)	28(0.42)	36(0.40)	64(0.36)	49(0.27)	13(0.18)
20.0	19(0.62)	16(0.53)	21(0.46)	26(0.50)	28(0.39)	38(0.40)	67(0.36)	49(0.25)	13(0.16)
20.5	19(0.57)	16(0.49)	21(0.43)	26(0.46)	28(0.36)	38(0.37)	67(0.34)	49(0.23)	13(0.15)
21.0	19(0.53)	16(0.45)	21(0.40)	26(0.43)	28(0.34)	38(0.34)	67(0.31)	49(0.22)	13(0.14)
21.5	19(0.50)	16(0.42)	21(0.37)	26(0.40)	28(0.31)	38(0.32)	67(0.29)	49(0.20)	13(0.13)
22.0	19(0.46)	16(0.40)	21(0.35)	26(0.37)	28(0.29)	38(0.30)	67(0.27)	49(0.19)	13(0.12)
22.5	19(0.43)	16(0.37)	21(0.33)	26(0.35)	28(0.27)	38(0.28)	67(0.26)	49(0.18)	13(0.11)
23.0	19(0.41)	16(0.35)	21(0.30)	26(0.33)	28(0.26)	38(0.26)	67(0.24)	49(0.17)	13(0.11)
23.5	19(0.38)	16(0.32)	21(0.29)	26(0.31)	28(0.24)	38(0.25)	67(0.22)	49(0.16)	13(0.10)
24.0	19(0.36)	16(0.30)	21(0.27)	26(0.29)	28(0.22)	38(0.23)	67(0.21)	49(0.15)	13(0.09)
24.5	19(0.34)	16(0.29)	21(0.25)	26(0.27)	28(0.21)	38(0.22)	67(0.20)	49(0.14)	13(0.09)
25.0	19(0.32)	16(0.27)	21(0.24)	26(0.25)	28(0.20)	38(0.20)	67(0.19)	49(0.13)	13(0.08)

Note.

^a For each temperature bin listed, the first value is the number of objects out to the distance given in column (1), and the second value (in parentheses) is the value of $\langle V/V_{\max} \rangle$ for objects out to that distance.

each object are given in column 9 of Table 13.) We find 25, 25, 14, and 16 objects starting with the northernmost piece and ending with the southernmost. This shows that our 20 pc sample of early-L dwarfs lacks an obvious zone of avoidance in the Galactic Plane because 39/80 = 49% of the sources are concentrated in the 50% of the sky closest to the Plane itself. We can thus assume that the 20 pc sample of 1500–2100 K dwarfs is reasonably complete both sky-wide and to the full 20 pc distance limit. Therefore, no adjustment factor (see Table 12) to the measured space densities is needed.

9.3.3. A Uniform Distribution of the Nearest Brown Dwarfs

Bihain & Scholz (2016) have posited that the distribution of nearby brown dwarfs on the sky is astonishingly non-uniform. Those authors claim that most of the brown dwarfs with the 6.5 pc volume (21 out of 26 objects) are leading the Sun in its Galactic orbit, with only a handful (the remaining 5) trailing the Sun. They further state that the probability of such a distribution occurring by chance is 0.098%, although the 2σ error bar on this quantity pushes it as high as 11%. They conjecture that the literature sample of brown dwarfs within 6.5

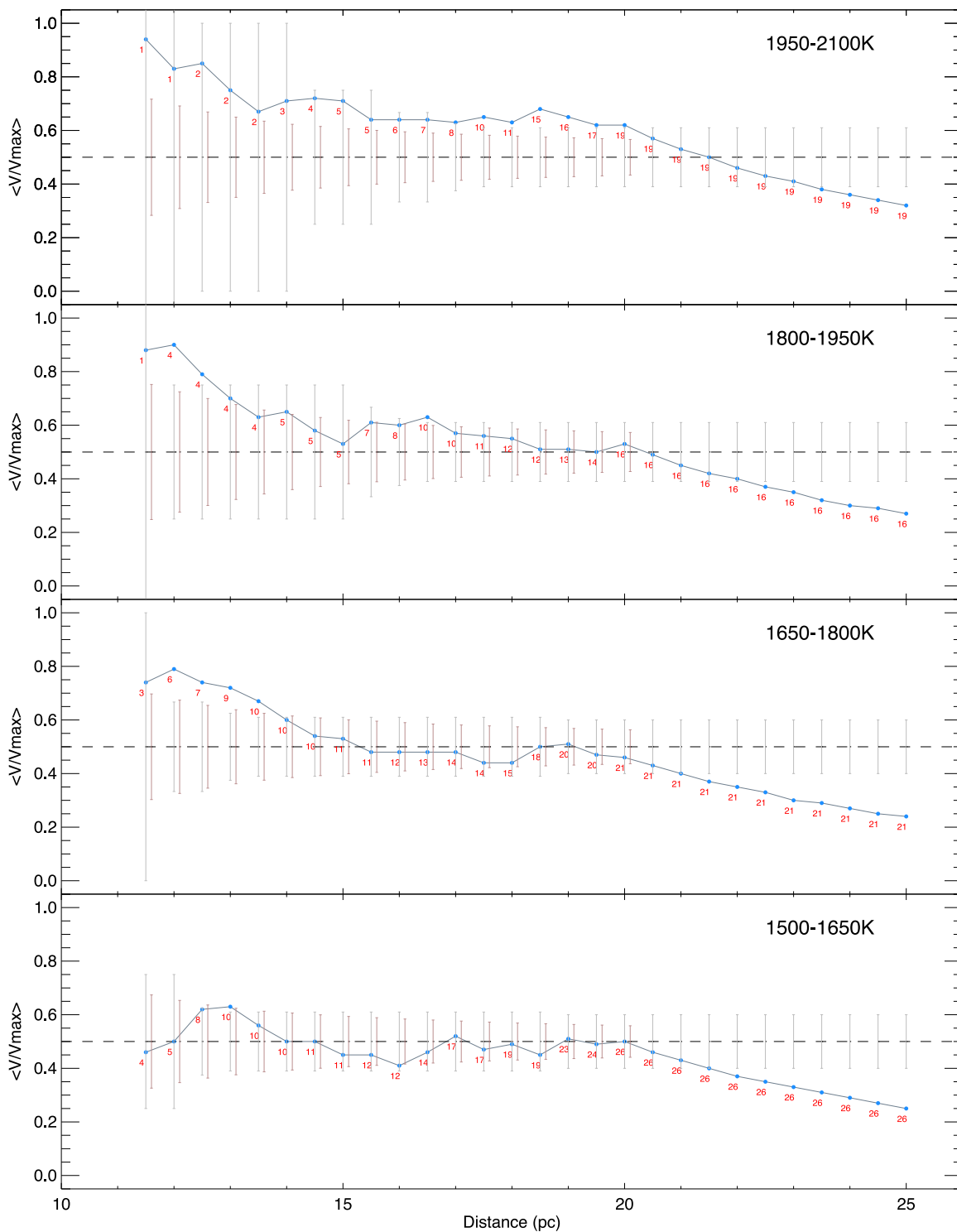


Figure 16. Average V/V_{\max} value in 0.5 pc intervals for the four 150 K bins encompassing our 20 pc early- to mid-L sample. See the caption to Figure 15 for more details. (Data in support of this figure can be found in Table 15.)

pc is incomplete due to biases in the methodology being employed to search the all-sky 2MASS and *WISE* data sets, although the ways in which the search criteria might have created such an odd bias are not clearly specified. Alternatively, they suggest that if the sample is complete, or nearly so, it is either caused by some “random inhomogeneity” or an unknown dynamical mechanism causing brown dwarfs to segregate from stars in this manner, as the stellar sample (136 objects within 6.5 pc) shows no such asymmetric distribution.

We show here, using a sample ~ 6 times larger, that nearby brown dwarfs are distributed uniformly and that the Bihain & Scholz (2016) observation is solely the result of the statistics of small numbers. To demonstrate this, we employ our sample of 1500–2100 K and 450–900 K objects used in the space density measurements of Table 12. The warmer group of objects is comprised of early- to mid-L dwarfs, which includes some low-mass stars as well as brown dwarfs, and the cooler group is comprised of late-T to Y dwarfs, all of which are brown dwarfs.

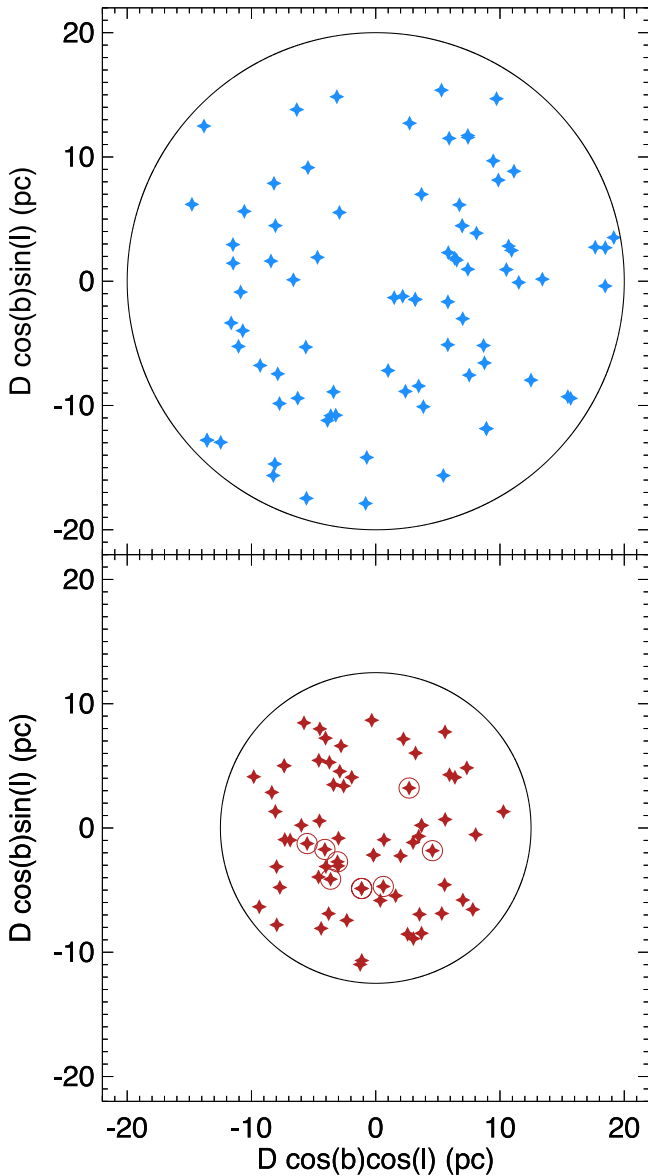


Figure 17. Galactic projection plot identical to that in Figure 1 of Bihain & Scholz (2016) showing the distributions of our two samples. The upper panel shows the 1500–2100 K sample (82 objects) out to our completeness limit of 20 pc, and the lower panel shows the 450–900 K sample (69 objects) out to our completeness limit of 12.5 pc. Objects within 6.5 pc of the Sun are circled individually; no such objects appear in the upper panel.

We note also that we have not added any new objects to these samples that were not already in the 6.5 pc accounting of Bihain & Scholz (2016), with the exception of considering 2MASS 0939–2448 to be an unresolved double (see Section 8.2). Figure 17 shows the sky distribution of these objects on a Galactic projection identical to that used in Figure 1 of Bihain & Scholz (2016). For the 1500–2100 K objects, we use the entire sample out to 20 pc since we believe that to be relatively complete, and for the 450–900 K objects we use only the subsample out to 12.5 pc since the coolest sub-bin (450–600 K) is complete only out to that distance.

Both sets of objects are distributed so that roughly equal numbers are seen in the upper and lower halves of the diagram. We circle objects falling within the same 6.5 pc distance used by Bihain & Scholz (2016) to show that these objects appear,

as those authors noted, primarily in the lower half of the diagram. (Note that *none* of the objects in the 1500–2100 K range fall within 6.5 pc.) However, this is a result of random statistics on a small sample, as the larger sample shows no such effect. It is very difficult to imagine a selection effect or a dynamical process at work within the 6.5 pc distance that would not also be operating in the distance range from 6.5 to 12.5 pc.

9.3.4. Best Fits to the Space Densities

We can now test which of the 72 models in Figures 12 and 13 best match our measured space densities. We use the IDL routine `mpfit` (Markwardt 2009) to perform a weighted least-squares fit between the data and the model where the only adjustable parameter is the scaling between the arbitrary number counts in the models and our measured space densities. For the calculation, we use only the seven values in Table 12 with measured uncertainties (four in the 1500–2100 K range and three in the 450–900 K range) and ignore the ranges in which we have only lower limits (900–1050 K and 300–450 K) and the range in which we have only one data point and no measurable space density (150–300 K).

The best fit to each model produces a reduced χ^2 value, and we illustrate in Figure 18 the fits for which this value is minimized. For mass functions paired with the evolutionary code of Baraffe et al. (2003), the best fits are given by the power-law mass function with $\alpha = 0.5$ (model D). The single-object log-normal mass function of Chabrier (2001) (model H) is the next best model, although it consistently underpredicts the space densities seen in the 300–750 K range. If we consider the lower limit to the space density in the 300–450 K bin, we find that for the power-law model there is a preference for the lower-mass cutoffs, with the current data favoring a cutoff no higher than $\sim 5M_{\text{Jup}}$. The other power-law mass functions produced poorer reduced χ^2 values of ~ 7.8 , ~ 5.2 , ~ 3.0 , ~ 3.0 , and ~ 6.2 for α values of -1.0 , -0.5 , 0.0 , $+1.0$, and $+1.5$ (models A, B, C, E, and F), respectively. The other log-normal mass functions give reduced χ^2 values of ~ 3.8 and ~ 3.2 for models G and I, respectively. The bi-partite power-law mass functions of Kroupa et al. (2013) give much larger reduced χ^2 values of ~ 7.2 , ~ 4.1 , and ~ 10.2 for models J, K, and L, respectively.

For mass functions paired with the evolutionary code of Saumon & Marley (2008), we find even better fits. As with the Baraffe et al. (2003) models, the best fits are given by the power-law mass function with $\alpha = 0.5$ (model D), with the single-object log-normal mass function of Chabrier (2001) (model H) being only slightly worse. The log-normal function again underpredicts the space densities in the 300–750 K range. The $\alpha = 0.5$ power law suggests that the cutoff mass is likely no higher than $\sim 5M_{\text{Jup}}$ given our measured lower limit to the space density in the 300–450 K bin. The other power-law mass functions produced poorer reduced χ^2 values of ~ 8.7 , ~ 5.7 , ~ 3.1 , ~ 2.4 , and ~ 5.6 for α values of -1.0 , -0.5 , 0.0 , $+1.0$, and $+1.5$ (models A, B, C, E, and F), respectively. The other log-normal mass functions give reduced χ^2 values of ~ 2.0 and ~ 3.1 for models G and I, respectively, showing that the log-normal function of Chabrier (2003a) (model G) produces almost as good a match to the observed data as that from Chabrier (2001) (model H). The bi-partite power-law mass functions of Kroupa et al. (2013) give much larger reduced χ^2

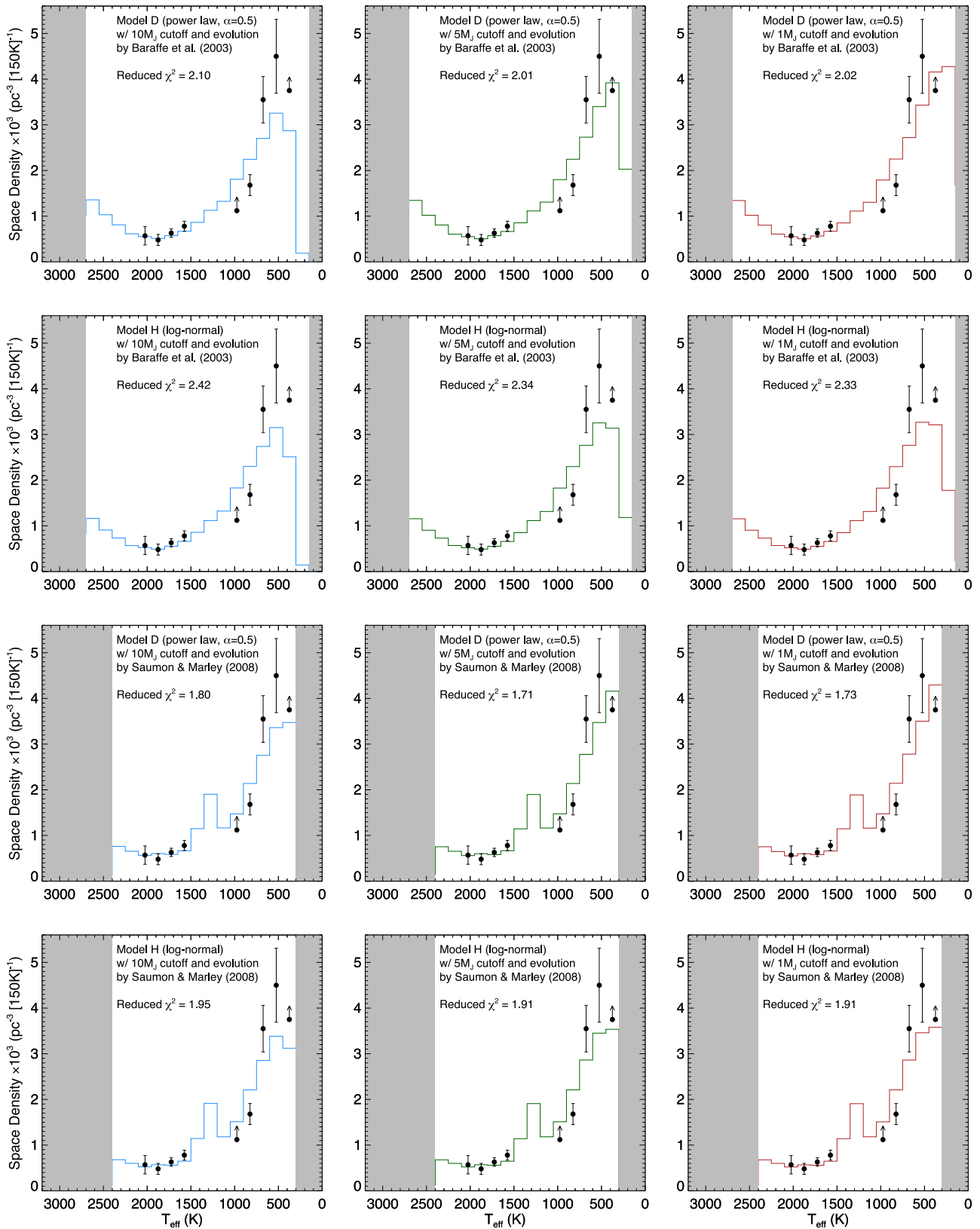


Figure 18. Best fits between the simulations of Figures 12 and 13 and our measured space densities in Table 12. The top two rows show the two mass functions using the Baraffe et al. (2003) evolutionary code that provide the smallest reduced χ^2 values: the power law with $\alpha = 0.5$ (top row; Model D) and the single-object log-normal from Chabrier (2003a) (second row; Model G). Similarly, the bottom two rows show the two mass functions using the Saumon & Marley (2008) evolutionary code that provide the smallest reduced χ^2 values: the power law with $\alpha = 0.5$ (third row; Model D) and the single-object log-normal from Chabrier (2003a) (bottom row; Model H). In each row the mass functions are shown with assumed low-mass cutoffs of $10M_{\text{Jup}}$ (blue, left panels), $5M_{\text{Jup}}$ (dark green, middle panels), and $1M_{\text{Jup}}$ (red, right panels). Our measured spaced densities and their uncertainties are shown in black on each panel.

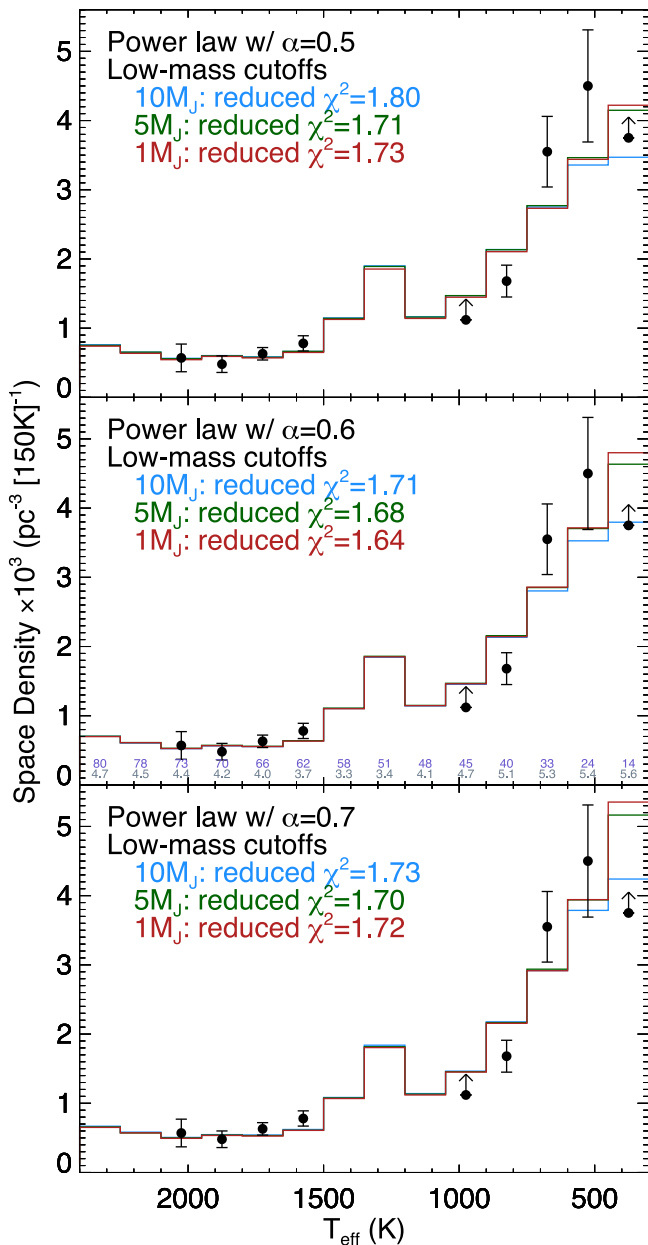


Figure 19. Fits of power laws with α values of 0.5 (top panel), 0.6 (middle panel), and 0.7 (bottom panel) to our observational data (black points). These predicted T_{eff} distributions have been passed through the evolutionary models of Saumon & Marley (2008). Each panel shows simulations for each of three low-mass cutoffs: $10 M_{\text{Jup}}$ (blue), $5 M_{\text{Jup}}$ (green), and $1 M_{\text{Jup}}$ (red). The minimum reduced χ^2 value is found for the $\alpha = 0.6$ model. For the $\alpha = 0.6$ model with $5 M_{\text{Jup}}$ cutoff, we have also calculated the mean mass and mean age in each T_{eff} bin. These values are shown in the middle panel; the mean mass is shown in units of M_{Jup} (upper value in purple), and the mean age is shown in units of Gyr (lower value in gray).

values of ~ 12.0 , ~ 8.8 , and ~ 14.6 for models J, K, and L, respectively.

Three other points should be noted regarding these preliminary results:

1. As mentioned earlier, there is a clear discriminator present in the 1050–1500 K range of the simulations that will determine whether the Baraffe et al. (2003) or Saumon & Marley (2008) evolutionary models are preferred, from the point of view of the mass function.

In the six lower panels of Figure 18 based on the Saumon & Marley (2008) models, there is a clear overdensity relative to a simple interpolation between the space densities seen in the 750–900 K and 1500–1650 K bins that is not present in the six upper panels based on the Baraffe et al. (2003) models. Using a literature update by CRG to the known L and T dwarfs archived at DwarfArchives along with spectrophotometric distance estimates to those still lacking parallax determinations, we find strong evidence that this overdensity is, indeed, present. This can be tested with a large, volume-limited sample of objects in this temperature range, which both the ground-based parallax program of Best et al. (2018) and the Cycle 14 *Spitzer* program 14000 (PI: Kirkpatrick) are currently aiming to do.

2. There is a dramatic difference, slightly over a factor of two, in our measured space densities between the 750–900 K bin and the 600–750 K bin. The predictions, even in our best fits, are unable to model this effect. Is this effect real or an artifact of our transformation to T_{eff} ? This rapid rise in space density with falling temperature is also seen in the distribution by spectral type. Our late-T dwarf sample in Table 11 shows 34 T7–T7.5 dwarfs but a surprisingly larger number (64) of T8–T8.5 dwarfs. Performing a V/V_{max} test on these objects shows that the earlier spectral types are complete to 13.5 pc with 18 objects; the later spectral types are complete to 13.5 with 34 objects. The difference in these space densities is almost a factor of two ($1.89\times$), paralleling the effect seen when binning by T_{eff} .

We can also examine this effect in other quantities. Figure 14 suggests that between 600 and 900 K, M_H runs from ~ 16 to 18 mag. If we divide the absolute magnitude range into two portions, $16 \leq M_H < 17$ mag and $17 \leq M_H < 18$ mag, we find 34 objects in the brighter bin and 43 objects in the fainter one. Performing a simple V/V_{max} test finds that the brighter bin is complete to ~ 15.5 pc with 28 objects; the fainter bin is complete to ~ 13.0 pc with 20 objects. In this case, the space density of the fainter bin is only 1.21 times higher than that of the brighter bin. We can perform a similar exercise on ch1–ch2 color, for which Figure 14 shows that a color span of 1.2 to 2.0 mag corresponds to T_{eff} values of 900 K down to 600 K. We find 49 T dwarfs with $1.2 \leq \text{ch1} - \text{ch2} < 1.6$ mag and 61 with $1.6 \leq \text{ch1} - \text{ch2} < 2.0$ mag. Performing a simple V/V_{max} test finds that the bluer bin is complete to ~ 14.5 pc with 25 objects; the redder bin is complete to ~ 13.5 pc with 35 objects. In this case, the space density of the redder bin is $1.73\times$ higher than that of the bluer bin.

We conclude that the jump in space density from 750–900 K to 600–750 K is likely real since it appears in other physical quantities like spectral type and color, although less so with absolute magnitude. The fact that this jump appears not to be well modeled by the predicted mass functions plus evolutionary code may suggest that the Solar Neighborhood has an unusual distribution of T dwarfs relative to the Milky Way as a whole, but this seems at odds with the fact that this peculiarity in the space densities occurs at the point where we have our largest number of objects and hence our best statistical measurement. It is possible, then, that the discrepancy

with respect to predictions is real and points to missing physics in the evolutionary models.

- As the three panels in the top row of Figure 18 indicate, improving the space density measurement in the 300–450 K bin as well as providing a robust lower limit to the density in the 150–300 K bin would better help determine the low-mass cutoff of the mass function as the simulations show vast differences in the predicted numbers in these ranges. Current work to find more of these Y dwarfs, which at these temperatures are typically those classified as Y1 and later, is currently underway using proper motion searches afforded by the long time baseline (seven-plus years) now available between the classic *WISE* and *NEOWISE* Reactivation missions. The prospect for discovering more of these objects looks promising based on early results from the Backyard Worlds Citizen Science project (Kuchner et al. 2017) and CatWISE (Meisner et al. 2018), but characterizing the spectra of such discoveries and measuring accurate distances will be challenging given the extreme faintness of these objects. (See Section 11 for more discussion on this point.)

Given the success of fitting our observational data to the power-law model with $\alpha = 0.5$, we searched for even better fits using a smaller grid spacing (increments of 0.1) for α . We find that the $\alpha = 0.6$ version using the evolutionary models of Saumon & Marley (2008) results in the lowest overall reduced χ^2 , as illustrated in Figure 19. The fits to the 1 and 5 M_{Jup} cutoffs are slightly better than the one for the 10 M_{Jup} cutoff. If we assume, based on the T_{eff} determinations in Table 11, that our coldest bin on Figure 19 is reasonably complete to $T_{\text{eff}} \approx 350$ K, then the simulations predict a mean mass of 16 M_{Jup} with standard deviation of 5 M_{Jup} . (See the figure for the mean mass and age in each T_{eff} bin.) It should also be stated again that the next coldest bin—the 150–300 K bin just off the right side of the plot—has only one known object, WISE 0855–0714, whose mass has been estimated at 3–10 M_{Jup} (Luhman 2014a). Thus, our observations are already beginning to measure the field mass function into the regime below the deuterium-burning limit of $\sim 13M_{\text{Jup}}$.

10. Discussion

The fitting of our measured space densities to the suite of simulated T_{eff} distributions in Section 9.3.4 was focused solely on the substellar regime. Here we place these results in context with efforts that have attempted to describe the mass function across the entirety of star formation’s mass spectrum, from $\sim 100M_{\odot}$ to $\sim 1M_{\text{Jup}}$.

Specifically, early work by Salpeter (1955) suggested that the stellar mass function at very high masses could be adequately described by a power law with exponent $\alpha = 2.35$. Miller & Scalo (1979) found this same power law for $M > 10M_{\odot}$, but at lower masses favored a two-piece power law with exponents of $\alpha = 1.5$ for $1M_{\odot} < M < 10M_{\odot}$ and $\alpha = 0.4$ for $0.1M_{\odot} < M < 1M_{\odot}$. Kroupa (2001) prefers a three-piece power law in the stellar regime having segments with $\alpha \approx 2.3$ for $M > 1.0M_{\odot}$, $\alpha \approx 2.7$ for $0.5M_{\odot} < M < 1.0M_{\odot}$, and $\alpha \approx 1.8$ for $0.08M_{\odot} < M < 0.5M_{\odot}$, once the hidden members of unresolved binaries are properly accounted for. Chabrier (2003b) has suggested that over the entire stellar mass range ($\sim 100M_{\odot}$ to $\sim 0.1M_{\odot}$), the

mass function can be adequately described by either a log-normal or a two-segment power law.

With the discovery of brown dwarfs in both the field and young clusters, researchers have attempted to describe the mass function into the substellar regime. Kroupa et al. (2013) suggest that brown dwarfs form in a fundamentally different way from stars and that the mass function of brown dwarfs is a power law with $\alpha \approx 0.3$. However, they state that there is significant overlap in mass between the normal “stellar” portion (a power law with $\alpha \approx 1.3$) of the mass function and the “substellar” part but that the two pieces are discontinuous. Chabrier (2001), on the other hand, prefers a log-normal form, with values²⁸ of $\mu = \ln(0.10)$ and $\sigma = 0.627 \ln(10)$. These values were later revised to $\mu = \ln(0.079)$ and $\sigma = 0.69 \ln(10)$ by Chabrier (2003a) and later, as stated by Chabrier et al. (2014), to $\mu = \ln(0.25)$ and $\sigma = 0.55 \ln(10)$ by Chabrier (2005).

We find, however, that neither the Kroupa bi-partite power law nor the Chabrier log-normal forms adequately fit the data even when we allow for the vertical axis scaling (the space density) to be adjusted as a free parameter. Specifically, the Chabrier log-normal forms underpredict the number of objects below 650 K. Indeed, as Chabrier et al. (2014) note, their preferred values of μ and σ from Chabrier (2005) behave like a power law with a negative α value below $T_{\text{eff}} \approx 1300$ K. Using the two α values and their break points in mass as suggested by Kroupa et al. (2013), the bi-partite power laws fare even worse; however, these still hold promise, as the individual mass break points and α values can be fine tuned to provide better fits. This should be possible since our best-fit value of $\alpha \approx 0.6$ seems to describe the 350–2100 K portion of the T_{eff} distribution very well. As predicted by Hoffmann et al. (2018), the difference between a log-normal and power-law representation of the mass function at the smallest masses provides a powerful discriminant in distinguishing between formation theories.

Based on a theoretical perspective, Hennebelle & Chabrier (2008) argue that the full stellar + substellar mass function should be described as a power law at highest masses and a single log-normal form at lower masses. The same conclusion is reached via a somewhat different formalism by Hopkins (2012), although more recent theoretical considerations by Guszejnov et al. (2018) have raised questions about how both of these methods treat formation at the smallest masses. For these lowest-mass objects, the log-normal form implies a single “characteristic” mass governing their formation. Chabrier (2003a) argues that using multi-part power laws instead of a log-normal form to describe the mass function necessarily implies that multiple characteristic masses determine the processes of formation for low-mass objects. Multiple (or at least two) characteristic masses may, in fact, be necessary to describe the observational results for low-mass stars and brown dwarfs, as Kroupa et al. (2013) argue. A theoretical formalism for this alternate scenario has been described by Thies et al. (2010).

Finally, we caution that the *field* mass function is the result of formation processes that have occurred in different environments over the last ~ 10 Gyr. If the physics governing star formation in one environment is found to differ substantially from that in another, disentangling the physics from the resulting mixture may be extremely difficult. For example, the formation of brown dwarfs could be

²⁸ See the footnote in Section 9.1.2 regarding our translation of these μ and σ values into a natural logarithm form.

fundamentally different in a low-mass moving group such as the TW Hydrae Association than it is from that operating in a high-mass region such as the Orion Nebula Cluster, where oblation from O star winds and the higher potential for gravitational disruption of forming pre-stellar cores may play critical roles. (If so, such effects are likely to be seen only below $\sim 30M_{\text{Jup}}$ because Andersen et al. 2008 do not see strong evidence for environment-specific effects at higher masses.) The field mass function may, therefore, have utility only in predicting the outcome of galaxy-wide star formation, although it may eventually be used in determining the relative roles that each environmentally dependent process plays in the overall picture.

11. Conclusions and Future Plans

We have presented preliminary trigonometric parallaxes for 184 dwarfs with spectral types from T6 through early-Y. The vast majority of these, 142, come from a dedicated *Spitzer*/IRAC ch2 program, with the rest coming from programs at the USNO, NTT, and UKIRT. We use these parallaxes to produce a 20 pc sample with which we fit trends to various relationships between colors, spectral types, absolute magnitudes, and effective temperatures. We use these parallaxes to determine the distance limits at which our sample is complete for each of five 150 K wide bins ranging over $300 \text{ K} < T_{\text{eff}} < 1050 \text{ K}$. We also take a sample of early- to mid-L dwarfs from the literature, supplemented with recent *Gaia* data, to produce a complete 20 pc sample across four hotter 150 K wide bins in the range $1500 \text{ K} < T_{\text{eff}} < 2100 \text{ K}$. We compute the observed space densities in these bins and compare to simulations using various forms of the mass function passed through different evolutionary code—either Baraffe et al. (2003) or Saumon & Marley (2008)—to produce predicted distributions as a function of T_{eff} . Fits of our sample to these simulations show that a power law with $\alpha = 0.6$ provides the best match. Functions involving log-normal forms do not fit the observed space densities well at the lowest temperatures and lowest masses. We find that simulations with low-mass cutoffs of $10 M_{\text{Jup}}$ underpredict the number of objects in these same bins, with which we conclude that the low-mass cutoff for star formation, if there is one, must be lower than $\sim 5 M_{\text{Jup}}$, a result corroborated by analysis of the low-mass constituents in nearby young clusters (e.g., Luhman et al. 2016). Obtaining this result for the *field* substellar distribution, however, confirms that the formation of objects this low in mass is not a recent phenomenon but has been occurring over the lifetime of the Milky Way. The predicted mean age (see Figure 19) of objects in the 300–450 K, for example, is 5.6 Gyr for a mean mass of $14 M_{\text{Jup}}$.

These new results represent a vast improvement upon our previous attempt (Kirkpatrick et al. 2012) to derive the shape of the low-mass end of the mass function for several reasons: (1) There have been six additional years of follow-up by the entire community of brown dwarf researchers to uncover late-T and Y dwarfs in the solar neighborhood, so we have benefited in this paper from a larger sample of objects. (2) Rather than using measured parallaxes for a handful of objects (42 late-T dwarfs and 7 Y dwarfs) and extending those via spectrophotometric distance estimates to the others, we now have actual trigonometric parallaxes for (almost) the entire sample—126 late-T dwarfs and 26 Y dwarfs. (3) With actual parallaxes in hand, we can eliminate unresolved interlopers that would fall

within our volume based on their spectrophotometric distances, and for objects still within the volume, we can better access which objects are likely to be unresolved binaries themselves. (4) We have created a new suite of mass function simulations, some tied to newer and more realistic evolutionary models, that better incorporate the complexities of cooling across the brown dwarf sequence. In Kirkpatrick et al. (2012), we concluded that the brown dwarf segment of the mass function most closely approximated a power law with $\alpha \approx 0.0$, but if we used a normalization based on the space density of low-mass *stellar* objects, this power law overpredicted our counts by a factor of two to three. In this paper, we fit the brown dwarf segment independently and find that a much steeper power law is indicated, with $\alpha \approx 0.6$. This number is much closer to the α values of the brown dwarf mass function found in the Pleiades (~ 0.6 ; Bouvier et al. 1998; Casewell et al. 2007) as well as other young clusters (typically ~ 0.5 ; see review by Luhman 2012) and star-forming regions ($\lesssim 0.5$; see review by Bastian et al. 2010).

We will be able to improve upon the results in this paper in several ways. The tabulated parallaxes and their uncertainties should continue to improve for our *Spitzer* sample of 142 targets as there is a final year of Cycle 13 observations currently underway. The measured parallaxes for objects in the USNO, NTT, and UKIRT parallax programs will also continue to improve, as those results presented here are also regarded as preliminary. For our *Spitzer* targets with large (>2) reduced χ^2 values in their astrometric fits, we will obtain an additional year of data in Cycle 14 to monitor whether the residuals in the fits show signs of periodicity related to unseen companions. In Cycle 14, we will also be acquiring astrometric data in IRAC ch2 of the 20 pc L dwarf sample in the missing 1050–1500 K T_{eff} interval of Table 12 as well as obtaining astrometry for those T dwarfs in Table 11 lacking parallax measurements. Other improvements for our continued analysis include the use of *Gaia* DR2 data to tie directly to the absolute astrometric reference frame for the individual *Spitzer* exposures, as parallactic solutions for most of our reference stars are available; this will obviate the need for a correction from relative to absolute astrometry at a later step. Moreover, as the community of nearby star researchers continues to scour the *Gaia* DR2 data, volume-limited samples of the omnipresent M dwarfs will finally become published out to ~ 20 pc or more, enabling us to check how the brown dwarf power-law segment found in this paper dovetails with the low-mass end of the field stellar mass function.

Most pressing, however, is the need to uncover even colder objects that will enable us to determine more accurately the low-mass cutoff of star formation and to discern if the power-law form continues to describe the observed space density at the coldest temperatures. In this regard, we need to complete the census of the coldest members in the 300–450 K bin, and find more objects that occupy the 150–300 K bin with WISE 0855–0714 (see Table 12). For this we need an all-sky data set probing wavelengths where these objects are brightest, and $\sim 5 \mu\text{m}$ images from *WISE* will likely be the only ones capable of providing that info for many years to come. Presently, two efforts are underway to discover more Y dwarfs using these data. The first is the Citizen Scientist project Backyard Worlds (Faherty et al. 2018) and the second is a NASA-funded ADAP proposal led by Peter Eisenhardt called CatWISE. Backyard Worlds is taking the unWISE coadds (Lang 2014;

Meisner et al. 2017a, 2017b) spanning several years of the *WISE* and *NEOWISE* missions and creating blinking coadds on which members of the public can identify moving objects. CatWISE is taking epochal versions of the unWISE coadds (Meisner et al. 2018) and running an AllWISE-style processing (Cutri et al. 2013; Kirkpatrick et al. 2014) on them to measure proper motions for all detected sources. For both, the main advantage over previous *WISE* data sets is that motions over a long, ~ 7 yr time baseline can now be used to uncover nearby objects, freeing selections from relying on color to identify cold objects that may be detected only weakly at *W2* and undetected in *W1*. (Previous motion searches with *WISE* data by Kirkpatrick et al. 2014, 2016; Luhman 2014b; Luhman & Sheppard 2014 and Schneider et al. 2016 were limited by a small 0.5 yr time baseline, shallow individual frame depths, or both.) Obtaining imaging and spectroscopic characterization of cold discoveries from both programs will be possible using current ground-based and space-based assets, although for the coldest discoveries, given their extreme faintness, obtaining spectra will likely have to wait for the launch of the *James Webb Space Telescope*. Sadly, once *Spitzer* ceases operations there will be no obvious instrumentation with which to obtain the much needed parallaxes for these discoveries. The astronomical community, and brown dwarf researchers in particular, will be left with a need that no planned future mission fulfills.





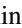


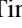
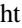
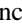



J.D.K. thanks the staff of the *Spitzer* Science Center for their assistance in making this project possible; Frank Masci, Lee Rottler, and Steve Schurr for programming advice; Yossi Shvartzvald and Sergio Fajardo-Acosta for lucrative discussions; and the anonymous referee and the U.S. Naval Observatory Editorial Board for comments that improved the paper. We also thank Trudy M. Tilleman and Justice E. Bruursema for their contributions to the USNO observing effort. We further thank David Ciardi for acquiring Keck/NIRC2 *H*-band imaging for WISE 0226–0211AB. Research by R.L.S. was supported by the 2015 Henri Chrétien International Research Grant administered by the American Astronomical Society. E.C.M. is supported by an NSF Astronomy and Astrophysics Postdoctoral Fellowship under award AST-1801978. A.J.C. gratefully acknowledges financial support through the Fellowships and Internships in Extremely Large Data Sets (FIELDS) Program, a National Aeronautics and Space Administration (NASA) science/technology/engineering/math (STEM) grant administered by the University of California, Riverside. F.M. is supported by an appointment to the NASA Postdoctoral Program at the Jet Propulsion Laboratory (JPL), administered by Universities Space Research Association under contract with NASA. Work in this paper is based on observations made with the *Spitzer Space Telescope*, which is operated by JPL, California Institute of Technology (Caltech), under a contract with NASA. Support for this work was provided by NASA through Cycle 9 and Cycle 13 awards issued by JPL/Caltech. This publication makes use of data products from *WISE*, which is a joint project of the University of California, Los Angeles, and JPL/Caltech, funded by NASA. This work has made use of data from the European Space Agency (ESA) mission *Gaia* (<https://www.cosmos.esa.int/gaia>), processed by the *Gaia* Data Processing and Analysis Consortium (DPAC, <https://www.cosmos.esa.int/web/gaia/dpac/consortium>). Funding for the DPAC has

been provided by national institutions, in particular the institutions participating in the *Gaia* Multilateral Agreement. This research has made use of IRSA, which is operated by JPL/Caltech, under contract with NASA, and KOA, which is operated by the W. M. Keck Observatory and the NASA Exoplanet Science Institute (NExScI), under contract with NASA. This research has also made use of the SIMBAD database, operated at CDS, Strasbourg, France.

Facilities: *Spitzer*(IRAC), USNO:61in(ASTROCAM), NTT (SOFI), UKIRT(WFCAM), *WISE*, *Gaia*, IRSA.

Software: IDL (<https://www.harrisgeospatial.com/Software-Technology/IDL>), MOPEX/APEX (<http://irsa.ipac.caltech.edu>), R (<https://www.r-project.org>), STILTS Taylor (2006), mpfit Markwardt (2009).

ORCID iDs

J. Davy Kirkpatrick  <https://orcid.org/0000-0003-4269-260X>
 Emily C. Martin  <https://orcid.org/0000-0002-0618-5128>
 Richard L. Smart  <https://orcid.org/0000-0002-4424-4766>
 Jacqueline K. Faherty  <https://orcid.org/0000-0001-6251-0573>
 Michael C. Cushing  <https://orcid.org/0000-0001-7780-3352>
 Adam C. Schneider  <https://orcid.org/0000-0002-6294-5937>
 Gregory N. Mace  <https://orcid.org/0000-0001-7875-6391>
 Christopher G. Tinney  <https://orcid.org/0000-0002-7595-0970>
 Edward L. Wright  <https://orcid.org/0000-0001-5058-1593>
 Patrick J. Lowrance  <https://orcid.org/0000-0001-8014-0270>
 James G. Ingalls  <https://orcid.org/0000-0003-4714-1364>
 Jeffrey A. Munn  <https://orcid.org/0000-0002-4603-4834>
 Scott E. Dahm  <https://orcid.org/0000-0002-2968-2418>

References

- Albert, L., Artigau, É., Delorme, P., et al. 2011, *AJ*, 141, 203
 Allen, P. R., Koerner, D. W., Reid, I. N., & Trilling, D. E. 2005, *ApJ*, 625, 385
 Allers, K. N., & Liu, M. C. 2013, *ApJ*, 772, 79
 Andersen, M., Meyer, M. R., Greissl, J., & Aversa, A. 2008, *ApJL*, 683, L183
 Artigau, É., Radigan, J., Folkes, S., et al. 2010, *ApJL*, 718, L38
 Baraffe, I., Chabrier, G., Barman, T. S., Allard, F., & Hauschildt, P. H. 2003, *A&A*, 402, 701
 Bardalez Gagliuffi, D. C., Burgasser, A. J., Gelino, C. R., et al. 2014, *ApJ*, 794, 143
 Bartlett, J. L., Lurie, J. C., Riedel, A., et al. 2017, *AJ*, 154, 151
 Bastian, N., Covey, K. R., & Meyer, M. R. 2010, *ARA&A*, 48, 339
 Bate, M. R. 2005, *MNRAS*, 363, 363
 Beamín, J. C., Minniti, D., Gromadzki, M., et al. 2013, *A&A*, 557, L8
 Bedin, L. R., & Fontanive, C. 2018, *MNRAS*, 481, 5339
 Beichman, C., Gelino, C. R., Kirkpatrick, J. D., et al. 2013, *ApJ*, 764, 101
 Beichman, C., Gelino, C. R., Kirkpatrick, J. D., et al. 2014, *ApJ*, 783, 68
 Best, W. M. J., Liu, M. C., Dupuy, T. J., & Magnier, E. A. 2017, *ApJL*, 843, L4
 Best, W. M. J., Liu, M. C., Magnier, E., & Dupuy, T. 2018, AAS Meeting, 231, 349.19
 Bihain, G., & Scholz, R.-D. 2016, *A&A*, 589, A26
 Bihain, G., Scholz, R.-D., Storm, J., & Schnurr, O. 2013, *A&A*, 557, A43
 Biller, B. A., Kasper, M., Close, L. M., Brandner, W., & Kellner, S. 2006, *ApJL*, 641, L141
 Bouvier, J., Stauffer, J. R., Martín, E. L., et al. 1998, *A&A*, 336, 490
 Bouy, H., Brandner, W., Martín, E. L., et al. 2003, *AJ*, 126, 1526
 Bouy, H., Duchêne, G., Köhler, R., et al. 2004, *A&A*, 423, 341
 Burgasser, A. J. 2004, *ApJS*, 155, 191
 Burgasser, A. J. 2007a, *ApJ*, 659, 655
 Burgasser, A. J., Burrows, A., & Kirkpatrick, J. D. 2006a, *ApJ*, 639, 1095
 Burgasser, A. J., Cruz, K. L., Cushing, M., et al. 2010a, *ApJ*, 710, 1142
 Burgasser, A. J., Cushing, M. C., Kirkpatrick, J. D., et al. 2011, *ApJ*, 735, 116

